Mechanical study on bending deformation and fracture of van der Waals layered materials

Masao AKIYOSHI

Contents

Chapter 1

Introduction

Two-dimensional (2D) materials such as graphene and transition metal dichalcogenides (TMDs) are layered crystals with a thickness of one or several atomic layers. These materials have a high elastic modulus and tensile strength in the in-plane direction owing to strong covalent and ionic bonds, but a very small bending rigidity in the out-of-plane direction [1–7]. In van der Waals (vdW)-layered materials (Fig. 1-1(a)), such as highly oriented pyrolytic graphite (HOPG) [8–11], many layers of 2D materials with a few defects and well-aligned crystallographic orientations are stacked by weak van der Waals (vdW) interactions. These materials exhibit unique mechanical properties owing to their structural and mechanical anisotropies. For example, owing to the weak interlayer interactions, an out-of-plane tension can easily cause delamination (Fig. 1-1(b)), and an interlayer slip can easily occur under shear loading [12–16] (Fig. 1-1(c)). In the in-plane compression of vdW-layered materials, deformation is caused by characteristic microscopic mechanisms accompanied by an interlayer slip and delamination such as rippling and kink buckling [17] (Figs. 1-1(d) and 1(e)).

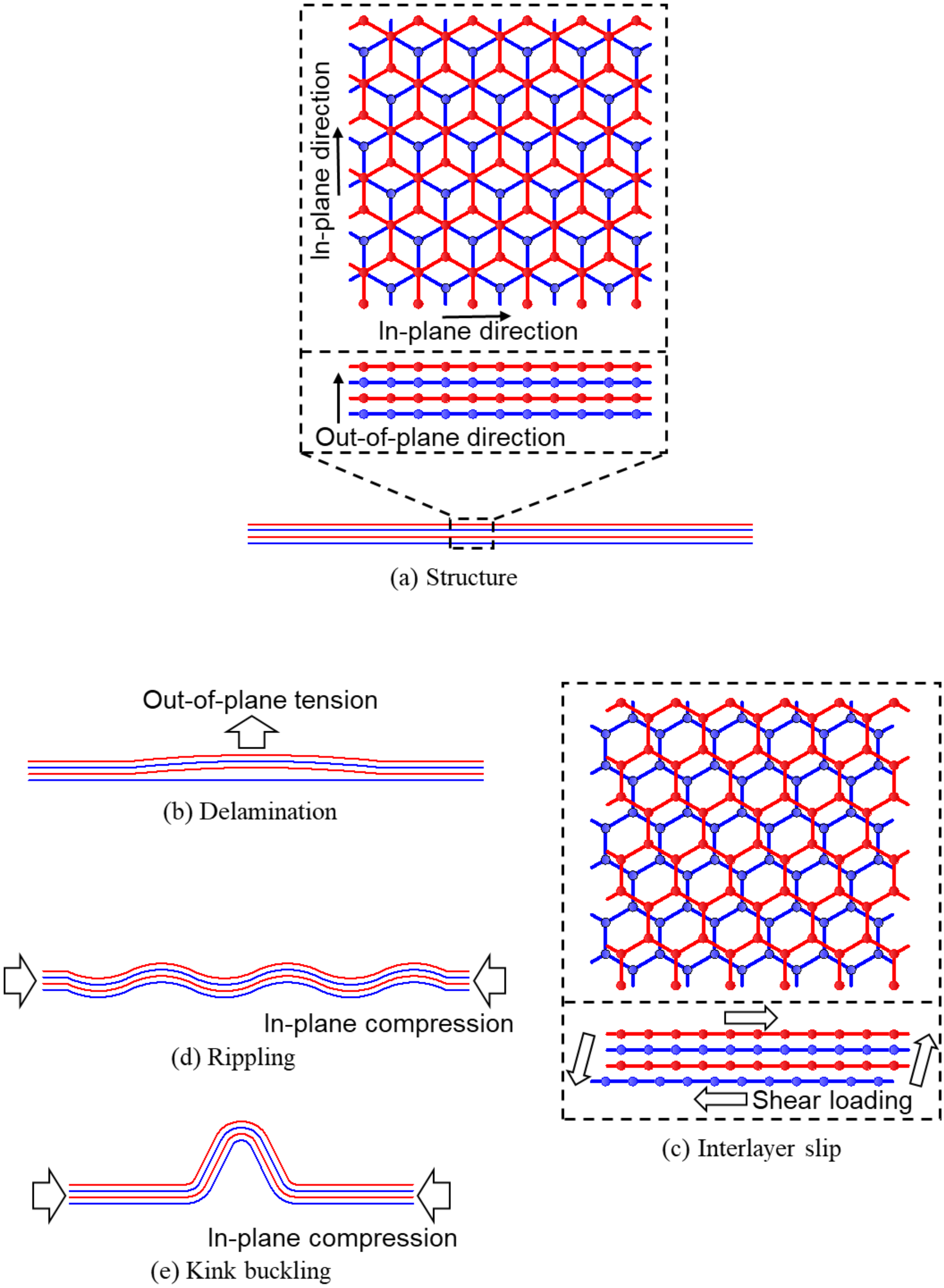

Fig. 1-1: Structure and characteristic deformation modes of vdW-layered materials

Bending deformation under out-of-plane loading is particularly important for flexible device applications that rely on the flexibility of vdW-layered materials (Fig. 1-2(a)(b)). The out-of-plane bending of vdW-layered materials is caused by a complex mechanism involving an interlayer slip and/or delamination in addition to macroscopic bending (tension and compression in the in-plane direction of each layer) [20–22]. Tang et al. [21] observed that, when multilayer MoS_2 consisting of up to 23 layers was subjected to a large bending deformation using a sharp needle, the deformation was accompanied by interlayer slip and delamination. Moreover, most of the deformation could be reversed by loading in the opposite direction. It has also been reported that, when a microsized graphite mesa is subjected to shear loading to induce the localized interlayer slip, it spontaneously recovers its deformation [13, 14]. The contact between the graphene layers changes from the commensurate state (energetically most stable) to the incommensurate state owing to shear loading, leading to a superlubricated state wherein the resistance to interlayer slip is drastically reduced. Thus, the slippage of the incommensurate layers can be reversed by a small driving force, such as the energy of the new surface formed by the interlayer sliding process. On the other hand, Barsoum et al. [23] showed that reversible nonlinear deformation with hysteresis occurs during the indentation of bulk vdW-layered materials. This is ascribable to the reversibility of the kink bands (rows of dislocation dipoles) formed by in-plane compression. These studies confirm that vdW-layered materials can accommodate large bending deformations with interlayer slippage and delamination without fracturing because of the extremely small bending stiffness of the individual layers and the weak interactions between these layers. In addition, the deformation can be restored readily by a small driving force. However, the large bending deformation characteristics of vdW-layered materials with interlayer slippage and the phenomenon of their self-restoration during unloading remain to be studied in detail.

Several studies have confirmed that the bending deformation of vdW-layered materials does not follow the classical continuum plate theory [6, 24, 25]. Wang et al. [6] investigated through deformation experiments (using the bulge method) and molecular dynamics (MD) analysis the bending stiffness and its dependence on the number of layers in multilayer graphene, MoS_2, and hexagonal boron nitride (hBN). Multilayer graphene, with the highest Young's modulus in the in-plane direction, exhibited the lowest bending stiffness which can be attributed to the discrete deformation of each layer caused by interlayer slips under bending deformation. Assuming that the vdW interaction between the layers does not occur, the bending stiffness is simply proportional to the number of layers (linear law) since each layer behaves as an independent discrete element as schematically shown in Fig.1-2(b). However, assuming that the vdW forces between layers are strong and the interlayer slip does not occur, the vdW-layered material behaves as a continuum body as schematically shown in Fig.1-2(a), and the bending stiffness is proportional to the cube of the number of layers, according to the bending theory of a continuum plate (cubic law). In actual vdW-layered materials, the vdW forces are weak between the layers, and hence each layer deforms in a semi-discrete manner, the interlayer slips easily occur, and the bending stiffness falls between the linear and cubic laws [6, 24, 26, 27]. Therefore, to elucidate the mechanics of bending deformation in vdW-layered materials, it is essential to construct a mechanical model that takes semi-discreteness into account.

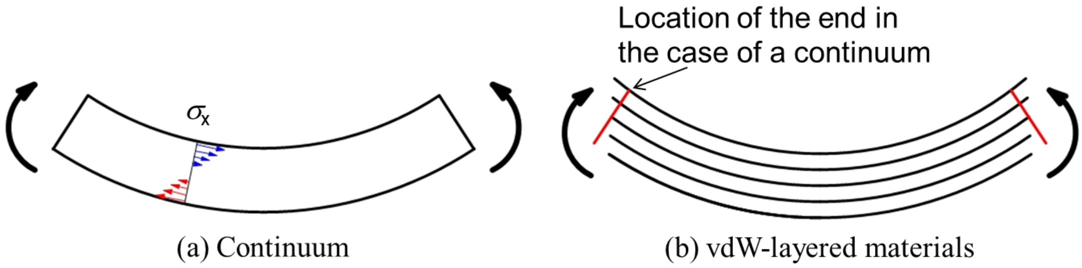

Fig. 1-2: Schematic diagram comparing bending deformation of continuum and vdW-layered materials

In the bending deformation of submicron to micron scale vdW-layered materials [22, 28], localized interlayer slips were observed, and the number of slips increased as the deformation progressed as shown in Fig. 1-3. The localized and discrete interlayer slips play an important role in the characteristic bending deformation. In addition, interlayer slips are considered to preferentially occur between incommensurate interlayers. For example, transmission electron microscopy (TEM) images of HOPG [29] revealed the presence of interlayer grain boundaries in the range of 5–30 nm along the stacking direction. Therefore, modeling considering discrete interlayer slips is effective to construct a universal mechanical model that describes the nonlinear bending deformation characteristics and self-restores upon unloading in vdW-layered materials. Up to our knowledge, such a mechanical model has not yet been reported.

Numerical simulations and theoretical studies have been conducted to elucidate the bending behavior of vdW-layered materials. MD simulation [4, 25, 26, 30] is an effective method for analyzing bending deformation of vdW-layered materials. In principle, bending deformation of vdW-layered materials can be reproduced by MD using an appropriate potential function. However, performing MD analysis on submicron- to micron-sized structures with hundreds to thousands of layers is extremely impractical in terms of computational cost. For this reason, theoretical models [2, 4, 25, 26, 30–33] based on the Euler-Bernoulli beam theory have been proposed. The simplest model is the Timoshenko beam model (TBM) [34], which takes into account the deflection of beam caused by both bending moment and shear force. Furthermore, a modified Timoshenko beam model [31] considering the bending stiffness of each layer and models [25, 32, 33] taking into account the failure of the planar-section hypothesis due to interlayer slip have been proposed. Huang et al. [33] proposed a centerline-based stacked model, which takes into account expansion and contraction, bending of each layer, and interlayer shear stiffness. On the other hand, these theoretical models can only provide solutions for simple shapes and boundary conditions, such as the bending of a beam. Finite element method (FEM) of continuum bodies is used to analyze deformation characteristics for arbitrary shapes and boundary conditions. However, the above theoretical models and the FEM analysis cannot reproduce the occurrence and propagation of localized interlayer slip which plays an important role as shown in Fig.1-3.

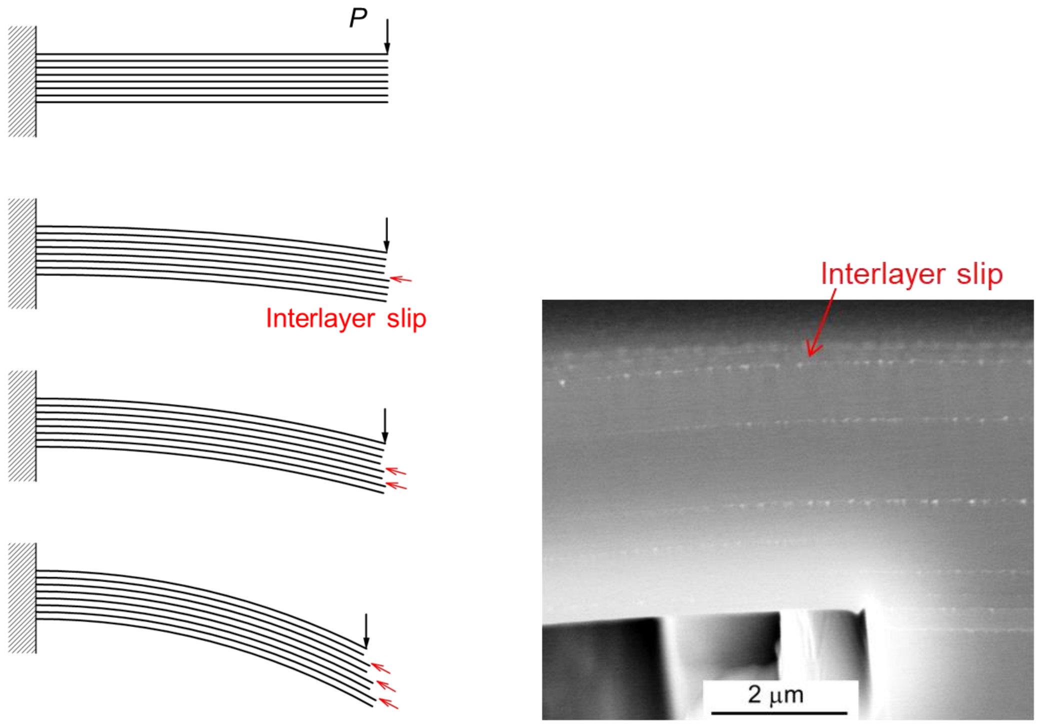

(a) Bending of vdW-layered materials consisting of multiple layers

(b)SEM image of the side of a $MoTe_2$ cantilever beam [28]

Fig. 1-3: Schematic diagram showing the occurrence of discrete interlayer slip inferred from experimental results

On the other hand, considering the reliability of vdW-layered materials in applications, research on their strength against fracture is important. Studies on fracture, such as nanoindentation tests on single-layer graphene [35] and MoS_2 [36], have experimentally shown fracture strengths comparable to their theoretical ideal strengths. In such a local loading test using an indenter tip, the high-stress region is confined to the nanoscale; therefore, it is not easily affected by potential structural defects and exhibits high strength. However, in tensile tests and fracture toughness tests on single- or several-layer freestanding 2D materials, the 2D materials exhibit defect-sensitive brittle fracture [36-38], and the fracture toughness is low [38–41]. However, the fracture characteristics of vdW-layered materials have not yet been fully elucidated.

Fracture is a phenomenon caused by a local mechanical field owing to a defect inside a material: for example, stress concentration at a notch root or a singular stress field formed at a crack tip [42]. At a notch root or crack tip, the stress is concentrated because of the detour of the stress flow, resulting in locally high stress. When considering the material strength of vdW-layered materials, the strength against in-plane loads that can withstand high stress due to atomic bonds is important. Considering the structural anisotropy of vdW-layered materials, typical cracks are classified as in-plane cracks (Fig. 1-4(a)) or out-of-plane cracks (Fig. 1-4(b)) in the in-plane load. In in-plane cracks, stress is transmitted by a strong bond in the plane of the 2D material; therefore, they can be regarded as continuum bodies in the in-plane direction, and a singular stress field is formed at a crack tip. On the other hand, in out-of-plane cracks, the interaction between layers is weak, and the force is difficult to transmit between layers. As an extreme assumption, if there is no interaction between layers (complete discrete body), each layer behaves as an isolated element, and no force is transmitted in the out-of-plane direction; thus, stress concentration does not occur. Because vdW-layered materials comprise weakly interacting 2D material elements, it is expected that a singular stress field for out-of-plane cracks is unlikely to occur (and the stress concentration in the notch root is reduced). In other words, it is thought to exhibit an intermediate mechanical property between a continuum body that transmits stresses three-dimensionally and a discrete body. For vdW-layered materials, it is important to consider the semi-discrete characteristics from the viewpoint of fracture.

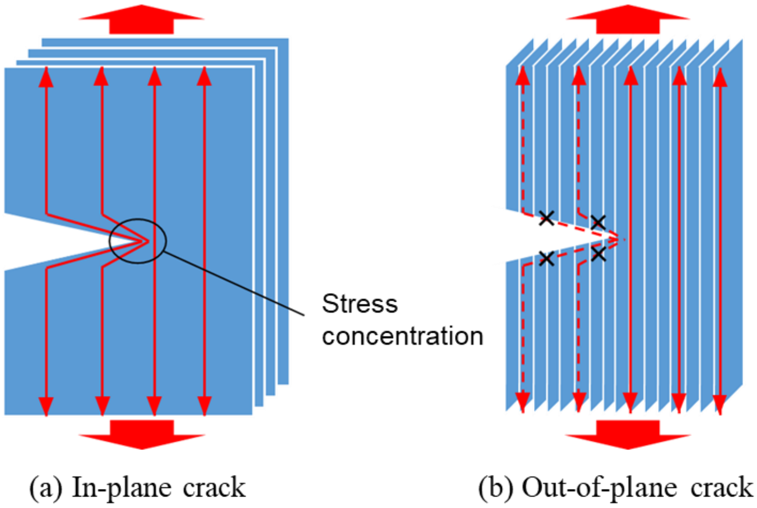

Fig. 1-4: In-plane and out-of-plane cracks in vdW-layered materials

As a study on the disappearance of the singular stress field of a discrete body, Sumigawa et al. [43] conducted a mechanical test and analysis on a thin film consisting of spiral Ta_2O_5 nanostructured elements on the order of 10 nm in diameter grown and arranged on a substrate. The singular stress field disappeared in the nanoelement-assembled thin film. However, in such structures, because the elements are sparsely distributed at intervals, the strength is lower than that of the homogeneous material [44]. However, there is a possibility that vdW-layered materials show high strength, reflecting the maximum in-plane strength, because the atomic layers are densely laminated by weak interactions in the materials. In other words, vdW-layered materials can be strong and tough owing to their atomic layer thickness, closely stacked structure, and discreteness. However, research from this perspective has not been sufficiently conducted.

The purpose of this study is to elucidate the mechanics of deformation and fracture of vdW-layered materials. In particular, focusing on the deformation under out-of-plane loading, the bending deformation characteristics and self-restoration properties are experimentally clarified. Then, considering the microscopic mechanism of bending deformation of vdW-layered materials (i.e., discrete interlayer slip), a mechanical model that universally reproduces the characteristic nonlinear and self-restoration deformation characteristic is constructed. Furthermore, the fracture mechanisms in vdW-layered materials are determined and the high fracture toughness owing to the disappearance of the singular stress field is experimentally demonstrated.

VdW-layered materials are expected to be used in a wide range of applications due to their excellent electrical, mechanical, and chemical properties [45–47]. Among these, large bending deformation capability and high fracture toughness are required for the development of stretchable electronics and strain semiconductors using vdW-layered materials [48, 49]. In particular, from the viewpoint of device miniaturization and performance enhancement, the deformation and fracture properties of submicron-order vdW-layered materials are important. However, because the deformation and fracture characteristics of vdW-layered materials vary depending on the material, dimensions, and loading mode, it is necessary to understand the strength and reliability of each product, which is one of the bottlenecks in improving development efficiency. Another objective of this research is to provide rational design guidelines for product development by elucidating the universal mechanics governing the deformation and fracture of vdW-layered materials.

This dissertation consists of five chapters including this chapter (Chapter 1). Chapter 2 aims to elucidate the bending deformation characteristics and self-restoration properties of vdW-layered materials under out-of-plane loading. For this reason, bending deformation experiments are conducted on submicron-sized HOPG cantilevers. HOPG is a typical vdW-layered material. Chapter 3 aims to develop a mechanical model for bending deformation of vdW-layered materials that universally reproduces the characteristic nonlinear reversible deformation by considering discrete interlayer slips. To this purpose, vdW-layered materials are modeled as a laminate of interacting discrete deformable layers (semi-discrete layer model), and the interlayer interaction is modeled using a cohesive zone model (CZM) that reproduces local interlayer slip. Bending deformation analysis of cantilevered beams of HOPG and $MoTe_2$, which are typical vdW-layered materials, is performed, and the validity of the model is discussed by contrasting the experimental results. Chapter 4 aims to elucidate the fracture mechanism of vdW-layered materials and demonstrate the high fracture toughness due to the disappearance of the singular stress field caused by the discrete nature of the structure. Fracture toughness tests are performed on $MoTe_2$ for in-plane and out-of-plane cracks. The fracture mechanism and mechanics are investigated based on the semi-discrete layer model developed in Chapter 3. Chapter 5 summarizes the results obtained in the chapters and provides an outlook.

References

[1] G. Cao and H. Gao, Mechanical properties characterization of two-dimensional materials via nanoindentation experiments, *Prog. Mater. Sci.* **103**, 558 (2019).

[2] X. Chen, C. Yi, and C. Ke, Bending stiffness and interlayer shear modulus of few-layer graphene, *Appl. Phys. Lett.* **106**, 101907 (2015).

[3] X. Ma, L. Liu, Z. Zhang, and Y. Wei, A Method to determine the geometry-dependent bending stiffness of multilayer graphene sheets, *J. Appl. Mech.* **88**, 011004 (2021).

[4] Y. Shen and H. Wu, Interlayer shear effect on multilayer graphene subjected to bending, *Appl. Phys. Lett.* **100**, 101909 (2012).

[5] Y. Sun, J. Pan, Z. Zhang, K. Zhang, J. Liang, W. Wang, Z. Yuan, Y. Hao, B. Wang, J. Wang, Y. Wu, J. Zheng, L. Jiao, S. Zhou, K. Liu, C. Cheng, W. Duan, Y. Xu, Q. Yan, and K. Liu, Elastic Properties and fracture behaviors of biaxially deformed, polymorphic $MoTe_2$, *Nano Lett.* **19**, 761 (2019).

[6] G. R. Wang, Z. H. Dai, J. K. Xiao, S. Z. Feng, C. X. Weng, L. Q. Liu, Z. P. Xu, R. Huang, and Z. Zhang, Bending of multilayer van der Waals materials, *Phys. Rev. Lett.* **123**, 116101 (2019).

[7] Y. Sun, Y. Wang, E. Wang, B. Wang, H. Zhao, Y. Zeng, Q. Zhang, Y. Wu, L. Gu, X. Li, and K. Liu, Determining the interlayer shearing in twisted bilayer MoS_2 by nanoindentation, *Nat. Commun.* **13**, 3898 (2022).

[8] B. Dai, L. Fu, Z. Zou, M. Wang, H. Xu, S. Wang, and Z. Liu, Rational design of a binary metal alloy for chemical vapour deposition growth of uniform single-layer graphene, *Nat. Commun.* **2**, 522 (2011).

[9] J. Hass, W. A. de Heer, and E. H. Conrad, The growth and morphology of epitaxial multilayer graphene, *J. Phys. Condens. Mat.* **20**, 323202 (2008).

[10] H. J. Shin, K.K. Kim, A. Benayad, S. M. Yoon, H.K. Park, I. S. Jung, M. H. Jin, H. K. Jeong, J. M. Kim, J. Y. Choi, and Y. H. Lee, Efficient reduction of graphite oxide by sodium borohydride and its effect on electrical conductance, *Adv. Funct. Mater.* **19**, 1987 (2009).

[11] C. Y. Su, A. Y. Lu, Y. P. Xu, F. R. Chen, A. N. Khlobystov, and L. J. Li, High-quality thin graphene films from fast electrochemical exfoliation, *Acs Nano* **5**, 2332 (2011).

[12] O. L. Blakslee, D. G. Proctor, E. J. Seldin, G. B. Spence, and T. Weng, Elastic constants of compression-annealed pyrolytic graphite, *J. Appl. Phys.* **41**, 3373 (1970).

[13] Z. Liu, J. R. Yang, F. Grey, J. Z. Liu, Y. L. Liu, Y. B. Wang, Y. L. Yang, Y. Cheng, and Q. S. Zheng, Observation of microscale superlubricity in graphite, *Phys. Rev. Lett.* **108**, 20 (2012).

[14] Z. Liu, S. M. Zhang, J. R. Yang, J. Z. Liu, Y. L. Yang, and Q. S. Zheng, Interlayer shear strength of single crystalline graphite, *Acta Mech. Sinica-Prc* **28**, 978 (2012).

[15] R. Nicklow, N. Wakabaya, and H. G. Smith, Lattice-dynamics of pyrolytic-graphite, *Phys. Rev. B* **5**, 4951 (1972).

[16] J. P. Oviedo, K. C. Santosh, N. Lu, J. G. Wang, K. Cho, R. M. Wallace, and M. J. Kim, Situ TEM characterization of shear-stress-induced interlayer sliding in the cross section view of molybdenum disulfide, *Acs Nano* **9**, 1543 (2015).

[17] M. W. Barsoum, X. Zhao, S. Shanazarov, A. Romanchuk, S. Koumlis, S. J. Pagano, L. Lamberson, and G. J. Tucker, Ripplocations: A universal deformation mechanism in layered solids, *Phys. Rev. Mater.* **3**, 013602 (2019).

[18] A. Farajpour, A. A. Solghar, and A. Shahidi, Postbuckling analysis of multi-layered graphene sheets under non-uniform biaxial compression, *Physica E* **47**, 197 (2013).

[19] A. Kushima, X. F. Qian, P. Zhao, S.L. Zhang, and J. Li, Ripplocations in van der

Waals Layers, *Nano Lett*. **15**, 1302 (2015).

[20] I. Nikiforov, D. M. Tang, X. Wei, T. Dumitrica, and D. Golberg, Nanoscale bending of multilayered boron nitride and graphene ribbons: Experiment and objective molecular dynamics calculations, *Phys*. *Rev*. *Lett*. **109**, 025504 (2012).

[21] D. M. Tang, D. G. Kvashnin, S. Najmaei, Y. Bando, K. Kimoto, P. Koskinen, P. M. Ajayan, B. I. Yakobson, P. B. Sorokin, J. Lou, and D. Golberg, Nanomechanical cleavage of molybdenum disulphide atomic layers, *Nat*. *Commun*. **5**, 3631 (2014).

[22] P. Wang, K. F. Wang, B. L. Wang, L. Xi1, K. Sano, T. Shimada, H. Hirakata, and D. N. Fang, Interlaminar fracture toughness measurement of multilayered 2D thermoelectric materials Bi_2Te_3 by a tapered cantilever bending (TCB) experiment, *Exp*. *Mech*. **62**, 165 (2022).

[23] M. W. Barsoum, A. Murugaiah, S. R. Kalidindi, T. Zhen, and Y. Gogotsi, Kink bands, nonlinear elasticity and nanoindentations in graphite, *Carbon* **42**, 1435 (2004).

[24] E. M. Han, J. Yu, E. Annevelink, J. Son, D. A. Kang, K. Watanabe, T. Taniguchi, E. Ertekin, P. H. Y. Huang, and A. M. van der Zande, Ultrasoft slip-mediated bending in few-layer graphene, *Nat*. *Mater*. **19**, 305 (2020).

[25] F. Pan, G. R. Wang, L. Q. Liu, Y. L. Chen, Z. Zhang, and X. H. Shi, Bending induced interlayer shearing, rippling and kink buckling of multilayered graphene sheets, *J*. *Mech*. *Phys*. *Solids* **122**, 340 (2019).

[26] Y. L. Liu, Z. P. Xu, and Q. S. Zheng, The interlayer shear effect on graphene multilayer resonators, *J. Mech*. *Phys*. *Solids* **59**, 1613 (2011).

[27] S. Y. Peng and Y. J. Wei, On the influence of interfacial properties to the bending rigidity of layered structures, *J. Mech*. *Phys*. *Solids* **92**, 278 (2016).

[28] M. Akiyoshi, T. Shimada, and H. Hirakata, Analyzing the bending deformation of

van der Waals-layered materials by a semi-discrete layer model, *J. Appl. Phys.* **134**, 175102 (2023).

[29] S. Y. Park, H. C. Floresca, Y. J. Suh, and M. J. Kim, Electron microscopy analyses of natural and highly oriented pyrolytic graphites and the mechanically exfoliated graphenes produced from them, *Carbon* **48**, 797 (2010).

[30] R. Nazemnezhad, Nonlocal Timoshenko beam model for considering shear effect of van der Waals interactions on free vibration of multilayer graphene nanoribbons, *Compos. Struct.* **133**, 522 (2015).

[31] H. Qin, Y. Yan, H. Liu, J. Liu, Y. W. Zhang, and Y. Liu, Modified Timoshenko beam model for bending behaviors of layered materials and structures, *Extreme Mech. Lett.* **39**, 100799 (2020).

[32] X. Ma, L. Liu, Z. Zhang, and Y. Wei, Bending stiffness of circular multilayer van der Waals material sheets, *J. Appl. Mech.* **89**, 031011 (2022).

[33] Z. Huang, Z. He, Y. Zhu, and H. Wu, A general theory for the bending of multilayer van der Waals materials, *J. Mech. and Phys. Solids* **171**, 105144 (2023).

[34] S. P. Timoshenko, *Philosophical Magazine* **41**, 744 (1921).

[35] C. Lee, X. D. Wei, J.W. Kysar, and J. Hone, Measurement of the elastic properties and intrinsic strength of monolayer graphene, *Science* **321**, 385 (2008)

[36] S. Bertolazzi, J. Brivio, and A. Kis, Stretching and Breaking of Ultrathin MoS_2, *Acs Nano*. **5**, 9703 (2011).

[37] Y. C. Yang, X. Li, M. R. Wen, E. Hacopian, W. B. Chen, and Y. J. Gong, Brittle fracture of 2D $MoSe_2$, *Adv. Mater.* **29** (2017).

[38] P. Zhang, L. Ma, F. Fan, Z. Zeng, C. Peng, P. E. Loya, Z. Liu, Y. Gong, J. Zhang, X. Zhang, P. M. Ajayan, T. Zhu, and J. Lou, Fracture toughness of graphene, *Nat.*

Commun. **5**, 3782 (2014).

[39] X. Wei, S. Xiao, F. Li, D. M. Tang, Q. Chen, Y. Bando, and D. Golberg, Comparative fracture toughness of multilayer graphenes and boronitrenes, *Nano Lett*. **15**, 689 (2015).

[40] B. Jang, B. Kim, J. H. Kim, H. J. Lee, T. Sumigawa, and T. Kitamura, Asynchronous cracking with dissimilar paths in multilayer graphene, *Nanoscale* **9**, 44 (2017).

[41] C. Ca, S. Mukherjee, J. Y. Howe, D. D. Perovic, Y. Sun, C. V. Singh, and T. Filleter, Nonlinear fracture toughness measurement and crack propagation resistance of functionalized graphene multilayers, *Science Adv*. **4**, 7202 (2018).

[42] T. L. Anderson, Fracture mechanics: Fundamentals and applications, Fourth edition, *CRC Press* (2017).

[43] T. Sumigawa, H. Hirakata, M. Takemura, S. Matsumoto, M. Suzuki, and T. Kitamura, Disappearance of stress singularity at interface edge due to nanostructured thin film, *Eng*. *Fract*. *Mech*. **75**, 3073 (2008).

[44] H. Hirakata, T. Nishihira, A. Yonezu, and K. Minoshima, Interface strength of structured nanocolumns grown by glancing angle deposition, *Eng*. *Fract*. *Mech*. **78**, 2800 (2011).

[45] A. K. Geim and I. V. Grigorieva, Van der Waals heterostructures, *Nat*. **499**, 419 (2013).

[46] K. S. Novoselov, A. Mishchenko, A. Carvalho, and A. H. Castro Neto, 2D materials and van der Waals heterostructures, *Science* **353**, aac9439 (2016).

[47] P. H. Tan, W. P. Han, W. J. Zhao, Z.H. Wu, K. Chang, H. Wang, Y. F. Wang, N. Bonini, N. Bonini, N. Marzari, N. Pugno, G. Savini, A. Lombardo, and A.C. Ferrari, The shear mode of multilayer graphene, *Nat*. *Mat*. **11**, 294 (2012).

[48] F. De Juan, A. Cortijo, M. A. Vozmediano, and A. Cano, Aharonov–Bohm interferences from local deformations in graphene, *Nat*. *Phys*. **7**, 810 (2011).

[49] F. Guinea, M. I. Katsnelson, and A. K. Geim, Energy gaps and a zero-field quantum Hall effect in graphene by strain engineering, *Nat*. *Phys*. **6**, 30 (2010).

Chapter 2

Bending deformation and self-restoration of submicron-sized graphite cantilevers

2.1 Introduction

In vdW-layered materials such as HOPG, a large number of 2D layers are stacked based on weak vdW forces [1–6]. Owing to the loosely packed structure of these extremely thin atomic-layer materials, vdW-layered materials will exhibit different mechanical properties than their three-dimensionally bonded counterparts. However, the mechanical properties of these materials need to be clarified.

Bending deformation during out-of-plane loading is particularly important with respect to devices based on the flexibility of vdW-layered materials. The bending deformation of a continuum body involves both tension and compression, wherein the stress varies from tensile to compressive in the neutral plane. On the other hand, the out-of-plane bending of vdW-layered materials is caused by a more complex mechanism involving macroscopic bending (the in-plane tension and compression of the individual layers) as well as microscopic interlayer slip and delamination.

The bending deformation of vdW-layered materials has been studied both experimentally and theoretically [7–9]. These studies confirm that vdW-layered materials can accommodate large bending deformations with interlayer slip and delamination without fracturing because of the extremely small bending stiffness of the individual layers and the weak interactions between these layers. In addition, the deformation can be restored by loading in the opposite direction [10]. It has also been shown that the interlayer slip can be restored readily by a small driving force, such as the surface energy [11, 12]. On the other hand, Barsoum et al. [13] showed that reversible nonlinear deformation with hysteresis occurs during the indentation of bulk vdW-layered materials. This is ascribable to the reversibility of the kink bands (rows of dislocation dipoles) formed by in-plane compression. However, the large bending deformation characteristics of vdW-layered materials with interlayer slips and the phenomenon of their self-restoration during unloading remain to be studied in detail.

The purpose of this chapter is to elucidate the bending deformation characteristics and self-restoration properties of submicron-sized graphite, a typical vdW-layered material, under out-of-plane loading. Submicron-scale cantilever beam specimens were fabricated from bulk HOPG using focused ion beam (FIB) etching and performed *in situ* TEM-based bending tests. The results suggest that the graphite cantilevers exhibit large out-of-plane deformation and self-restore almost completely under unloading. The mechanism of self-restoration is discussed based on the experimental results.

2.2 Materials and methods

2.2.1 Materials and specimens

The test material was HOPG (ZYA-DS, Tips Nano Co.) with a mosaic spread of 0.4 ± 0.1° and grain size of 2–10 mm. A block with a side of ~10 mm was cut from the bulk material by FIB etching (FB2200, Hitachi High-Tech Co.) and fixed on a sample stage using a micromanipulator and FIB-induced tungsten vapor deposition. Cantilever specimens were then fabricated by FIB etching. FIB etching was conducted using Ga ions under the following conditions: accelerating voltage, 40 kV; irradiation current, 3.91–76.56 nA (rough processing) and 0.01–0.84 nA (final processing). The detailed cantilever fabrication procedure is described in Supplementary Material S2.1.

Fig. 2-1 shows a schematic diagram of the loading method and a TEM image (JEM2100, JEOL Ltd.) of a cantilever specimen. The specimen was subjected to out-of-plane loading with an indenter in the direction of stacking of the graphene layers (y-direction). Specimens 1–11 were prepared with different widths (w = 0.85–2.20 mm), heights (h = 0.33–0.53 mm), and lengths (L = 2.29–4.32 mm), as listed in Table 2-1. The distance between the fixed end and load point (L_p) was approximately 1.5 mm for each specimen.

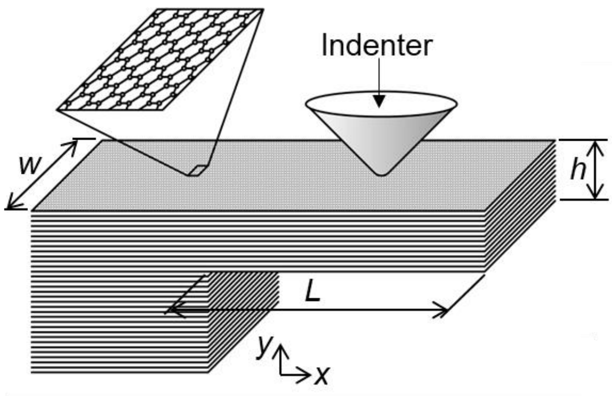

(a) Specimen and loading

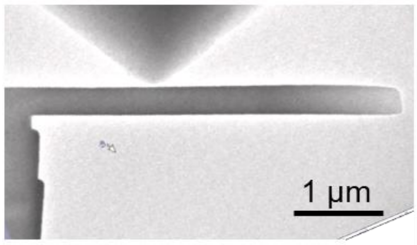

(b) TEM image

Fig. 2-1: Specimen shape and experimental method; a cantilever specimen of submicron-scale graphite is fabricated by FIB. The specimen is subjected to out-of-plane loading with a diamond indenter in the direction of stacking of the graphene layers.

Table 2-1: Dimensions of fabricated cantilever specimens

Specimen No.	*w*, µm	*h*, µm	*L*, µm
1	1.08	0.33	3.42
2	1.10	0.40	4.32
3	1.05	0.32	2.29
4	1.11	0.32	4.19
5	0.98	0.53	3.08
6	1.20	0.40	3.00
7	2.20	0.46	2.90
8	2.20	0.40	2.50
9	0.85	0.37	3.24
10	1.36	0.52	3.19
11	0.91	0.36	2.99

2.2.2 Experimental method

In situ TEM observations (JEM2100, JEOL Ltd.) were conducted in conjunction with a micromechanical testing system (Hysitron PI- 95TEM PicoIndenter, Bruker Co.) that allowed for the control and measurement of the load and displacement of an indenter. The specifications of the testing apparatus are listed in Table S2-1 in Supplementary Material S2.2. The system consisted of a transducer for controlling and measuring the load and displacement of the indenter and a three-dimensional piezostage for positioning the sample (Fig. 2-1).

The tip of the indenter was moved to the top of the cantilever, as shown in Fig. 2-1(a). The displacement of the indenter in the y-direction, d, was increased at a rate of 5 nm/s until the maximum displacement specified for each test, d_{max}, was reached. d_{max} was defined as the maximum value of d such that the origin was at the position where the indenter was in contact with the surface of the cantilever. The indenter was kept stationary for 5 s once d_{max} had been reached, and then unloaded at a rate of 5 nm/s to the initial position. Two types of conductive diamond indenters with different tip shapes were used. A cube-corner indenter with a tip radius of curvature of ~250 nm was used for the tests performed on Specimens 1, 2, 3, 5, 6, and 10, while a rectangular, brick-like indenter was used for the tests performed on Specimens 4, 7, 8, 9, and 11, in order to allow for larger displacements and prevent torsion. In the case of the cube-corner indenter, when the cantilever was bent to a significant degree, the side of the indenter came in contact with the top surface of the cantilever. This prevented the further deformation of the cantilever. On the other hand, by placing one side of the bottom of the rectangular indenter parallel to the width direction of the cantilever, the cantilever could be deformed to a greater degree. Multiple tests were conducted on each specimen with different d_{max} values. The number of tests performed on the specimens as well as the d_{max} values during the first and last tests are listed in Table 2-2. The d_{max} values for all the tests are listed in Table S2-2 in Supplementary Material S2.2. All tests were performed under a vacuum of 1.5×10^{-5} Pa during *in situ* TEM imaging at an accelerating voltage of 200 kV (Specimens 1–10) or 80 kV (Specimen 11). The beam source of the TEM was a LaB_6 filament. The temperature of the specimen was not controlled, and the laboratory temperature was set to ~293 K. During some of the tests performed on Specimen 4, the ability of the specimen to undergo irradiation-induced deformation recovery was examined by irradiating it with an electron beam for a long period (5.25 h) after the test. In this experiment, the material was irradiated by an electron beam at a current density of 1.3×10^3 A/m^2, which is two orders of magnitude higher than that used in the other deformation experiments (~10 A/m^2). To evaluate the effects of FIB processing and electron-beam irradiation on the structure of the microcantilever specimens, pristine HOPG and FIB-processed specimens with and without electron-beam irradiation were evaluated by Raman spectroscopy (LabRAM HR-800, Horiba Ltd.) at a wavelength of 488 nm, power of 3 mW, and exposure time of 10 s. The Raman spectra were measured three times and averaged.

Table 2-2: Number of loading tests performed on each specimen and d_{max} values during first and last tests

Specimen No.	1	2	3	4	5	6	7	8	9	10	11
Number of loading tests	17	13	15	9	8	9	3	25	9	3	21
d_{max} during first test, nm	17	166	64	239	150	187	97	76	47	122	69
d_{max} during last test, nm	687	825	630	1349	716	381	18	648	434	205	994

2.3 Results and discussions

2.3.1 Irradiation damage

a. FIB-induced damage

Since the cantilever specimens were prepared by FIB etching, the surface of the processed specimens had a damaged layer due to FIB irradiation [14–16]. To minimize the effect of this damaged layer, the upper and lower surfaces were finished with a small irradiation current of 0.01 nA. However, the existence of the damaged layer was unavoidable. To estimate the thickness of the FIB-damaged layer, a specimen that was processed under the same conditions as those for the bending test specimens was fractured by applying an impact load, and the fracture surface was observed by scanning electron microscopy (SEM). As shown in Fig. S2-2 in Supplementary Material 2.4, the thickness of the FIB-damaged layer was approximately 25 nm. This damage layer on the upper and lower surfaces occupied 10–15 % of the specimen height (h = 0.32–0.53 μm). This may have a non-negligible effect on the mechanical properties. Fig. 2-2 shows the Raman spectra of pristine HOPG and FIB-processed specimens with and without electron-beam irradiation. The absorption coefficient a of graphite is approximately 0.4×10^6 cm^{-1} [17] at the wavelength of 488 nm, and the laser penetration depth h_{laser} is approximately 30 nm based on the formula $h_{laser} = 2.3 / 2a$ [18, 19]. Therefore, the obtained Raman spectra mainly reflect the structure of the FIB-damaged layer. Pristine HOPG had a strong G peak at around 1580 cm^{-1}, indicating a typical graphite structure with few defects. On the other hand, the FIB-processed specimen had a broad spectrum with a D peak at around 1360 cm^{-1} in addition to the G peak. This indicates that FIB processing caused defects and amorphization in the surface layer. Although the detailed structure of the damaged layer with a thickness of ~25 nm due to FIB processing is unknown, it is thought to be amorphous carbon (a-C) with reduced crystallinity [20].

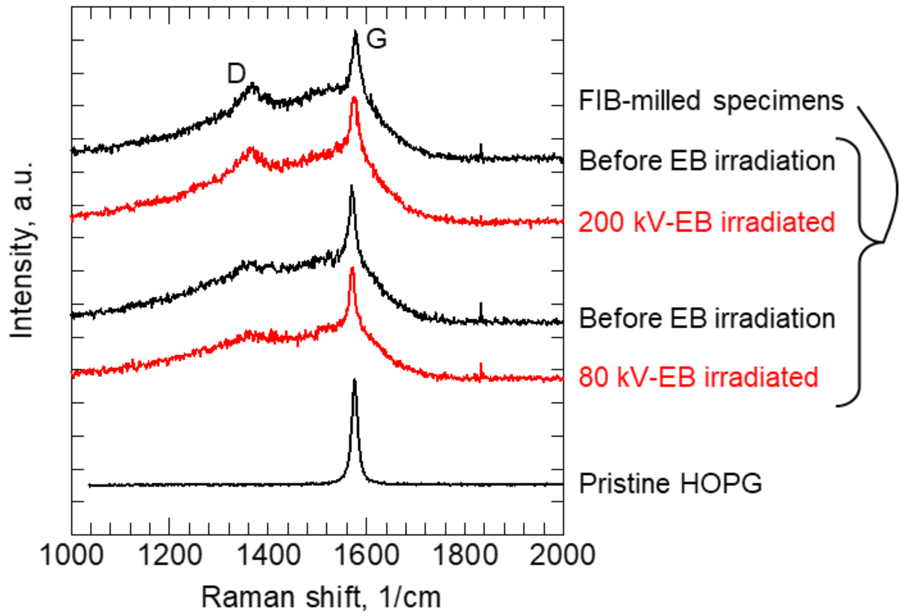

Fig. 2-2: Raman spectra of pristine HOPG and FIB processed specimen before and after electron beam irradiation

b. Electron beam-induced damage

The electron-beam irradiation of nanoscale carbon structures causes severe structural changes such as recombination of bonds [21–25]. However, the cantilever specimen used in this study had a width of ~1 μm or larger; therefore, any electron beam-induced damage would occur mainly near the surface. A FIB-processed specimen (Specimen 11) was irradiated with an electron beam with a lower accelerating voltage of 80 kV and current density of 19 A/m^2 for 1 h. Another FIB-processed specimen was irradiated with an electron beam at 200 kV and 13 A/m^2 for 3.5 h, which are similar to the irradiation conditions used in the bending tests. Fig. 2-2 shows the Raman spectra of these specimens, and Table S2-4 in Supplementary Material S2.5 summarizes the ratio of the intensity of the D and G peaks (I_D/I_G). At both 80 kV and 200 kV, no significant changes due to electron-beam irradiation were observed. Therefore, it was concluded that electron-beam irradiation did not significantly change the structure of the specimens during the bending tests.

2.3.2 Bending deformation characteristics

Fig. 2-3(a) shows the relationship between the load P and displacement d during the first bending test (d_{max} = 17 nm) of Specimen 1. During the loading process, P increased linearly with increasing d up to approximately 5 μN and decreased linearly during the unloading process. During this test, linear elastic deformation was observed, and the deformation was fully recovered upon unloading. Fig. 2-3(b) shows the P–d curve during the ninth test at d_{max} = 166 nm. During the loading process, P increased linearly, and the slope of the curve began to decrease at approximately d = 50 nm, with the curve becoming a nonlinear one with a convex shape. During the unloading process, P returned to zero almost linearly as d was decreased. Fig. 2-4 shows *in situ* TEM images of Specimen 1 obtained during the 9th test. The red dashed lines in all the figures indicate the shape of the cantilever beam before the test. It can be observed that the deformation of the cantilever was restored almost completely during unloading. The loading tests indicated that the P–d relationship was nonlinear. In addition, a hysteresis loop was observed during unloading, but the deformation was completely restored. Fig. 2-3(c) shows the P–d relationship as determined during the 11th test at d_{max} = 300 nm. The loading curve was nonlinear and exhibited a similar upwardly convex shape. The unloading curve was also nonlinear and showed a gently downwardly convex shape. Moreover, d did not return to zero during the unloading process, with a small deformation, d = 30 nm, remaining. The TEM images obtained during this test are shown in Fig. 2-5. The deformation of the cantilever was largely restored. However, the cantilever did not return to its initial position (red dashed line). When the deformation was increased to d_{max} = 300 nm, the P–d curve exhibited hysteresis, and most of the deformation was recovered. However, plastic deformation (permanent deformation) was observed.

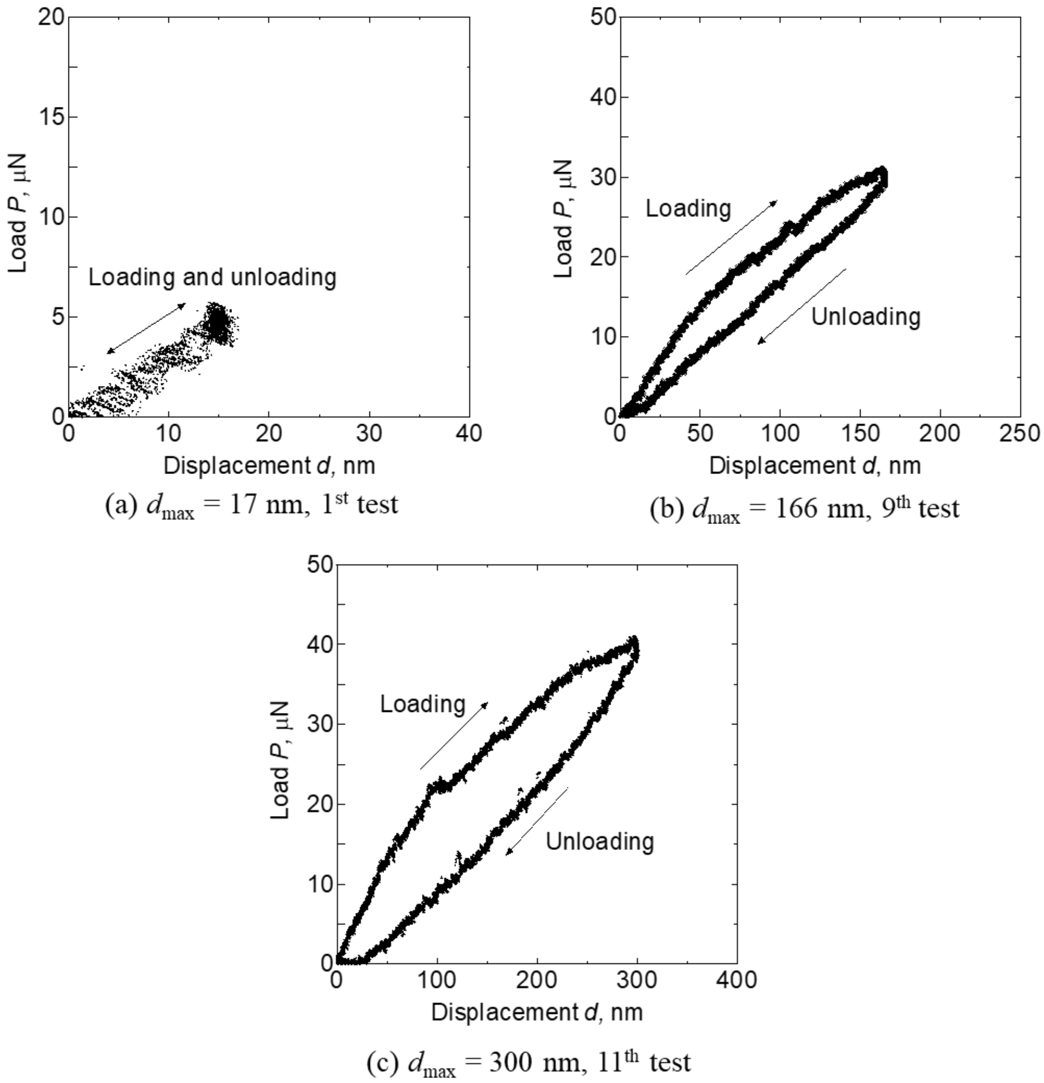

Fig. 2-3: Load–displacement (P–d) relationships for Specimen 1

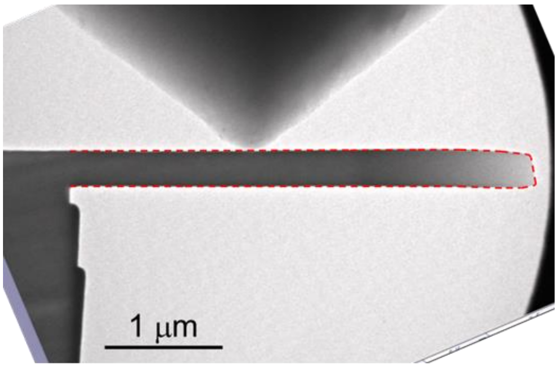

(a) Before test

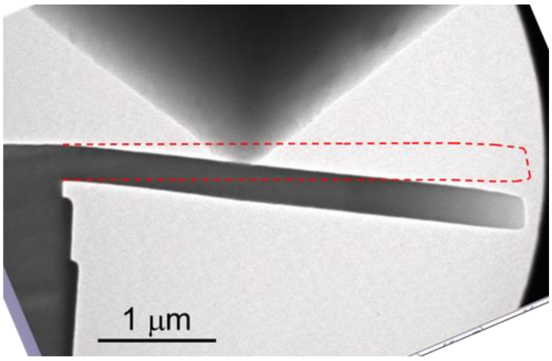

(b) At maximum displacement

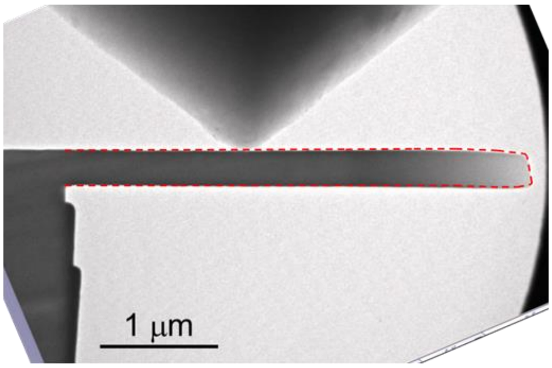

(c) After test

Fig. 2-4: TEM images of Specimen 1 during 9th test

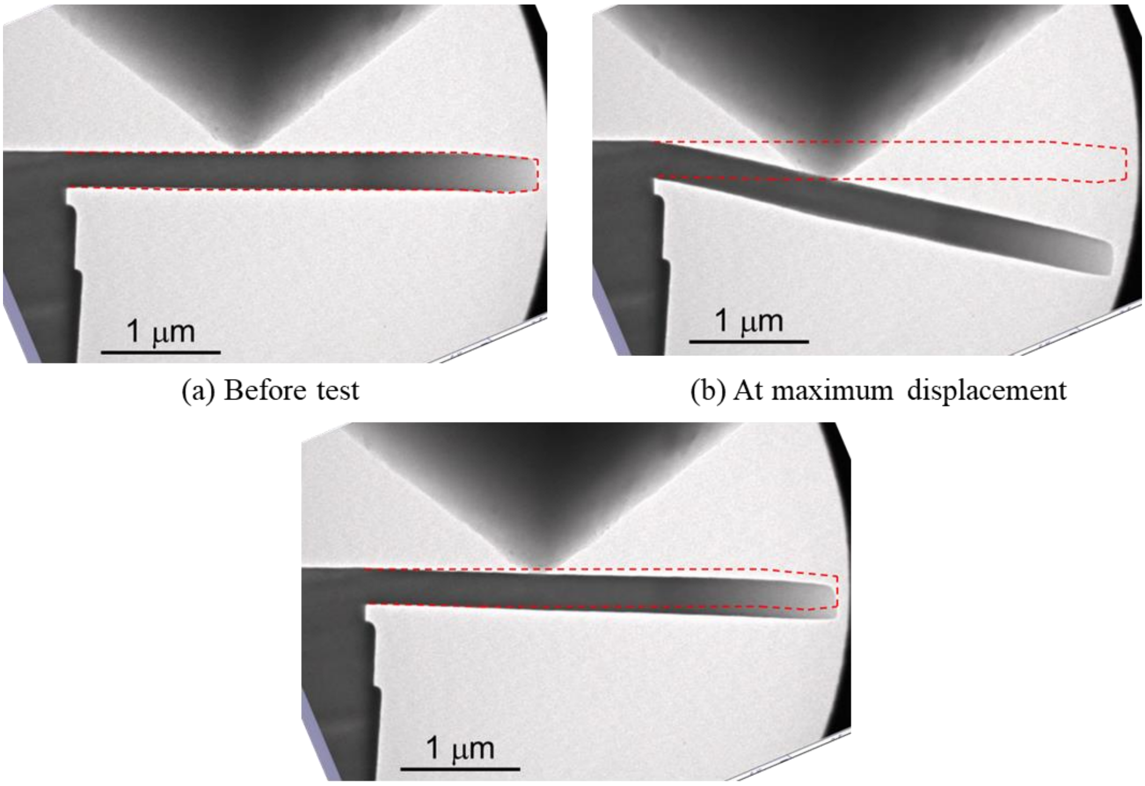

(a) Before test (b) At maximum displacement

(c) After test

Fig. 2-5: TEM images of Specimen 1 during 11th test

The other specimens showed qualitatively similar P–d relationships, depending on $d_{\max}$. In other words, the P–d curves could be divided into the following three stages, based on the degree of deformation.

Stage 1: Completely linear elastic behavior. As the displacement d is increased, the load P increases linearly, and the deformation is completely recovered upon unloading.

Stage 2: Reversible nonlinear behavior with a hysteresis loop. As d is increased, P increases linearly. However, the P–d curve eventually becomes nonlinear and exhibits an upwardly convex shape. A hysteresis loop is observed during unloading, and the deformation is completely recovered.

Stage 3: Nonlinear behavior with plastic deformation. As d is increased, P increases linearly. However, the P–d relationship eventually becomes nonlinear and exhibits an upwardly convex shape. The deformation is largely restored during unloading, but the plastic deformation remains.

2.3.3 Universality of deformation

Figs. 2-6(a) and (b) show the P–d relationships for Specimens 6 (w = 1.20 mm) and 8 (w = 2.20 mm), which had the same height, h = 0.40 mm. The results for the d_{max} values corresponding to Stage 2, namely, d_{max} = 187 nm in Fig. 2-6(a) and d_{max} = 168 nm in Fig. 2-6(b), are shown. The two specimens showed qualitatively similar behaviors, exhibiting upwardly convex nonlinear curves during the loading process and slightly downwardly convex nonlinear curves during the unloading process. Moreover, in both cases, the deformation was fully recovered. For the same d value, P was higher for Specimen 8, which was wider than Specimen 6. Fig. 2-6(c) shows the relationship between P/w (i.e., the load per unit width) and d. The curves are similar over the entire loading–unloading process. These results indicate that similar out-of-plane deformation occurred in both cases regardless of the specimen width. It is noted that a FIB-damaged layer of thickness ~25 nm existed on each surface of the cantilever beam. Although the proportion of the damaged layer to the overall width increased as w decreased, no significant difference was found in the bending properties ((P/w)–d relationships), as shown in Fig. 2-6(c). Thus, the effect of surface damage on the mechanical properties could be almost ignored.

Fig. 2-7(a) presents the (P/w)–d relationships for Specimens 1 (h = 0.33 mm), 6 (h = 0.40 mm), and 5 (h = 0.53 mm), which had different heights but exhibited qualitatively similar behaviors. Specimens with a larger h tend to show greater stiffness. First, we focus on the initial stiffness corresponding to the (P/w)–d curves and its dependence on h. As per the continuum beam theory, the bending stiffness is proportional to h^3. On the other hand, when 2D materials are bent in a discrete manner without interacting with each other, the stiffness is linearly proportional to h. It has been shown that, for vdW-layered materials, the relationship between the bending stiffness and height falls between the linear and cubic laws [7, 9–26]. However, h of the cantilever specimens is approximately 1/5–1/3 of the length L_p, and comparable bending and shearing act; thus, the beam approximation is not valid. In addition, graphite has strong elastic anisotropy [27], and the elastic constant C_{11} for in-plane deformation, which is dominant in bending deformation, is two orders of magnitude larger than the elastic constant C_{44} for shear (as shown in Table 2-3). Therefore, the graphite cantilevers are difficult to bend and easy to shear, and the isotropic continuum beam theory cannot be applied. Here, we analyzed the elastic properties of the cantilever specimen by employing the finite element method (FEM) considering the anisotropic elastic constants of graphite. A detailed analysis is provided in Supplementary Material 2.6. The results indicate that the bending rigidity S is roughly proportional to the 1.3 power of h/L_p when h = 300–500 nm and L_p = 1300–1800 nm. S is defined as the slope of the initial linear region of the (P/w)–d curve, and the least-squares approximation using the power law $S = k(h/L_p)^{\alpha}$ can be used to determine the value of the exponent (α = ~1.3). Thus, in the continuum theory, the height dependence of the bending stiffness of the cantilevers is not the cubic law, but rather a value close to a linear law (α = ~1.3).

Table 2-3: Elastic constants of graphite used in FEM analysis [34]

C_{11}	C_{12}	C_{13}	C_{33}	C_{44}	C_{66}
1109 GPa	139 GPa	0 GPa	38.7 GPa	4.95 GPa	485 GPa

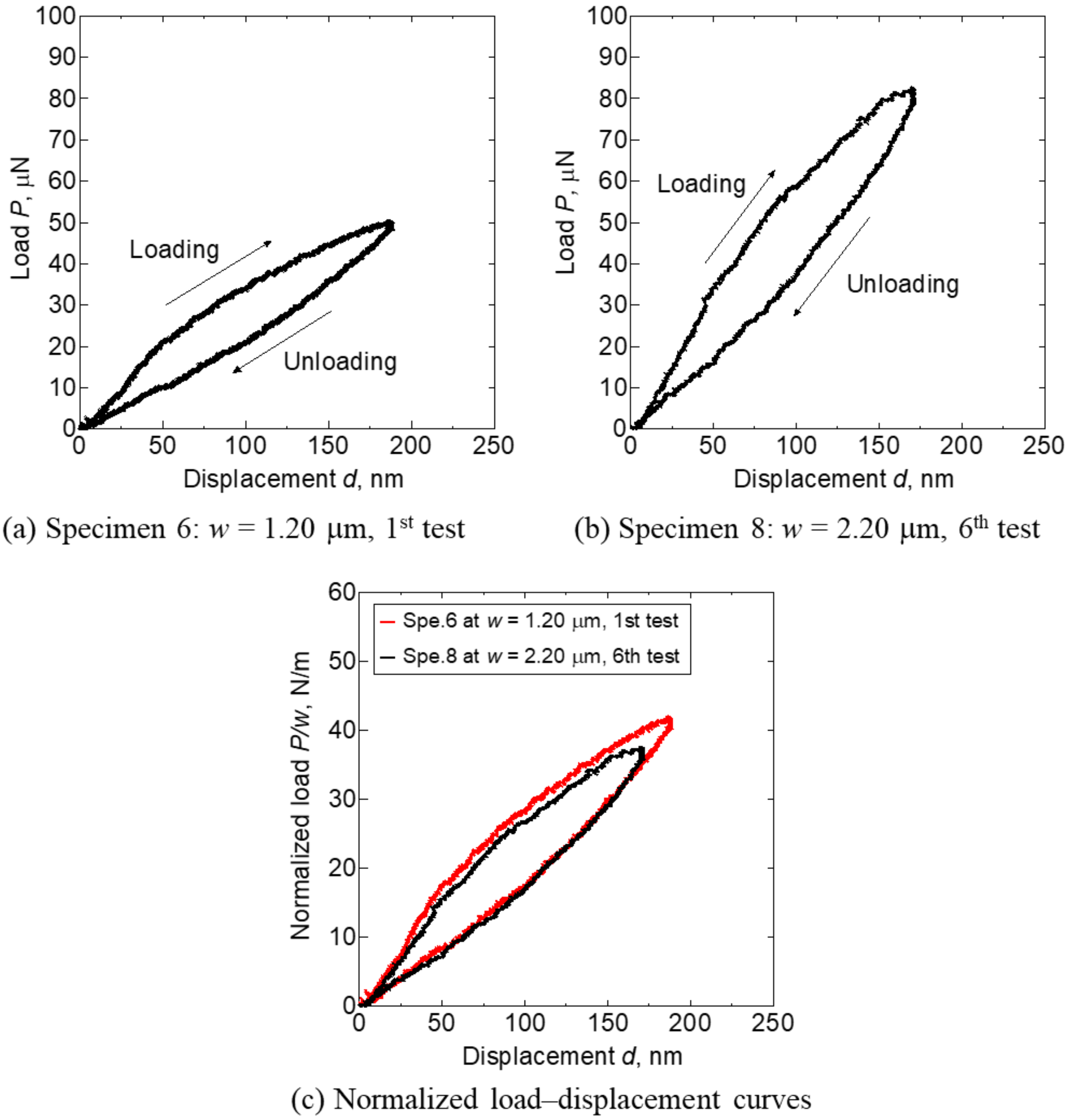

(a) Specimen 6: w = 1.20 μm, 1st test
(b) Specimen 8: w = 2.20 μm, 6th test
(c) Normalized load–displacement curves

Fig. 2-6: Load–displacement (P–d) relationships for specimens with different widths

The FIB-damaged layer on the specimen surface, which was indicated to be a-C from the Raman spectra shown in Fig. 2-2 and SEM image in Fig. S2-2, may affect the deformation behavior of the cantilever beams. To explore this, the effect of the a-C layer on the bending deformation properties were analyzed by FEM (Supplementary Material S2.6.4). This analysis revealed that the existence of the a-C layer with a thickness of 25 nm had no significant effect on the deformation properties.

Fig. 2-7(b) shows the relationship between S obtained in the experiments and the normalized height h/L_p. The (P/w)–d relationship shown in Fig. 2-7(a) is almost linear until d = ~50 nm regardless of h. Therefore, the slope in this region was taken to be S. Although there is scatter between specimens, S increases as h/L_p increases. This tendency is in agreement with the analysis results based on the continuum theory (solid gray line in Fig. 2-7(b)). By approximating the relationship between the mean values of S in each specimen and h/L_p using the power law, the exponent α = ~1.2 can be obtained (the coefficient of determination, R^2, is 0.64). This value is consistent with that estimated from the continuum theory, α = ~1.3. Therefore, the initial stiffness of this specimen can be predicted to some extent by continuum elastic analysis considering anisotropy. However, the rigidity obtained from the experiments is generally less than that in the FEM analysis results. One of the possible reasons for this difference is that the initial stiffness evaluated in the experiment is not the exact initial stiffness, and deformation accompanied with interlayer slips had already occurred by this stage (until d = ~50 nm). Moreover, the FEM analysis performed for comparison assumed plane strain, and the rigidity tended to be ~10% higher than that in the three-dimensional (3D) analysis (Supplementary Material S2.6). In previous studies [7, 8, 9, 28, 26, 29–31], the bending rigidity was evaluated when multilayer graphene was greatly deformed, and the dependence on the height (number of layers) did not follow the continuum theory. However, by focusing on the initial stiffness of the submicron-sized cantilever specimen, including in this study, it becomes evident that the bending rigidity can be predicted to some extent within the framework of continuum mechanics.

Fig. S2-8(a) shows the results of bending tests performed under electron-beam irradiation at accelerating voltages of 200 kV (Specimen 1) and 80 kV (Specimen 11). The effect of electron-beam irradiation was thought to be small in the latter specimen. A typical (P/w)–d relationship showing nonlinearity, hysteresis, and recovery was obtained at both 80 and 200 kV. Furthermore, as shown in Fig. 2-7(b), the initial stiffness S was in the same region at both 80 and 200 kV. From these results, it could be concluded that the electron-beam irradiation during the *in situ* TEM experiments did not cause any significant structural changes in the specimen, and that the obtained mechanical properties reflect those of HOPG.

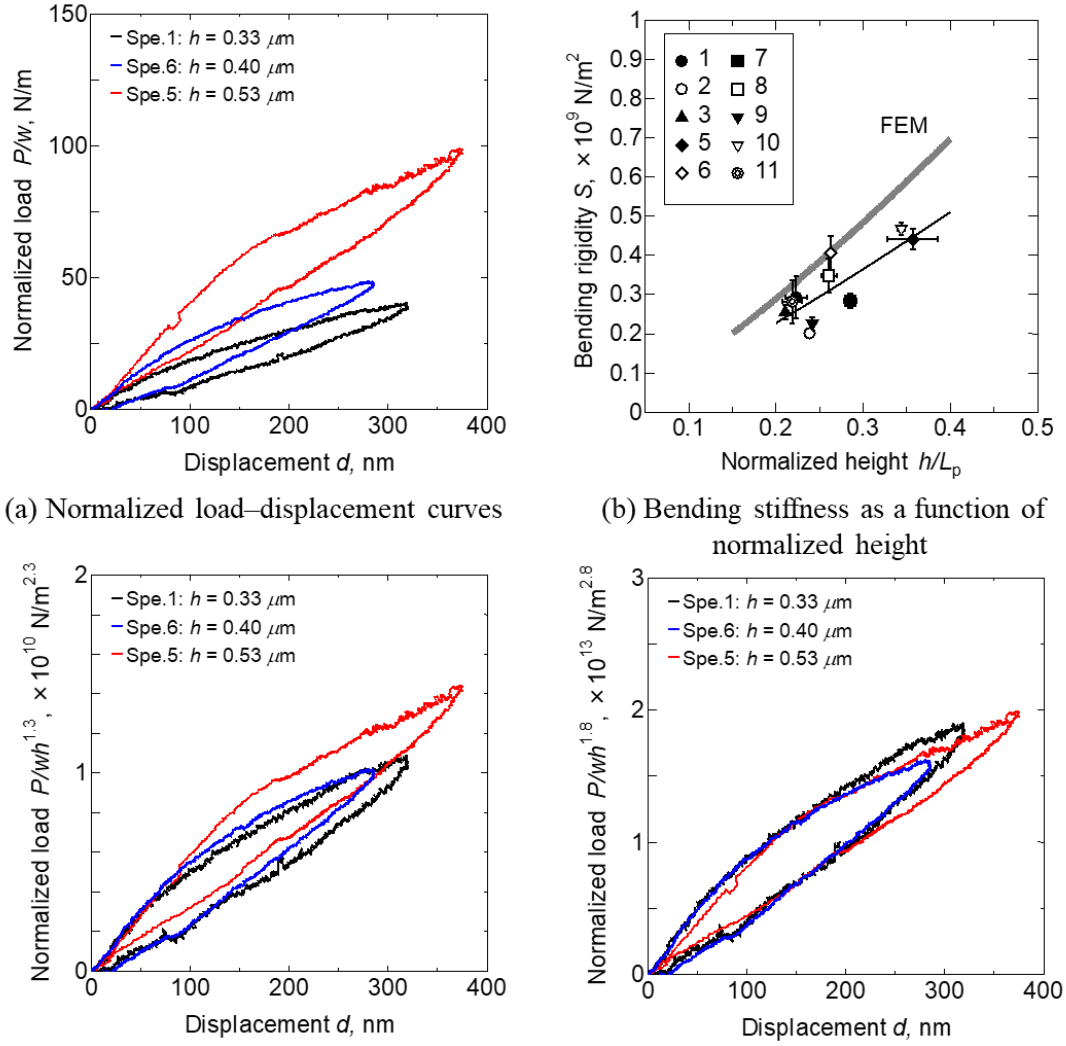

(a) Normalized load–displacement curves

(b) Bending stiffness as a function of normalized height

(c) Normalized by $h^{1.3}$

(d) Normalized by $h^{1.8}$

Fig. 2-7: Comparison of load–displacement ((P/w)–d) relationships for specimens with different heights

Next, we focused on the stiffness in the nonlinear region. Fig. 2-7(c) shows the relationships between the normalized load, P/wh^{α}, which is P/w normalized based on h^{α}, and d for Specimens 1, 5, and 6, where $\alpha = 1.3$ is used. Owing to this normalization, the initial slope is almost the same for all specimens up to d = ~50 nm. Roughly similar behavior was observed during entire loading–unloading process regardless of h. However, the smaller the h, the smaller the slope of the nonlinear region. In cantilever specimens, the smaller the h, the greater the contribution of bending to shear. It has been shown that in pure bending of multilayer graphene, the bending rigidity decreases because the layers become incommensurate as the bending progresses [8, 9, 29, 30]. Therefore, it is considered that the rigidity decreases because the curvature becomes larger as h decreases. By adjusting α, we searched for a value at which all nonlinear loading–unloading behaviors would be similar. Fig. 2-7(d) shows the (P/wh^{α})–d curves normalized using $\alpha = 1.8$. Almost identical behavior is observed throughout the loading–unloading process regardless of h. This finding indicates that the nonlinear bending deformation behavior is universally dominated by the power law $h^{1.8}$ when h = 0.33–0.53 mm. These results suggest that the height dependence of the nonlinear region of bending deformation is different from that of the initial rigidity.

2.3.4 Self-restoration property

To quantitatively investigate the self-restoration of the nonlinear deformation of the cantilever specimens, their deflection angles were calculated from the *in situ* TEM images. Although the curvature is commonly used as the measure of bending, the deflection angle at the loading point was adopted as the measure of deformation because the curvature was not uniform along the beam during the deformation process. Figs. 2-8(a)–(c) show the measurement procedure. The deflection angle at the loading point, θ (shown in Fig. 2-8(b)), was defined as the difference with respect to the initial state before the first test (shown in Fig. 2-8(a)). The θ value at the maximum displacement, d_{max}, was defined as θ_{max}, and the θ value after unloading was defined as θ_{res} (shown in Fig. 2-8(c)). The deformation restoration factor, *r*, defined as a measure of the degree of self-restoration of the bending deformation, was calculated as follows:

$$r = \frac{\theta_{\mathrm{max}} - \theta_{\mathrm{res}}}{\theta_{\mathrm{max}}} \qquad (1)$$

A larger *r* indicates a greater degree of recovery owing to unloading, with $r = 1$ indicating complete restoration.

Fig. 2-8(d) shows the *r* value as a function of θ_{max} for all the tests for Specimens 1–9 and 11. All the plots lie within a linear band, with *r* decreasing approximately linearly with an increase in θ_{max}. The relationship was approximated using the least-squares method as follows:

$$r = -0.0102\theta_{\mathrm{max}} + 0.9898 \qquad (2)$$

The coefficient of determination, R^2, was 0.7325. Thus, there is a strong correlation between *r* and θ_{max}. For example, at $\theta_{max} = 20°$, $r = 0.79$, indicating that despite the large nonlinear deformation, the deformation recovered to a significant degree after the unloading.

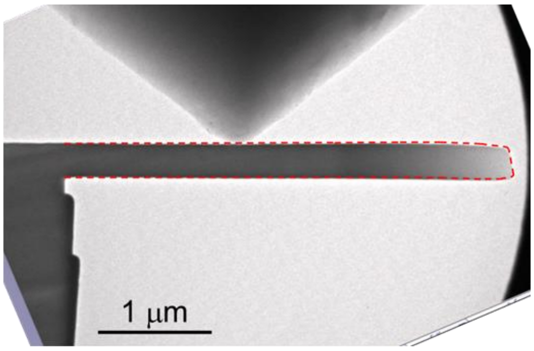

(a) Reference state before the 1st test of each specimen

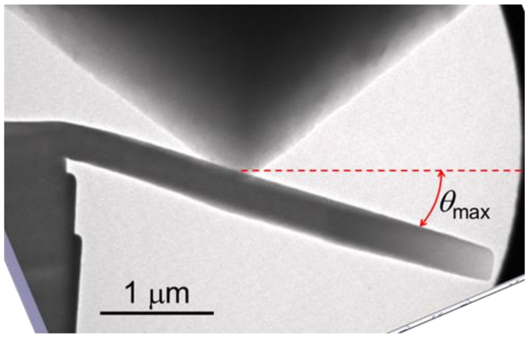

(b) Deflection angle at the maximum displacement d_{max}

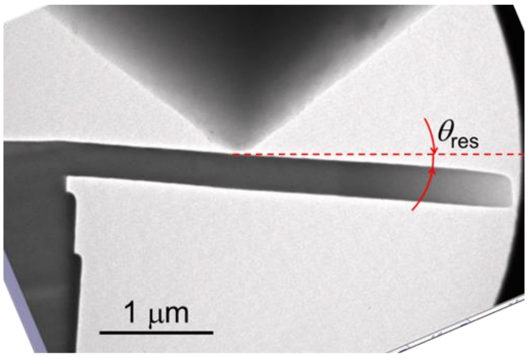

(c) Residual deflection angle after unloading

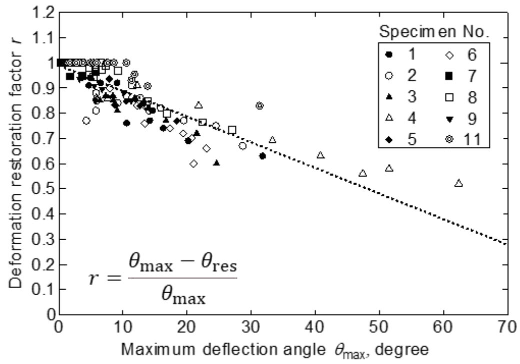

(d) Deformation restoration factor r as a function of maximum deflection angle θ_{max}

Fig. 2-8: Self-restoration of deformation. Deflection angle at the loading point is calculated from the *in situ* TEM images as a measure of deformation.

Next, the self-restoration of the mechanical properties was evaluated by comparing multiple *P–d* curves for the same specimen. Fig. 2-9(a) shows the *P–d* curves for the 1st and 2nd tests (Stage 1) and 8th and 9th tests (Stage 2) for Specimen 1. During Stage 1, both the loading and unloading curves were indicative of linear elastic behavior, and the mechanical properties of the sample did not degrade. On comparing the *P–d* curves for Stage 2, it was found that the loading and unloading curves were almost identical. In other words, even during Stage 2, where a large hysteresis loop was observed, the mechanical properties were restored by unloading, and the initial stiffness was similar to that during

Stage 1. This suggests that the mechanical properties did not degrade during the unloading cycles with nonlinear deformation.

Fig. 2-9 (b) shows the *P–d* curves for the 11^{th}–13^{th} tests (Stage 3) as well as that for the 9^{th} test (Stage 2) for Specimen 1. During the 11^{th} and 12^{th} tests, a slight permanent deformation remained after unloading; however, the *P–d* curves were similar. The initial stiffness was almost the same as that during the 9^{th} test and the previous tests, and the mechanical properties were restored. However, during the 13^{th} test, P decreased at d = ~22 nm. After the sudden decrease in P, the slope of the loading curve decreased sharply, in contrast to the case during the previous tests. In addition, a large plastic deformation of d = ~100 nm remained after unloading. In other words, the self-restoration property was lost during this loading cycle. In the other specimens, multiple deformations with d_{max} greater than ~300 nm caused a reduction in the stiffness and a large plastic deformation. Although the reason for this result is unknown, repeated large deformations beyond a certain threshold can cause the deterioration of the mechanical properties as well as the self-restoration ability of a material.

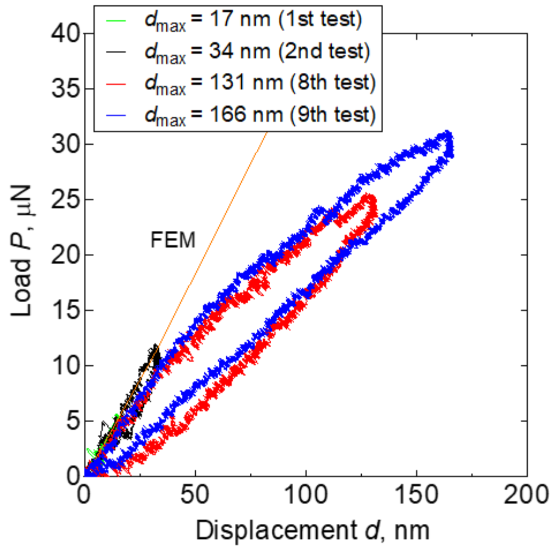

(a) Stages 1 and 2

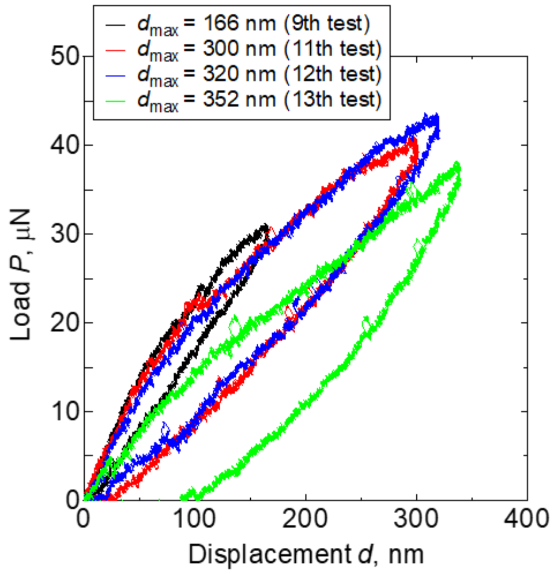

(b) Stages 2 and 3

Fig. 2-9: *P*–*d* relationships for Specimen 1 with different maximum displacements $d_{\max}$. (a) The results show that initial stiffness is restored even after the large nonlinear bending deformation. The stiffness calculated by FEM is larger than the experimental results. (b) In the 13th test, the stiffness clearly decreases, and large plastic deformation remains after unloading.

2.3.5 Mechanism of self-restoration

The results of the bending tests performed on the graphite cantilever specimens confirmed that the shape and mechanical properties of the specimens were restored upon unloading, even though the *P*–*d* curves showed significant nonlinearity. First, we discuss the cause of the nonlinearity in the *P*–*d* curves. The probable causes of this nonlinearity include material nonlinearity, geometric nonlinearity, and boundary nonlinearity owing to indenter contact. To evaluate these factors separately, deformation analysis was performed using 3D FEM, wherein the cantilever was assumed to be a linear elastic body, and the geometrical and boundary nonlinearities were considered. The details of the analysis are given in Supplementary Material 2.6. For Specimen 1, the vdW-layered material was assumed to be an orthotropic elastic material, and the elastic constants [27] shown in Table 2-3 were used. The diamond indenter was modeled using a hemisphere with a radius of 250 nm, Young's modulus of 1140 GPa, and Poisson's ratio of 0.07. Fig. 2-9(a) shows the *P–d* relationship as determined by the FEM analysis (see solid line) along with the experimental results. The slopes of the *P–d* curves corresponding to the tests were smaller than that of the curve from the FEM analysis, except in the initial region, which corresponded to linear elastic deformation. The *P–d* curve determined from the FEM analysis was almost linear until $d_{\max}$ was reached. This indicates that the large nonlinearity observed in the experimental *P–d* curves was not owing to geometrical or boundary nonlinearity. Therefore, the nonlinearity observed during the bending tests of the graphite cantilevers can be ascribed to material nonlinearity.

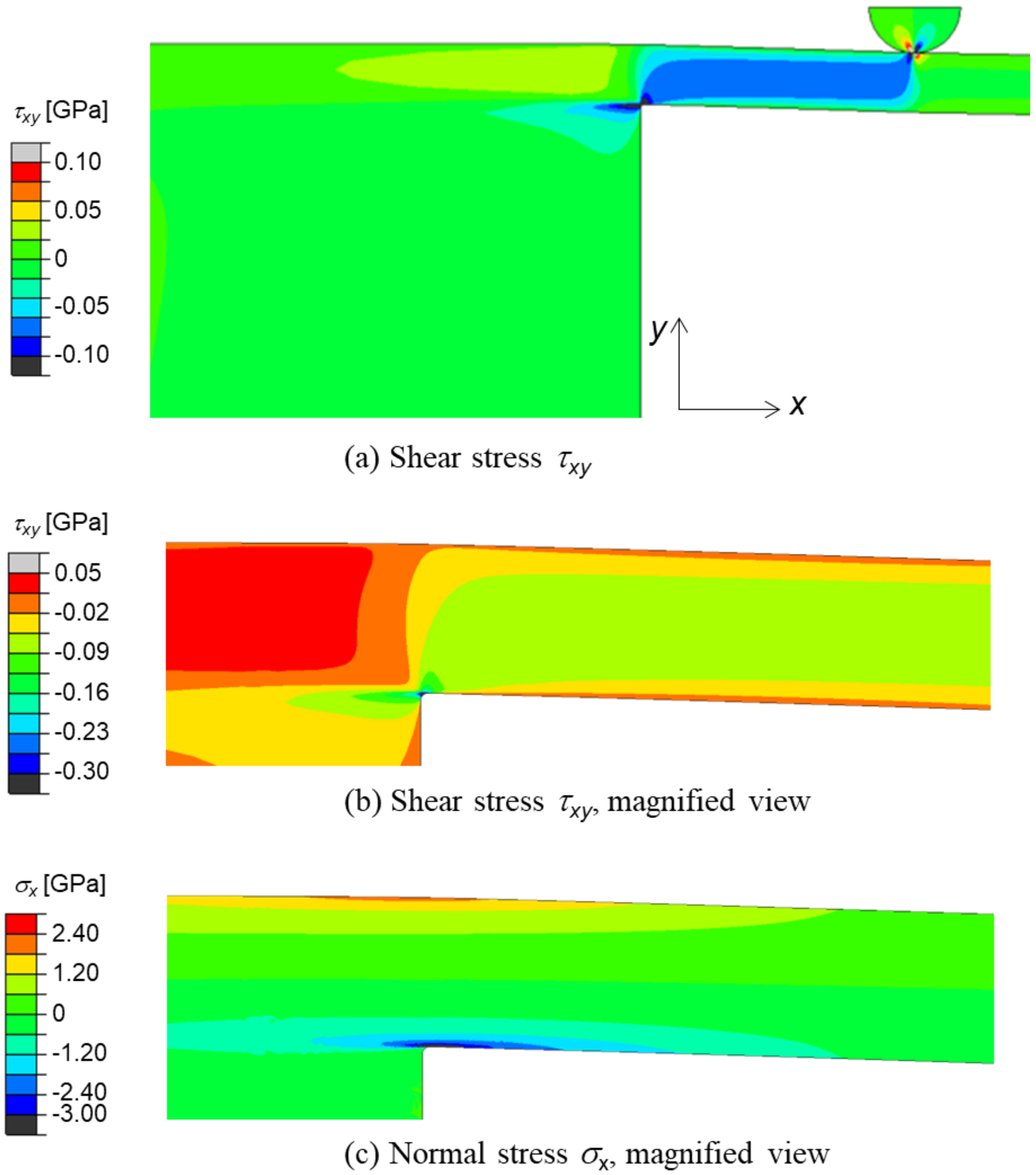

Fig. 2-10: Elastic stress distributions of cantilever specimen analyzed by FEM

Fig. 2-10 shows the elastic stress distributions in a cantilever specimen (Specimen 1). The images show the distributions of the shear stress, τ_{xy} (corresponding to the resolved shear stress between the layers) and the normal stress, σ_x (bending stress) at d = 50 nm. During cantilever bending, both shear and bending stresses occur. In vdW-layered materials, interlayer slip occurs in response to the shear stress. Therefore, the material nonlinearity that appeared during the cantilever bending tests could be attributed to a decrease in the stiffness because of interlayer slip. As shown in Figs. 2-10(a) and (b), the shear stress τ_{xy} that acted on the cantilever was not uniform, and a high stress concentration occurred near the bottom corner of the fixed end. Between the fixed end and the loading point, τ_{xy} was in effect over a wide region, and a high shear stress region formed along the longitudinal direction at the center. Therefore, during the loading process, interlayer slip occurred in the regions with a high shear stress, τ_{xy}, and the slipped region gradually expanded as the load was increased. As a result, a nonlinear *P*–*d* curve and a gradual decrease in the stiffness were observed.

Next, we discuss the self-restoration of the properties of the cantilever specimens upon unloading. Single-layer graphene is a covalently bonded sheet-like structure consisting of carbon atoms arranged in a hexagonal honeycomb lattice, while graphite has an AB stacking structure called the Bernal type, with vdW forces acting between the layers [32, 33]. It has been reported that the interlayer shear strength of AB-layered multilayer graphene is approximately 400–600 MPa [8, 34]. However, when interlayer slip occurs and the structure transitions to an incommensurate state, the shear strength becomes extremely small (for example, 40 kPa has been reported [35]), resulting in a superlubricated state [10, 34, 36]. During cantilever bending, once interlayer slip occurs because of deformation, the resistance to sliding at the mismatched interlayers reduces significantly owing to the formation of the superlubricated state [10, 34, 36]. Therefore, it is expected that a small driving force in the direction opposite to the loading direction would be able to restore a large deformation. For example, the generation of a new surface owing to localized interlayer slip results in a driving force large enough to ensure recovery

[11, 12]. However, as confirmed from the TEM images in Figs. 2-4, 2-5, and 2-8, the bending tests did not result in distinct new surfaces owing to localized slip deformation. Nevertheless, the deformation was restored almost completely upon unloading. As shown in Figs. 2-10(a) and 2-10(b), a high shear stress region formed within the cantilever away from the edge. Therefore, it can be assumed that a driving force for recovery was not activated by the generation of a new surface. On the other hand, as shown in Fig. 2-10(c), during cantilever bending, a large bending stress was generated near the fixed end of the cantilever, and the strain energy related to tension and compression in the in-plane direction was stored. In the regions with a high shear stress, energy was dissipated owing to the slippage between the layers. However, in the other regions, the stored strain energy was probably the driving force for recovery. In addition, the mismatched interlayers were in a state with a higher energy than that corresponding to the state of the commensurate or AB-stacked layers; this could also serve as the driving force for the recovery. Hence, it is likely that the deformation was restored because of these factors. Once the deformation was restored, the mechanical properties were also restored because of the restoration of the matched stacking structure.

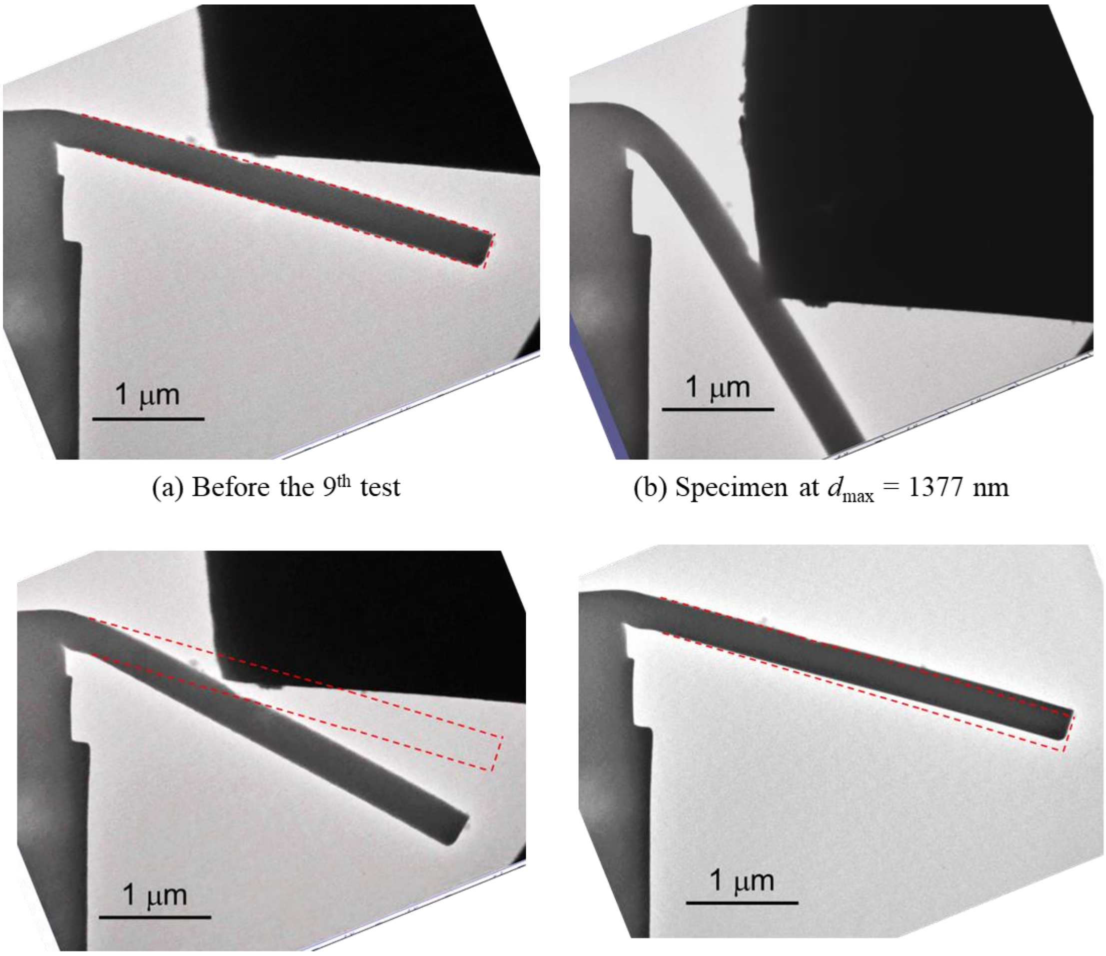

(a) Before the 9th test

(b) Specimen at d_{max} = 1377 nm

(c) After the test

(d) After electron-beam irradiation for 18.9 ks

Fig. 2-11: Restoration of deformation by electron-beam irradiation. TEM micrographs of loading tests for Specimen 4 show that the multilayer graphene cantilever is able to accommodate the large bending deformations without undergoing fracturing. The plastic deformation of the specimen is restored after it is subjected to the electron-beam irradiation process.

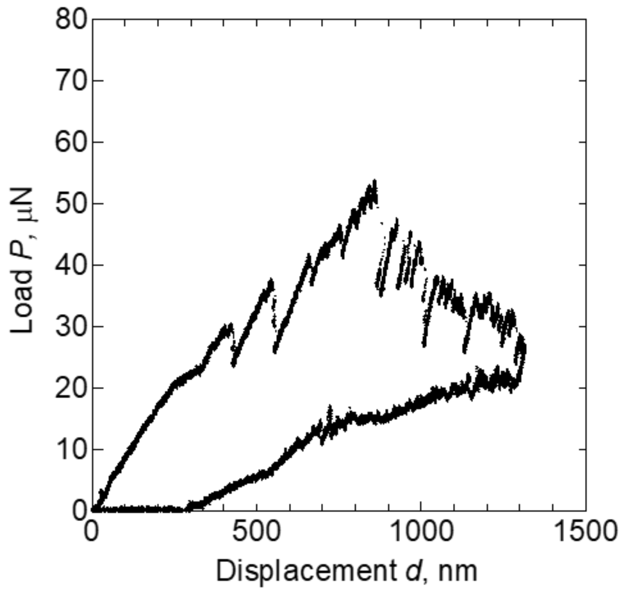

(e) P–d relationship for 9th test of Specimen 4

Fig. 2-11: Continued.

On the other hand, permanent deformation occurred in Stage 3. Because graphene is covalently bonded in the in-plane direction, it is difficult to break the covalent bonds by bending. In the case of the large deformation that occurs in Stage 3, a slight ripple is observed in the region near the bottom of the fixed end of the cantilever, as shown in Fig. 2-8(b). This feature may be attributed to the local buckling of the layered structure. The generation of the ripple releases the compressive stress [37, 38], which could have resulted in a decrease in strain energy or driving force of the recovery. This type of localized deformation, called ripplocation and kinking, occurs when a vdW-layered material such as HOPG is subjected to compressive loading in the in-plane direction [13, 39]. This type of deformation is accompanied by a high degree of interlayer slip and delamination [40] and may not be fully recovered. Furthermore, the presence of such ripples may increase the interlayer slip resistance [41], which could lead to permanent deformation. For these reasons, there is probably a threshold for the complete self-restoration of deformation.

2.3.6 Recovery of deformation by electron-beam irradiation

Fig. 2-11 shows the results of the 9th test (d_{max} = 1349 nm) for Specimen 4. Figs. 2-11(a)–(c) show TEM images obtained before the test, at d_{max}, and after the test, respectively. The red dashed line in each figure shows the outline of the cantilever before the test. As can be seen from Fig. 2-11(a), a plastic deformation with θ_{res} = 20.9° occurred during the 8th test. The corresponding P–d curve is shown in Fig. 2-11(e). P increased almost linearly with increasing d but exhibited large fluctuations from $d \approx 300$ nm onwards. This was caused by slippage between the indenter tip and the specimen. P reached its maximum value before d_{max} and then decreased. This was partly because of the change in the loading direction. The cantilever deformed significantly, as shown in Fig. 2-11(b), which increased the horizontal component of the load (x-direction component) and decreased the vertical component (y-direction component) measured by the device. Interestingly, even when the cantilever was deflected by θ_{max} = 62° (Fig. 2-11(b)), no distinct fracture was observed near the fixed end of the cantilever, as shown in Fig. S2-9. In other words, the graphite cantilever was able to accommodate large bending deformations without fracturing. During the unloading process, P decreased monotonically, as shown in Fig. 2-11(e), and the permanent deformation with θ_{res} = 30° ($d \approx 300$ nm) remained.

After the bending test, the cantilever specimen was subjected to electron-beam irradiation for 18,900 s (5.25 h). Fig. 2-11(d) shows a TEM image of the specimen after the electron-beam irradiation test, which demonstrates that the plastic deformation of the specimen was restored. The displacement was smaller than that before the 9th test, as shown in Fig. 2-11(a). In other words, the plastic deformation induced during the 8th test was partially recovered. The experimental results confirm that the bending deformation could be recovered even when the deformation was greater than that corresponding to the self-restoring capability of the cantilever samples. In contrast, the deformation was not restored in specimens that were not subjected to electron-beam irradiation. Because electron-beam irradiation by TEM can increase the temperature of the test specimen [22, 42], it is possible that temperature acted as a driving force for recovery; that is, the deformation of the plastically deformed cantilever was recovered gradually over time owing to thermally activated processes. To investigate whether the recovery observed under electron-beam irradiation was caused by temperature or other factors, the temperature rise under the irradiation conditions of this TEM experiment was quantitatively estimated by thermal conduction analysis using FEM (Supplementary Material S2.10). The results indicated that the maximum temperature rise in the specimen was approximately 2.0 K. Therefore, it was inferred that the deformation recovery was not due to heat.

Another possibility for why this remarkable deformation recovery occurred under electron-beam irradiation is that a change in the mechanical properties occurred owing to electron-beam irradiation [43, 44]. The effect of electron-beam irradiation on time-dependent deformation behavior has been observed previously, such as during creep tests of Si [45] and ZnO [46]. In these studies, the creep of Si and ZnO micro-specimens was accelerated during *in situ* SEM, which subjected the samples to electron-beam irradiation under low accelerating voltage. The change in behavior could not be explained by thermal effects alone, because the temperature rise was negligibly small in these tests. It is thought that excess electrons and/or holes induced by electron-beam irradiation altered the state of the interatomic bonds [47, 48], thereby changing the creep characteristics. During the out-of-plane bending deformation of vdW-layered materials such as HOPG, the recombination of covalent bonds is not likely to occur, and the plastic deformation is mainly caused by the slip between the vdW layers. However, it is thought that electron-beam irradiation may affect the interactions between the layers in HOPG, changing the time-dependent deformation characteristics and accelerating the recovery of plastic deformation. Determining the detail and mechanism of this phenomenon remains an intriguing issue, which requires further investigation.

2.4 Conclusions

In situ TEM bending tests were performed on submicron-sized cantilever specimens prepared by FIB to determine the bending deformation characteristics and self-restoring properties of submicron-sized graphite. The results obtained can be summarized as follows:

The loading–unloading curves were nonlinear, indicative of reversible behavior, and contained a large hysteresis loop. Moreover, similar loading–unloading curves were obtained during multiple loading tests performed on the same specimen, indicating that the mechanical properties of the specimens were restored upon unloading, even in the case of large nonlinear deformations. As the deformation increased, plastic deformation occurred, and the self-restoration property was lost. However, no clear fracture was observed in the cantilevers even when they were deformed to a deflection angle of 62º. Furthermore, the plastic deformation recovered with time owing to a temperature increase when the specimens were subjected to electron-beam irradiation by TEM. Based on the experimental results, the mechanisms of nonlinear deformation and its self-restoration were discussed. The nonlinearity of the load–displacement curves can probably be ascribed to a reduction in the stiffness because of the occurrence and propagation of interlayer slip in the high shear stress region. On the other hand, the bending deformation led to the storage of the in-plane tensile and compressive strain energy, resulting in a driving force for the self-restoration of the deformation during the unloading process. The results of this study confirmed that vdW-layered materials can accommodate large out-of-plane bending deformations without fracturing and that these deformations are reversible. As a result, these materials exhibit high durability against repeated loading.

References

[1] L.C. Blackman, and A.R. Ubbelohde, Stress recrystallization of graphite, *Proc. R. Soc. Lond. A* **266**, 20 (1962).

[2] A. W. Moore, A. R. Ubbelohde, and D. A. Young, Stress recrystallization of pyrolytic graphite, *Proc. R. Soc. Lond. A* **280**, 153 (1964).

[3] B. Dai, L. Fu, Z. Zou, M. Wang, H. Xu, S. Wang, and Z. Liu, Rational design of a binary metal alloy for chemical vapour deposition growth of uniform single-layer graphene, *Nat. Commun.* **2**, 522 (2011).

[4] J. Hass, W. A. de Heer, and E. H. Conrad, The growth and morphology of epitaxial multilayer graphene, *J. Phys. Condens. Mat.* 20, 323202 (2008).

[5] H. J. Shin, K. K. Kim, A. Benayad, S.M. Yoon, H.K. Park, I.S. Jung, M.H. Jin, H.K. Jeong, J.M. Kim, J.Y. Choi, and Y.H. Lee, Efficient reduction of graphite oxide by sodium borohydride and its effect on electrical conductance, *Adv. Funct. Mater.* **19**, 1987 (2009).

[6] C. Y. Su, A. Y. Lu, Y. P. Xu, F. R. Chen, A. N. Khlobystov, and L. J. Li, High-quality thin graphene films from fast electrochemical exfoliation, *Acs Nano* **5**, 2332 (2011).

[7] E. M. Han, J. Yu, E. Annevelink, J. Son, D. A. Kang, K. Watanabe, T. Taniguchi, E. Ertekin, P. H. Y. Huang, and A. M. van der Zande, Ultrasoft slip-mediated bending in few-layer graphene, *Nat. Mater.* **19**, 305 (2020).

[8] F. Pan, G. R. Wang, L. Q. Liu, Y. L. Chen, Z. Zhang, X. and H. Shi, Bending induced interlayer shearing, rippling and kink buckling of multilayered graphene sheets, *J. Mech. Phys. Solids* **122**, 340 (2019).

[9] G. R. Wang, Z. H. Dai, J. K. Xiao, S. Z. Feng, C. X. Weng, L. Q. Liu, Z. P. Xu, R. Huang, and Z. Zhang, Bending of multilayer van der Waals materials, *Phys. Rev. Lett.*

123, 116101 (2019).

[10] D. M. Tang, D. G. Kvashnin, S. Najmaei, Y. Bando, K. Kimoto, P. Koskinen, P. M. Ajayan, B. I. Yakobson, P. B. Sorokin, J. Lou, and D. Golberg, Nanomechanical cleavage of molybdenum disulphide atomic layers, *Nat. Commun.* **5**, 3631 (2014).

[11] Z. Liu, J. R. Yang, F. Grey, J. Z. Liu, Y. L. Liu, Y. B. Wang, Y. L. Yang, Y. Cheng, and Q. S. Zheng, Observation of microscale superlubricity in graphite, *Phys. Rev. Lett.* **108**, 20 (2012).

[12] Z. Liu, S. M. Zhang, J. R. Yang, J. Z. Liu, Y. L. Yang, Q. S. Zheng, Interlayer shear strength of single crystalline graphite, *Acta Mech. Sinica-Prc* **28**, 978 (2012).

[13] M. W. Barsoum, A. Murugaiah, S. R. Kalidindi, T. Zhen, and Y. Gogotsi, Kink bands, nonlinear elasticity and nanoindentations in graphite, *Carbon* **42**, 1435 (2004).

[14] J. Mayer, L. A. Giannuzzi, T. Kamino, and J. Michael, TEM sample preparation and FIB-induced damage, *MRS Bull.* **32**, 400 (2007).

[15] S. Rubanov and P. R. Munroe, FIB-induced damage in silicon, *J. Microscopy* **214**, 213 (2004).

[16] B. S. Archanjo, I. O. Maciel, E. H. M. Ferreira, S. B. Peripolli, J. C. Damasceno, C. A. Achete, and A. Jorio, Ion beam nanopatterning and micro-raman spectroscopy analysis on HOPG for testing FIB performances, *Ultramicroscopy* **111**, 1338 (2011).

[17] W. Li, G. J. Cheng, Y. R. Liang, B. Y. Tian, X. L. Liang, L. M. Peng, A. R. H. Walker, D. J. Gundlach, and N. V. Nguyen, Broadband optical properties of graphene by spectroscopic ellipsometry, *Carbon* **99**, 348 (2016).

[18] J. Takahashi and T. Makino, Raman-Scattering measurement of silicon-on-insulator substrates formed by high-dose oxygen-ion implantation, *J. Appl. Phys.* **63**, 87 (1988).

[19] I. DeWolf, Micro-Raman spectroscopy to study local mechanical stress in silicon

integrated circuits, *Semicond*. *Sci*. *Tech*. **11**, 139 (1996).

[20] M. Lasithiotakis, J. T. Marrow, and B. J. Marsden, Evaluation of damage induced in graphite due to sample preparation by standard non-destructive techniques, *Mater*. *Phys*. *Mech*. **44**, 271 (2020).

[21] A. V. Krasheninnikov and K. Nordlund, Ion and electron irradiation-induced effects in nanostructured materials, *J*. *Appl*. *Phys*. **107**, 071301 (2010).

[22] R. F. Egerton, P. Li, and M. Malac, Radiation damage in the TEM and SEM, *Micron* **35**, 399 (2004).

[23] D. Teweldebrhan and A.A. Balandin, Modification of graphene properties due to electron-beam irradiation, *Appl*. *Phys*. *Lett*. **94**, 013101 (2009).

[24] A. Chartier, L. Van Brutzel, B. Pannier, and P. Baranek, Atomic scale mechanisms for the amorphisation of irradiated graphite, *Carbon* **91**, 395 (2015).

[25] J. H. Warner, M. H. Rummeli, L. Ge, T. Gemming, B. Montanari, N. M. Harrison, B. Buchner, and G. A. D. Briggs, Structural transformations in graphene studied with high spatial and temporal resolution, *Nat. Nanotech.* **4**, 500 (2009).

[26] S. Y. Peng and Y. J. Wei, On the influence of interfacial properties to the bending rigidity of layered structures, *J*. *Mech*. *Phys*. *Solids* **92**, 278 (2016).

[27] A. Bosak, M. Krisch, M. Mohr, J. Maultzsch, and C. Thomsen, Elasticity of single-crystalline graphite: Inelastic x-ray scattering study, *Phys*. *Rev B* **75**, 153408(2007).

[28] Y. L. Liu, Z. P. Xu, and Q. S. Zheng, The interlayer shear effect on graphene multilayer resonators, *J*. *Mech*. *Phys*. *Solids* **59**, 1613 (2011).

[29] E. M. Han, J. Yu, E. Annevelink, J. Son, D. A. Kang, K. Watanabe, T. Taniguchi, E. Ertekin, P. H. Y. Huang, A. and M. van der Zande, Ultrasoft slip-mediated bending in few-layer graphene, *Nat*. *Mater*. **19**, 305 (2020).

[30] X. J. Ma, L. Q. Liu, Z. Zhang, and Y. G. Wei, A Method to Determine the Geometry-Dependent Bending Stiffness of Multilayer Graphene Sheets, *J. Appl. Mech.* **88**, 011004 (2021).

[31] X. M. Chen, C. L. Yi, and C. H. Ke, Bending stiffness and interlayer shear modulus of few-layer graphene, *Appl. Phys. Lett.* **106**, 101907 (2015).

[32] M. Aoki and H. Amawashi, Dependence of band structures on stacking and field in layered graphene, *Solid State Commun.* **142**, 123 (2007).

[33] Y. K. Shen and H. A. Wu, Interlayer shear effect on multilayer graphene subjected to bending, *Appl. Phys. Lett.* **100**, 101909 (2012).

[34] L. Ruiz, W. J. Xia, Z. X. Meng, and S. Keten, A coarse-grained model for the mechanical behavior of multi-layer graphene, *Carbon* **82**, 103 (2015).

[35] G. R. Wang, Z. H. Dai, Y. L. Wang, P. H. Tan, L. Q. Liu, Z. P. Xu, Y. G. Wei, R. Huang, and Z. Zhang, Measuring interlayer shear stress in bilayer graphene, *Phys. Rev. Lett.* **119**, 036101 (2017).

[36] Y. F. Guo, W. L. Guo, and C. F. Chen, Modifying atomic-scale friction between two graphene sheets: A molecular-force-field study, *Phys. Rev. B* **76**, 155429 (2007).

[37] A. Kushima, X. F. Qian, P. Zhao, S. L. Zhang, and J. Li, Ripplocations in van der Waals layers, *Nano Lett.* **15**, 1302 (2015).

[38] D. Vella, A. Boudaoud, and M. Adda-Bedia, Statics and inertial dynamics of a ruck in a rug, *Phys. Rev. Lett.* **103**, 174301 (2009).

[39] I. Nikiforov, D. M. Tang, X. L. Wei, T. Dumitrica, and D. Golberg, Nanoscale bending of multilayered boron nitride and graphene ribbons: Experiment and objective molecular dynamics calculations, *Phys. Rev. Lett.* **109**, 025504 (2012).

[40] M.W. Barsoum, X. Zhao, S. Shanazarov, A. Romanchuk, S. Koumlis, S. J. Pagano,

L. Lamberson, and G.J. Tucker, Ripplocations: A universal deformation mechanism in layered solids, *Phys*. *Rev*. *Mater*. **3**, 013602 (2019).

[41] S. Y. Zhao, Y. Y. Zhang, J. Yang, and S. Kitipornchai, Improving interfacial shear strength between graphene sheets by strain-induced wrinkles, *Carbon* **168**, 135 (2020).

[42] L. Reimer, Scanning Electron Microscopy: Physics of image formation and microanalysis, *Springer*, (1998).

[43] K. Zheng, C. C. Wang, Y. Q. Cheng, Y. H. Yue, X. D. Han, Z. Zhang, Z. W. Shan, S. X. Mao, M. M. Ye, Y. D. Yin, and E. Ma, Electron-beam-assisted superplastic shaping of nanoscale amorphous silica, *Nat*. *Commun*. **1**, 24 (2010).

[44] S. Dai, J. Zhao, L. Xie, Y. Cai, N. Wang, and J. Zhu, Electron-beam-induced elastic-plastic transition in Si nanowires, *Nano Lett*. **12**, 2379 (2012).

[45] H. Hirakata, K. Konishi, T. Kondo, and K. Minoshima, Electron-beam enhanced creep deformation of amorphous silicon nano-cantilever, *J*. *Appl*. *Phys*. **126**, 105102 (2019).

[46] Y. J. Kim, W. W. Lee, I. C. Choi, B. G. Yoo, S. M. Han, H. G. Park, W. I. Park, and J. I. Jang, Time-dependent nanoscale plasticity of ZnO nanorods, *Acta Mater*. **61**, 7180 (2013).

[47] H. Hirakata, K. Sano, and T. Shimada, Electron-beam irradiation alters bond strength in zinc oxide single crystal, *Appl*. *Phys*. *Lett*. **116**, 111902 (2020).

[48] S. J. Woo and Y. W. Son, Ideal strength of doped graphene, *Phys*. *Rev*. *B* **87**, 075419 (2013).

Chapter 3

Analyzing the bending deformation of van der Waals-layered materials by a semi-discrete layer model

3.1 Introduction

As shown in Chapter 2, bending tests [1] on submicron-sized HOPG cantilevers fabricated using a FIB revealed that they exhibited a characteristic nonlinear deformation in which the stiffness decreased as deformation progressed, and the cantilevers accommodated large bending deformations without fracturing. However, the deformation was almost completely restored upon unloading, thus resulting in a hysteresis loop. In bending tests on microsized Bi_2Te_3 [2] and $MoTe_2$ [3] cantilevers, localized interlayer slips were observed, and the number of slips increased as the deformation progressed. Furthermore, shear loading tests on microsized graphite mesas revealed that when an interlayer slip occurred under loading, the interlayer entered an incommensurate state or a super-lubricated state with an extremely low shear resistance, and this slip was spontaneously restored when the load was released [4, 5]. These results indicate that vdW-layered materials can accommodate large nonlinear bending deformations without fracturing and undergo self-restoration upon unloading.

It is assumed that localized and discrete interlayer slips play an important role in the mechanism of this characteristic deformation. In addition, interlayer slips are considered to preferentially occur between incommensurate interlayers [6]. Therefore, modeling considering discrete interlayer slips is effective to construct a universal mechanical model that describes the nonlinear bending deformation characteristics, exhibits a hysteresis loop, and self-restores upon unloading in vdW-layered materials. Up to our knowledge, such a mechanical model has not yet been reported, although several theoretical models [7–14] for the bending deformation of vdW-layered materials have been proposed.

This chapter reports the development of a mechanical model that reproduces the characteristic nonlinear and reversible deformation of vdW-layered materials by considering the microscopic mechanisms (discrete interlayer slips). The vdW-layered material is modeled as a stack of interacting discrete deformable layers (semi-discrete layer model), and the interlayer interaction is modeled using a CZM that reproduces the localized interlayer slip. A bending deformation analysis based on the mechanical model is performed using the FEM for the out-of-plane bending deformations in HOPG and $MoTe_2$, which are typical vdW-layered materials, and the validity of the model is discussed by comparing it with experimental results. The results demonstrate that the designed model reproduced well the out-of-plane bending deformation of the vdW-layered materials.

3.2 Experimental observations of the bending deformation of vdW-layered materials

Fig. 2-1(a) showed a schematic illustration of the specimen and loading method. Typical vdW-layered materials, HOPG (ZYA-DS, Tips Nano Co.) and $MoTe_2$ (single-crystal 2H-phase $MoTe_2$, 2D Semiconductors), were used as target materials. Considering that the anisotropy of deformation properties (i.e., the ratio of the elastic constants C_{11} to C_{44}) affects the onset and propagation of interlayer slips under bending deformation, two types of materials with significantly different C_{11} / C_{44} ratios were selected. The C_{11} / C_{44} values for HOPG and $MoTe_2$ are 224 and 6.8, respectively.

Figs. 3-1(a)-(c) show the typical bending deformation characteristics [1, 3] of HOPG in Chapter 2 and $MoTe_2$ cantilevers obtained by FIB from bulk vdW-layered materials. Details of the experiment for $MoTe_2$ is shown in Supplementary Material S3.1. The load-displacement (*P*–*d*) graph for the submicron HOPG cantilever (Fig. 3-1(a)), became nonlinear, thus accommodating a large bending deformation. In the linear region at the initial stage of deformation, the experimental results were in accordance with the FEM stress analysis solution, assuming a continuum (linear elastic body). Subsequently, it significantly deviated from the linear elastic solution and exhibited a nonlinear deformation. Unloading resulted in the formation of a hysteresis loop and in restoring of most of the deformation [1]. The deformation was reversible, and similar *P*–*d* relationships were observed upon repeatedly loading the same specimen. The hysteresis loops associated with this nonlinear deformation were considered to be due to energy dissipation accompanying the occurrence and propagation of interlayer slips. Fig. 3-1(b) shows the bending deformation results [3] of the micro $MoTe_2$ cantilever. Increasing d resulted in a linear increase in P followed by its intermittent decrease. Most of the deformation was restored by unloading. Fig. 3-1(c) shows the scanning electron microscopy (SEM) image of the side of the $MoTe_2$ specimen observed after further deformation. White lines owing to localized discrete interlayer slips were observed on the side surface, indicating that the large bending deformation was caused by discrete interlayer slips. The rapid decrease in P corresponded to the onset and propagation of localized interlayer slip.

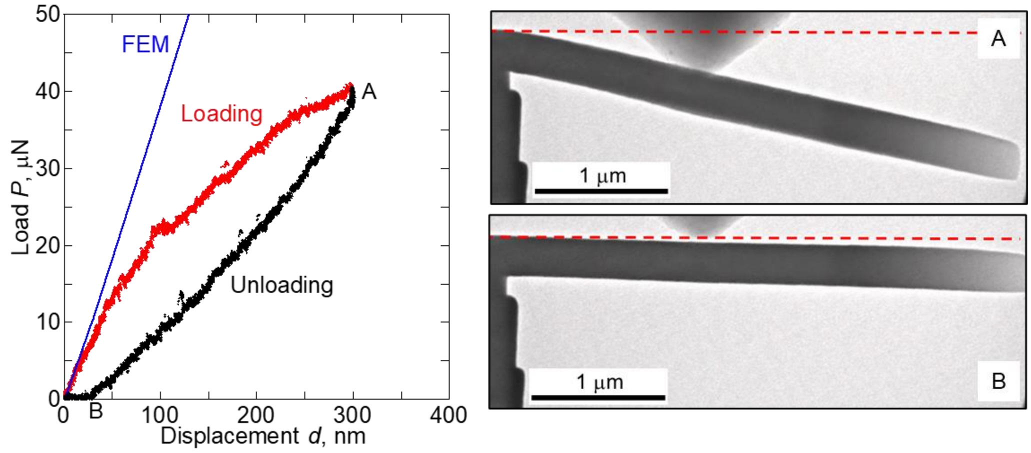

(a) HOPG submicron-cantilevers: *P*–*d* relationship and TEM images. The red dashed lines in the TEM images indicate the top surface of the specimen before deformation.

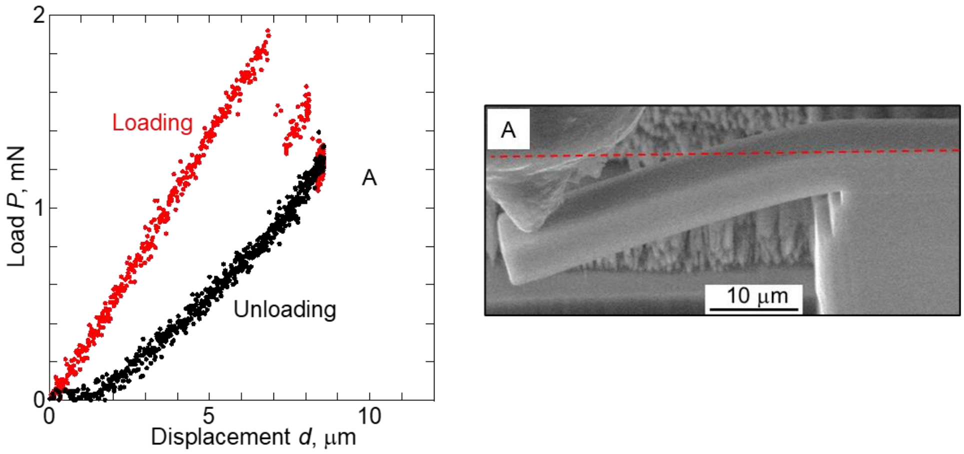

(b) $MoTe_2$ micro-cantilever: *P*–*d* relationship and SEM image. The red dashed line in the SEM image indicates the top surface of the specimen before deformation.

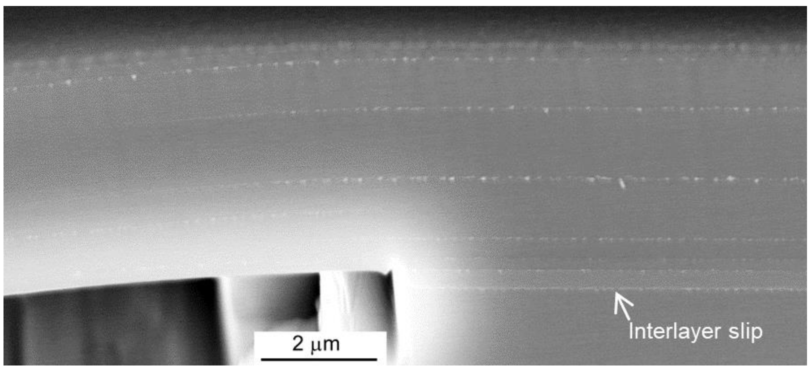

(c) Enlarged view of the side of the $MoTe_2$ cantilever near the fixed end

Fig. 3-1: Typical experimental results of cantilever bending of vdW-layered materials

The above results showed that vdW-layered materials can undergo large bending deformations without fracturing, and that most of the deformation can be restored upon unloading. The main deformation mechanism in the nonlinear regime was the discrete interlayer slip. The reversibility of the deformation is attributed to the reversibility of the vdW interactions between the layers. Owing to these characteristics, it is effective to model vdW-layered materials as a stack of interacting discrete deformable layers (semi-discrete layer model) to universally reproduce the deformation characteristics of vdW-layered materials.

3.3 Analysis method

3.3.1 Mechanical model of the vdW-layered materials (semi-discrete layer model)

Localized interlayer slips occurred in the bending tests of the $MoTe_2$ [3] and Bi_2Te_3 [2] cantilevers and the regions between these slips deformed in a continuum-like manner. Therefore, we assumed that the bending deformation of vdW-layered materials is dominated by the elastic deformation of the deformable layers and the interactions between them. Fig. 3-2 illustrates the concept of the mechanical model. A vdW-layered material was modeled as a stack of deformable layers (anisotropic linear elastic bodies, height h_n) with vdW interactions between the deformable layers (Fig. 3-2(a)). The vdW interaction for the interlayer slip was modeled using the CZM.

Figs. 3-2(b) and 3-2(c) show the CZMs between the layers. In both models, as the sliding distance (δ_T) increased, the interlayer shear stress (τ_T) increased linearly up to the maximum interlayer shear stress (τ_{Tm}) at $\delta_T = \delta_{Tm}/2$, and then τ_T linearly decreased to τ_T

= 0 at $\delta_T = \delta_{Tm}$. For $\delta_T > \delta_{Tm}$, we employed two types of models, designated as the fracture model and recombination model (Figs. 3-2(b) and 3-2(c), respectively). In the 'fracture model' the interlayer fractures, or $\tau_T = 0$ for $\delta_T > \delta_{Tm}$. In the 'recombination model', the interlayer was restored to its original state (recombined) at $\delta_T = \delta_{Tm}$. For each increase in δ_T with δ_{Tm}, the same constitutive equation was applied. However, in the presence of tensile stress (delamination stress in the out-of-plane direction) between the layers, recombination did not occur, assuming that the shear interaction disappeared owing to delamination. Recombination was also applied to the interlayer slip in the reverse direction during the unloading process. Details of the constitutive equations for unloading are provided in the Supplementary Material S3.2.

In the MD analysis of the interlayer shear deformation of graphene sheets [9], the shear resistance force is approximately represented by a triangular wave, so it is reasonable to approximate it by a simple triangular wave. Two types of *P-d* relationships with different characteristics depending on the material were obtained in bending deformation experiments of vdW-layered materials, HOPG and $MoTe_2$, as shown in Fig. 3-1. Assuming that this difference in behavior is due to the difference in interlayer slip behavior, there are two cases: one in which slip resistance is maintained (or recombined) even if interlayer slip occurs, and the other in which slip resistance disappears (or fractures) once the interlayer slip occurs. For this reason, the two CZM models (fracture and recombination models) shown in Fig. 3-2 were considered.

The out-of-plane interaction related to delamination was modeled using a nonlinear spring whose contact stiffness (k_N) varied with the delamination distance (δ_N). Fig. 3-2(d) shows an example of the δ_N–k_N relationship (HOPG). The nonlinear spring produces a contact stress that is k_N multiplied by δ_N, and there is no essential difference from using

CZM (relationship between delamination distance and stress). The nonlinear spring model can reproduce both attractive and repulsive forces depending on the positive and negative δ_N. In this model, the sign of δ_N was defined as positive in the direction of delamination, and the contact stress was defined as positive in the direction of repulsion. Therefore, in order for an attractive force (negative contact stress) to act against a positive δ_N, k_N becomes negative. The out-of-plane interactions were independent of the in-plane interactions. For example, even if the interlayer slip progressed to a fracture state of τ_T = 0, k_N corresponding to δ_N continued to act in the out-of-plane direction. The out-of-plane interactions were independent of the in-plane interactions. For example, even if the interlayer slip progressed to a fracture state of $\tau_T = 0$, k_N corresponding to δ_N continued to act in the out-of-plane direction. The reason for this setting is that in the vdW-layered materials, even if interlayer slip occurs, if the interlayer distance in the out-of-plane direction is maintained, the interaction in the out-of-plane direction is maintained. Conventional mixed-mode CZM [15] does not reproduce the characteristics because fracture occurs whether it is due to interlayer delamination or interlayer slip.

The material constants τ_{Tm} and δ_{Tm} of the CZMs and h_n of the deformable layer were empirically fitted based on the experimental results. In HOPG, the elastic constants for the deformable layer are the values for the single crystal graphite [16], C_{11} = 1109 GPa, C_{12} = 139 GPa, C_{13} = 0 GPa, C_{33} = 38.7 GPa, C_{44} = 4.95 GPa, and C_{66} = 485 GPa. h_n corresponds to the interval at which the localized interlayer slips occurs, and the range was set to $h_n > 30$ nm. This is based on the spacing of the grain boundaries observed by the TEM of HOPG [6], where interlayer slips are likely to occur. In the MD analysis of the interlayer shear deformation of graphene sheets [9], when the commensurate graphene sheets were slid in the zigzag direction, the shear resistance force changed in a sinusoidal manner (almost triangular wave) with a maximum shear force of 0.015 nN/atom and a period of 0.2425 nm. Multiplying the shear force by the area density of the carbon atom $d_c = 4/(3\sqrt{3}l_{c-c}^2)$ resulted in a τ_{Tm} of 589 MPa and δ_{Tm} of 0.1212 nm, where $l_{c\text{-}c}$ is the C–C bond length. On the other hand, Liu et al. [4, 5] evaluated by shear loading experiments the shear strength of graphite mesa to be ~100 MPa. Since τ_{Tm} = 589 MPa corresponds to the ideal strength, we set τ_{Tm} in the range of 100–589 MPa.

For the out-of-plane interaction, the relationship between the k_N and δ_N (Fig. 3-2(d)) was determined to reproduce the relationship between the cohesive force in the out-of-plane direction and δ_N obtained by the MD analysis of the delamination [9].

In $MoTe_2$, the elastic constants of the deformable layer are C_{11} = 123 GPa, C_{12} = 28 GPa, C_{13} = 9 GPa, C_{33} = 37 GPa, C_{44} = 18 GPa, and C_{66} = 47 GPa [17]. The experimental results (Fig. 3-1(c) [3] revealed the presence of traces of the localized interlayer slip in the stacking direction at intervals of ~0.2–1 μm. The h_n of the deformable layer was set to be > 0.2 μm. The theoretical analysis based on the first-principles calculations [18] evaluated the ideal shear strength for the interlayer slip to be 1040 MPa. Although there are no experimental evaluations, the τ_{Tm} was set to be < 1040 MPa, assuming that similar to HOPG, the actual strength is much smaller than the ideal strength. From the lattice constant of $MoTe_2$ of 0.3551 nm [19], δ_{Tm} was assumed to be > 0.1776 nm. The theoretical analysis [18] showed that the in-plane shear strength of $MoTe_2$ was roughly twice that of HOPG. Since there are no evaluations on the out-of-plane interaction of $MoTe_2$, k_N was assumed to be twice that of HOPG.

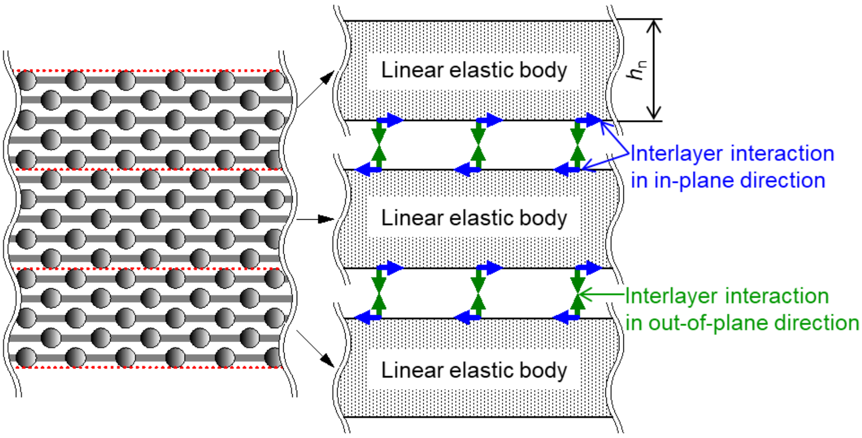

(a) Modeling of the vdW-layered material

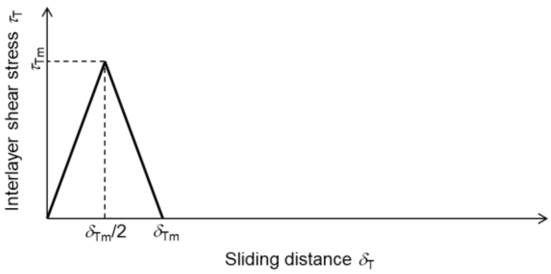

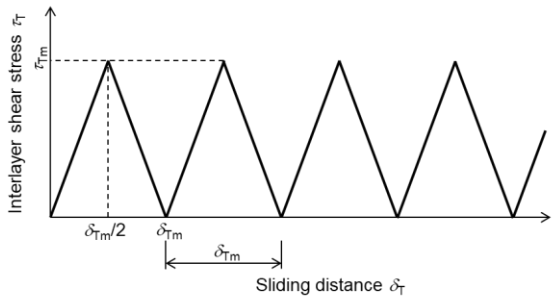

(b) Fracture model,
CZM of the in-plane interaction

(c) Recombination model,
CZM of the in-plane interaction

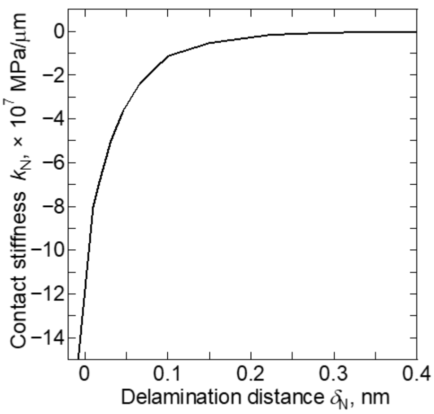

(d) Non-linear spring model for out-of-plane interaction, relation between k_N and δ_N

Fig. 3-2: Semi-discrete layer model: Mechanical model of the interacting discrete deformable layers simulating the deformation of vdW-layered materials. The interaction between layers was modeled by CZM.

3.3.2 Analysis models and conditions

FEM analyses introducing the mechanical model of vdW-layered materials were performed, and the validity of the model was verified by comparing it with experimental results. ANSYS (2022) Student, a general-purpose finite-element analysis software, was used for the analyses. Because the displacement velocities in the experiments were small, all FEM analyses were quasi-static nonlinear analyses (implicit solution method). Geometric nonlinearity was considered. Details of the solution steps and convergence criteria for the nonlinear problems in FEM analysis are shown in Supplementary Material S3.3.

a. Cantilever bending

Fig. 3-3(a) shows the analytical model of the HOPG cantilever where the height direction (y-direction) of the deformable layer is the stacking direction of HOPG and the longitudinal direction of the cantilever is along the x-direction. The deformation in the xy-plane of the specimen was targeted for analysis, and a plane strain was assumed. The dimensions of the model simulated experimental specimens. For example, in the model shown in Fig. 3-3(a), the height (h) and length (L) of the cantilever were set to 0.33 μm and 3.42 μm, respectively, and three deformable layers with $h_n = h/N$ (= 0.11 μm, $N = 3$, where N is the number of layers) were stacked. The shape of the model was a rectangle with a width of $2L = 6.84$ μm and a height of $h = 0.33$ μm. The displacement in the y-direction of the bottom ($y = 0$) in the half-length of the model ($x = 0$–L) was constrained to simulate a cantilever of length L. A plane-strain element (6-nodes triangular quadratic element) was used in the FEM analysis. The CZM and nonlinear spring model were set on all the contact surfaces between the deformable layers. The element size was set to approximately 10 nm. The diamond indenter was modeled as a semicircle with a radius of 0.25 μm and the loading point was set to L_p = 1.56 μm from the fixed end of the cantilever (x = L). During the loading process, the indenter was displaced in the y-direction to a maximum displacement (d_{max}) and was returned to d = 0 nm during the unloading process. The indenter was assumed to be an isotropic linear elastic body with a Young's modulus of 1140 GPa and Poisson's ratio of 0.07. Frictionless contact was assumed between the indenter and the specimen.

Fig. 3-3(b) shows the analytical model of the $MoTe_2$ cantilever. The model simulated a cantilever with an h = 4.5 μm and L = 36.4 μm and comprised 10 deformable layers (N = 10, h_n = 0.45 μm). The outline of the model was similar to that of HOPG; however, a rectangular region with an L and h (the same linear elastic body as the deformable layer) was provided below the left side of the fixed end. The element size was set to approximately 150 nm. To simulate the experiment, L_p = 32 μm was used in this model, and the radius of the indenter was set to 1 μm.

b. Pure bending

The deformation characteristics of the HOPG plates under pure bending (uniform curvature) were analyzed using a mechanical model validated by the cantilever analysis. In particular, the effect of the specimen size on the deformation properties was investigated. Fig. 3-3(c) shows the analytical model. Considering geometrical symmetry, half of the plate (half-length L) was modeled, and the displacement in the x-direction of the symmetry plane (x = 0) was constrained. The ratio of h/L was fixed to 1/25, and three models with similarly varying specimen sizes were created. The height of the deformable layer was held constant at h_n = 0.1 μm and the number of layers was set to N = 3, 5, and

7 for h = 0.3, 0.5, and 0.7 μm, respectively. N was set to an odd number (3, 5, and 7) so that the neutral axis was in the deformable layer. Fig. 3(c) shows the analysis model for N = 3. To apply a uniform curvature to the model, a displacement of the curvature radius (ρ) was applied to the neutral axis (red line in the figure). The neutral axis did not stretch nor shrink, thus producing a pure bending deformation. ρ was applied from the maximum value ρ_{max} to the minimum value ρ_{min} and then back to ρ_{max}. The bending moment (M_z) generated in the plane of symmetry was determined, and the bending stiffness (D) = ρM_z was evaluated. The analysis was divided into four ρ regions: [ρ_{max}, ρ_{min}] = [30 L, 20 L], [20 L, 10 L], [10 L, 8 L], and [8 L, 6 L]. The reason why the analysis was divided into four region was to understand the unloading characteristics.

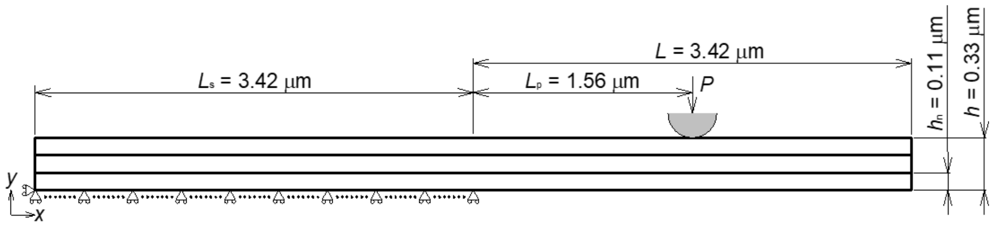

(a) HOPG cantilever model: N = 3, L = 3.42 μm, h = 0.33 μm

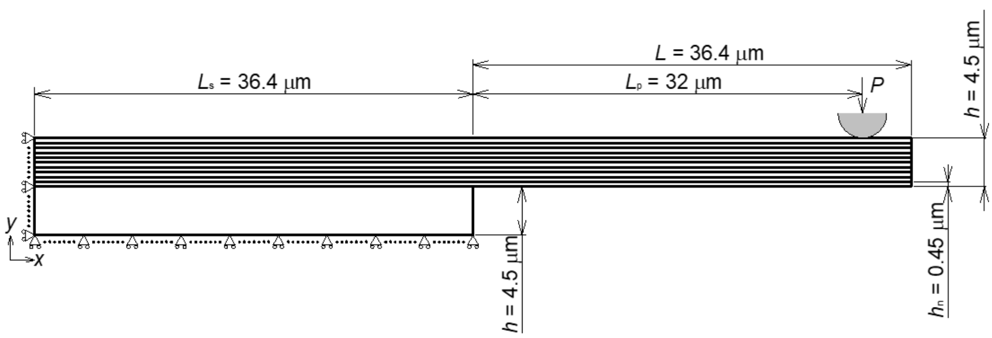

(b) $MoTe_2$ cantilever model: N = 10, L = 36.4 μm, h = 4.5 μm

Fig. 3-3: FEM analysis models

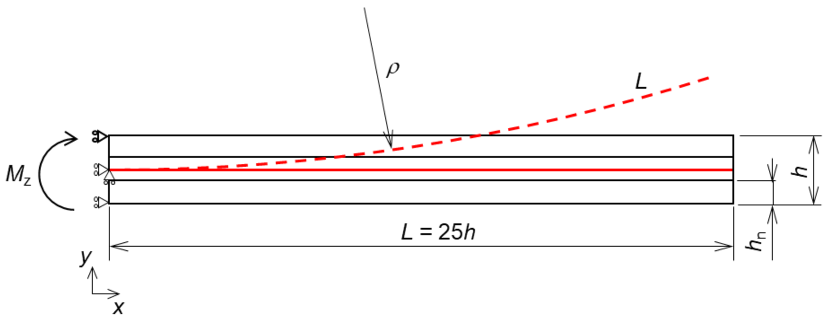

(c) HOPG model for pure bending: $N = 3$

Fig. 3-3: Continued.

3.4 Results and discussions

3.4.1 Deformation of the HOPG cantilevers

a. Fracture model

Fig. 3-4 shows the results of the semi-discrete layer model (CZM: fracture model, $N = 3$, $h_n = 0.11$ μm, $\tau_{Tm} = 100$ MPa) for the HOPG cantilever. The P–d relationship (Fig. 3-4(a)) revealed that in the initial stage of loading P increased linearly with an increase in d. At d ~40 nm, P rapidly decreased from 14.1 to 5.06 μN, and the slope decreased by approximately 65%. Thereafter, P increased linearly until a d_{max} of 166 nm was attained. The unloading process was linear throughout the entire region, and plastic deformation did not occur. Fig. 3-4(b) shows the deformed shape at a d_{max} of 166 nm. The vicinity of the fixed end of the cantilever was bent, and the other region of the cantilever was almost straight. Interlayer slips clearly occurred in both interlayers, thus resulting in surface steps of approximately 13 nm at the free end of the cantilever.

The distributions of τ_T and δ_T before and after the rapid decrease in P are shown in Figs. 3-4(c) and 3-4(d), respectively. A positive/negative δ_T indicates that the upper surface slid to the right or left relative to the lower surface, and the sign of τ_T was against the direction of δ_T. The heights of the contours in these figures corresponded to the distributions of τ_T and δ_T. Before the rapid decrease in P, τ_T acted on both interlayers in the region between the fixed end and the loading point, and δ_T was less than δ_{Tm} = 0.1212 nm in the entire region. However, after the rapid decrease in P, τ_T became zero and δ_T exceeded δ_{Tm} in the larger region from the fixed end to the free end in both interlayers. In other words, the shear fracture or interlayer slip occurred in the high τ_T region at the critical load (14.1 μN) and rapidly propagated throughout the entire cantilever region. In the fracture model, once fracture occurred, the shear resistance disappeared (Fig. 3-2(b)). Consequently, the three deformable layers behaved discretely, and the stiffness of the cantilever rapidly decreased at the critical load. The same stiffness was observed for both the loading and unloading processes after the rapid decrease in P. The stiffness (slope of the P–d relationship) of the cantilever before and after the rapid decrease in P was 371 and 129 N/m, respectively. Here, the stiffness of the single deformable layer with an h (= h_n) of 0.11 μm was 44.5 N/m, which was approximately 1/3 that of the cantilever after the rapid decrease in P. Thus, the stiffness of the cantilever after the shear fracture was approximately the sum of the stiffnesses of the three layers, thus indicating that the bending stiffness of the cantilever described by the fracture model followed a linear law after the shear fracture occurred.

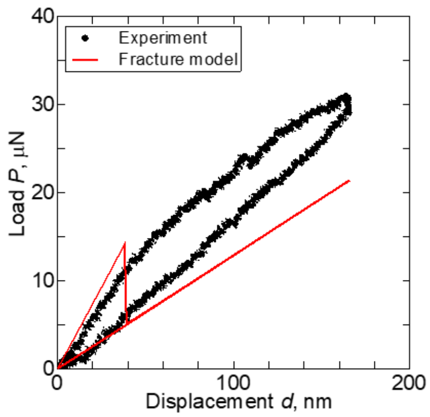

(a) P–d relationship

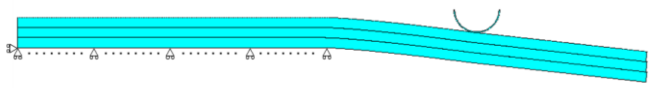

(b) Deformed shape at d_{max}

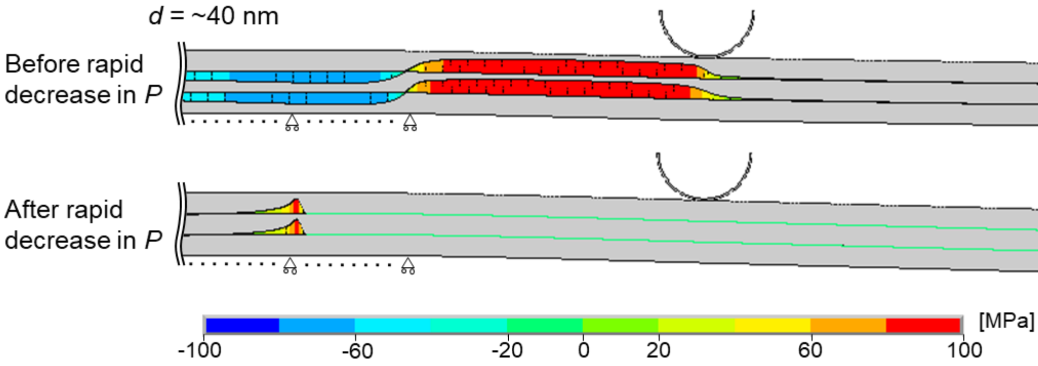

(c) Change in τ_T distribution at the P drop

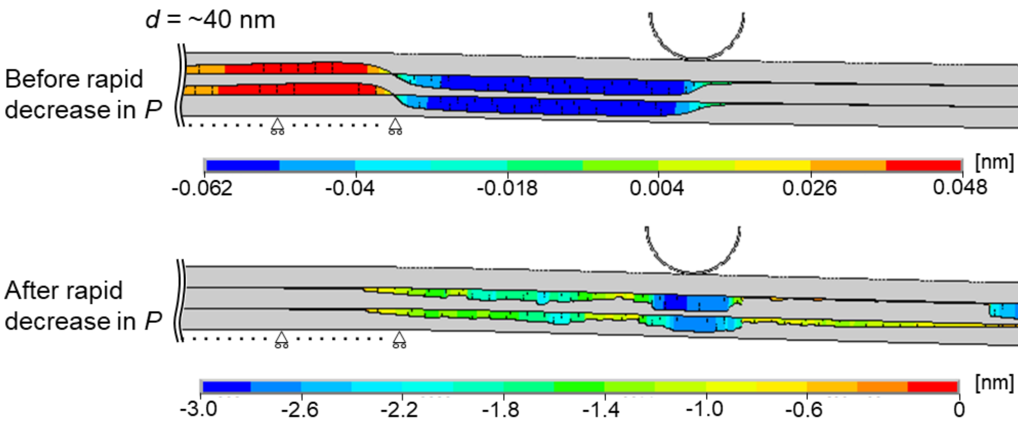

(d) Change in the δ_T distribution at the P drop

Fig. 3-4: FEM results of the HOPG cantilever: fracture model, $N = 3$, $h_n = 0.11$ μm, $\tau_{Tm} = 100$ MPa

b. Recombination model

Fig. 3-5 shows the analytical results of the semi-discrete layer model (CZM: recombination model, $N = 3$, $h_n = 11$ μm, $\tau_{Tm} = 100$ MPa). The P–d relationship (Fig. 3-5(a)) and deformed shape (Fig. 3-5(b)) obtained from the analysis were in good agreement with the experimental results (Fig. 3-1 (a)). The P–d relationship (Fig. 3-5(a)) revealed that at the initial stage of loading P increased linearly with an increase in d up to 14.1 μN at d = ~40 nm which is the same trend as that of the fracture model. At d = ~40 nm, P decreased by 2.6 μN and the magnitude of this decrease was smaller than that in the fracture model. The stiffness then gradually decreased with an increase in d until d_{max} was attained. The maximum value of P at d_{max} was larger than that in the fracture model (Fig. 3-4(a)). During the unloading process, P decreased almost linearly during the early stages of unloading, and at d = ~120 nm, the slope gradually decreased. Most of the deformation was restored by unloading; however, plastic deformation equivalent to a displacement of $d = 14$ nm remained after complete unloading. The initial stiffness of the loading process and the stiffness of the early stage of the unloading process were 371 and 373 N/m, respectively, which were almost the same. The deformed shape at $d_{max} = 166$ nm (Fig. 3-5(b)) was qualitatively similar to that of the fracture model; however, the steps at the free end by the interlayer slips were ~5 nm, which were smaller than those of the fracture model (~13 nm).

The distributions of τ_T and δ_T immediately after the rapid decrease in P are shown in Figs. 3-5(c) and 3-5(d), respectively. Before the rapid decrease in P, the τ_T and δ_T distributions were the same as those of the fracture model (Figs. 3-4(c) and (d), respectively). After the rapid decrease in P, δ_T was concentrated in the region from the fixed end to the loading point for both interlayers, and the interlayer slip (shear fracture) did not propagate to the free end of the cantilever. In this slipped region, although δ_T exceeded δ_{Tm}, recombination occurred, thus resulting in τ_T values between 0 and 100 MPa (Fig. 3-5(c)). Fig. 3-5(e) shows the τ_T distribution in the nonlinear region after the rapid decrease in P. As the deformation progressed, the interlayer slips moved toward the free end of the cantilever and δ_T increased. In this loading stage, τ_T was always present over a wide region from the fixed end to the free end. In other words, in the nonlinear region, the interlayer slips continued, whereas repeated shear fractures and recombinations occurred between the layers. Therefore, the stiffness (slope of the P–d relationship) of the cantilever gradually decreased in the nonlinear region, whereas τ_T continued to increase. In Fig. 3-5(e), there are some regions of τ_T = 0 MPa (yellow-green lines), where recombination did not occur owing to delamination (out-of-plane delamination stress). The delaminated region expanded as the loading proceeded.

Fig. 3-5(f) shows the τ_T distribution during unloading. The direction of τ_T in the region from the fixed end to the loading point was opposite to that in the loading process. In the initial unloading stage of d = 166–140 nm, a significant interlayer slip did not occur, resulting in a linear decrease in P due to the elastic deformation of the deformable layers. In the subsequent region of d = 120–0 nm, the interlayer slips in the region from the fixed end to the loading point occurred in the direction opposite to that in the loading process, resulting in nonlinearity or a decrease in stiffness. Surprisingly, even in this unloading stage, the delaminated region near the fixed end of the cantilever expanded; thus, most of the cantilever deformation could be restored by the stored elastic strain energy in each deformable layer.

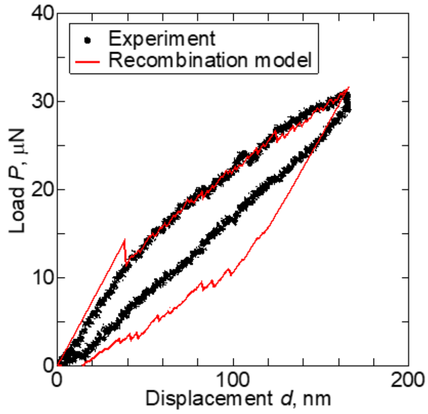

(a) P–d relationship

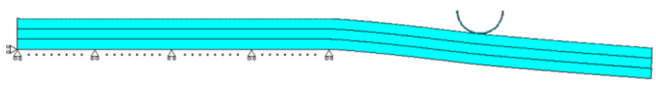

(b) Deformed shape at d_{max}

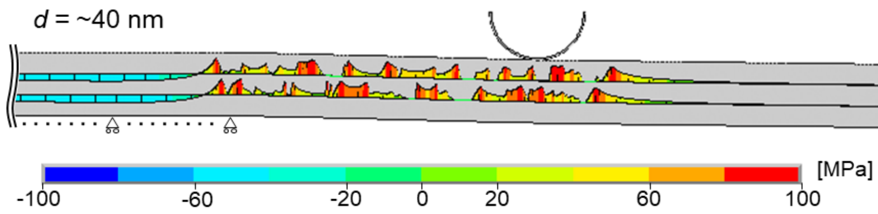

(c) τ_T distribution just after the P drop

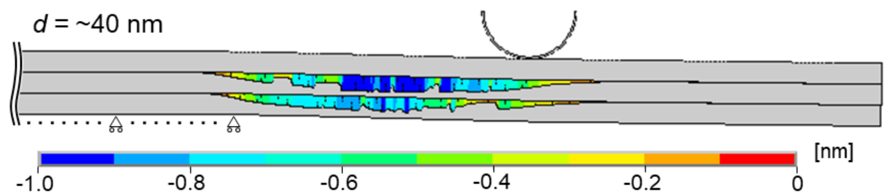

(d) δ_T distribution just after the P drop

Fig. 3-5: FEM results of the HOPG cantilever: recombination model, $N = 3$, $h_n = 0.11$ μm, $\tau_{Tm} = 100$ MPa

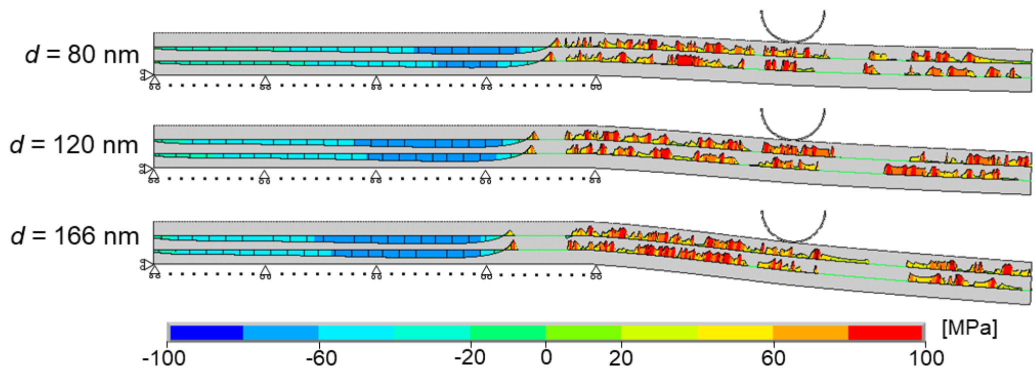

(e) τ_{T} distribution in the loading process

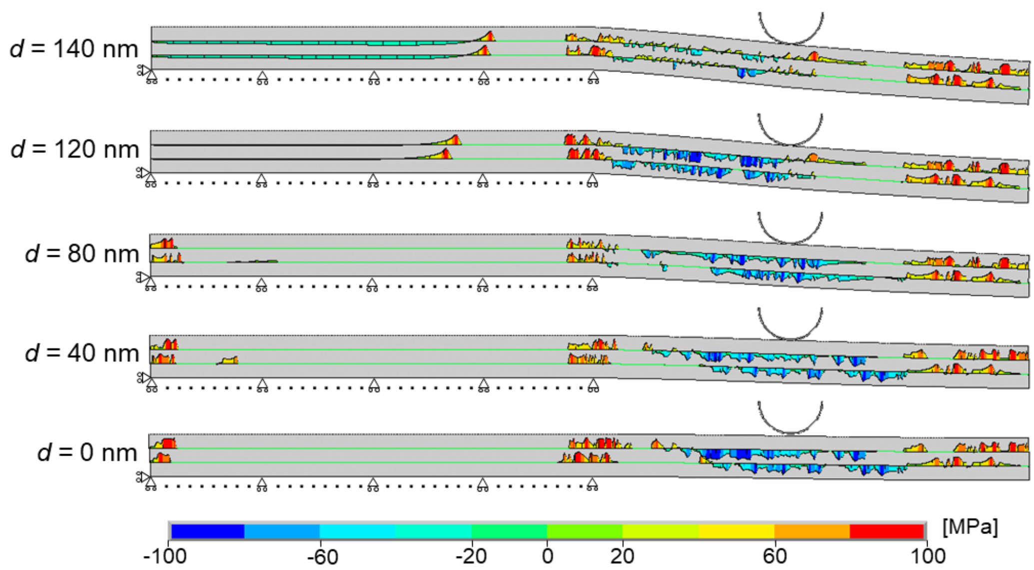

(f) τ_{T} distribution in the unloading process

Fig. 3-5: Continued.

Fig. 3-6 shows the results of two consecutive loading-unloading cycles for the same model (CZM: recombination model, $N = 3$, $h_{\mathrm{n}} = 0.11$ μm, $\tau_{\mathrm{Tm}} = 100$ MPa). In the second loading (red line in Fig. 3-6(a)), the indenter contacted the cantilever at $d = 14$ nm owing to plastic deformation caused by the first loading. After contact, P increased linearly with d and at $d = \sim 80$ nm, the P–d curve was almost the same as that of the first loading. Fig.

3-6(b) shows the τ_T distributions during the second loading process. At d = 20 nm, the τ_T distribution was similar to that after the complete unloading (d = 0 nm) of the first cycle (Fig. 3-5(f)). As deformation progressed (d = 20–80 nm), the delaminated regions shrank owing to an increase in recombination. At d = 120 nm, the τ_T distribution was approximately the same as that during the first loading process (at d = 120 nm in Fig. 3-5(e)). Hence, the subsequent loading and unloading behaviors were similar to those of the first loading and unloading cycles. The state after complete unloading in the second cycle (d = 0 nm), (Fig. 3-6(b)), was almost identical to the initial state of the second cycle (d = 20 nm). Therefore, from the third cycle onward, the same behavior as that observed in the second cycle was repeated; that is, the nonlinear deformation was reversible for cyclic loading. It is noted that as shown in Chapter 1, the experimental result in Fig. 3-6(a) is one cycle of multiple loading tests for the specimen. No sudden drop in P occurred in the second loading in the analysis. This feature was consistent with the experimental result.

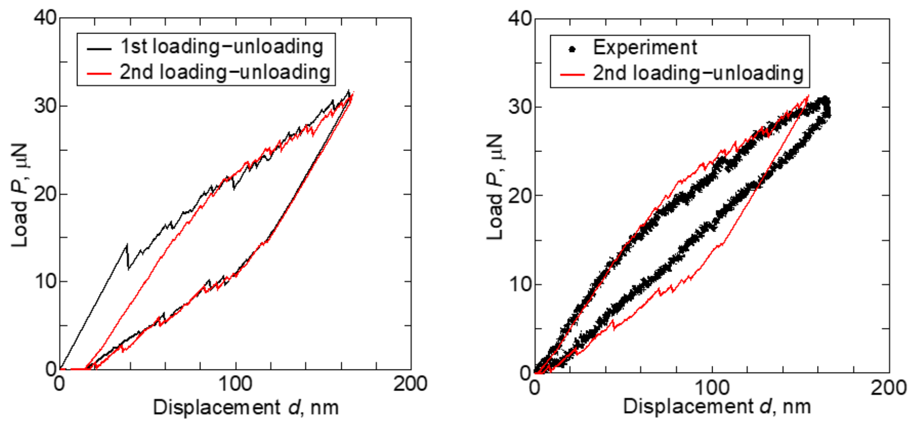

(a) Reversibility of the deformation; P–d relationship for two consecutive loading and unloading cycles (left). The second loading-unloading shows behavior more similar to the experiment (right). In the right figure, the origin of displacement is the point where the indenter contacts the cantilever again.

Fig. 3-6: FEM results of HOPG cantilever for two consecutive loading and unloading cycles: recombination model, N = 3, h_n = 0.11 μm, τ_{Tm} = 100 MPa

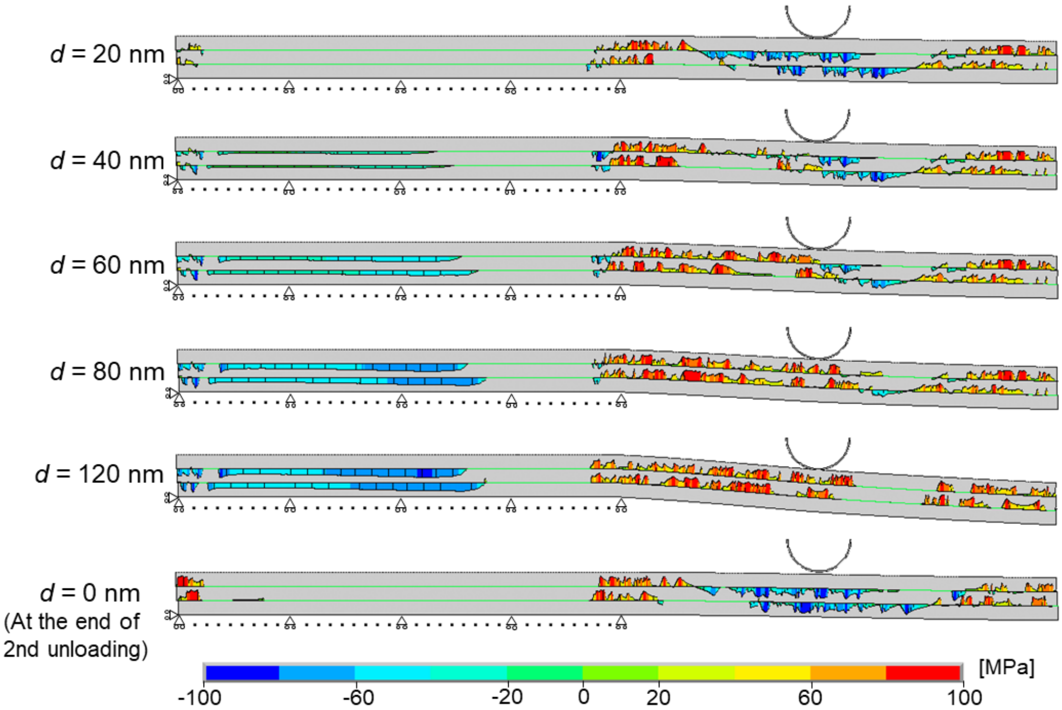

(b) Change in the distribution of τ_T in the second loading process

Fig. 3-6: Continued.

Fig. 3-7 shows the analytical results for a d_{max} of 300 nm using the same semi-discrete layer model (CZM: recombination model, $N = 3$, $h_n = 0.11$ μm, $\tau_{Tm} = 100$ MPa), together with the corresponding experimental results. The P–d relationship and deformed shape obtained by the analysis were in good agreement with those of the experimental results. Therefore, it was concluded that the model accurately reproduced the deformation characteristics of submicron HOPG cantilevers, regardless of the degree of deformation. In the semi-discrete layer model using the recombination CZM, an interlayer slip accompanied by shear fracture and recombination occurred in both the loading and unloading processes, resulting in a large nonlinear deformation and energy dissipation.

However, during the unloading process the expansion in the delaminated region of the cantilever resulted in a decrease in the resistance to the interlayer slip. Therefore, the stored elastic strain energy in each deformable layer almost completely restored the shape of the cantilever. In addition, the delaminated region shrank during the subsequent loading. This is the mechanism of the large nonlinear and reversible deformation with a hysteresis loop of vdW-layered materials. These features are in accordance with the experimental results for submicron HOPG cantilevers [1] (Figs. 3-1(a) and 3-5(a)).

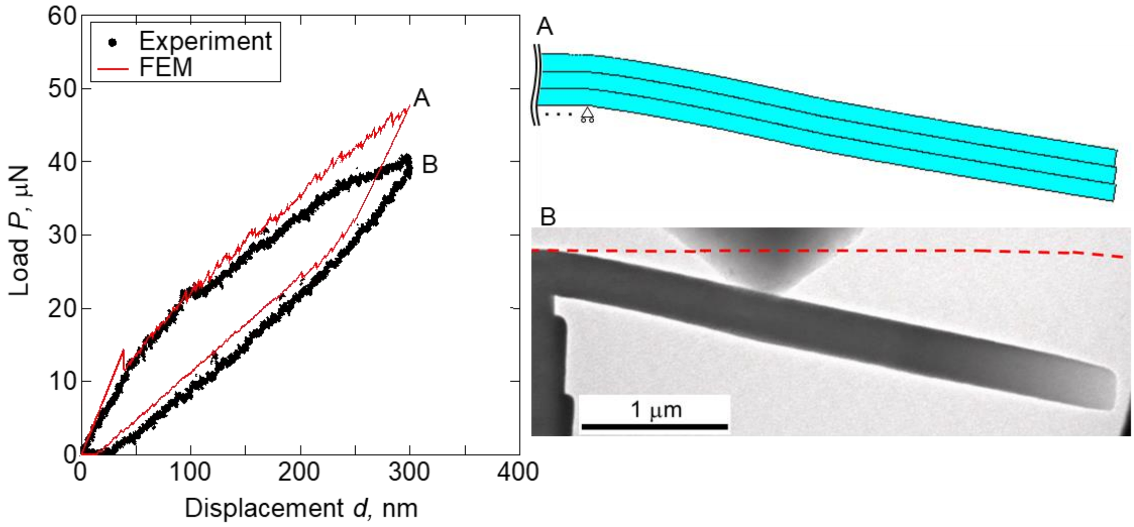

Fig. 3-7: Comparison of deformation behavior of HOPG cantilever between the recombination model ($N = 3$, $h_n = 0.11$ μm, $\tau_{Tm} = 100$ MPa) and the experiment at $d_{max} = 300$ nm

c. Effects of the interlayer interaction and deformable layer height (interlayer spacing)

Fig. 3-8(a) shows the effect of τ_{Tm} on the deformation properties. The semi-discrete layer model (CZM: recombination model, $N = 3$, $h_n = 0.11$ μm, $d_{max} = 166$ nm) was used, and

τ_{Tm} was set at 100, 300, and 589 MPa. The critical P at the rapid decrease increased almost in proportion to τ_{Tm} (14.1 μN for a τ_{Tm} = 100 MPa and 40.9 μN for a τ_{Tm} = 300 MPa). In the analysis at τ_{Tm} = 589 MPa, P did not reach the critical value; hence, an interlayer slip did not occur, thus resulting in a linear elastic deformation during both the loading and unloading processes. The deformation behaviors at τ_{Tm} of 100 and 300 MPa were qualitatively similar; however, in the unloading process, the larger the slip resistance (τ_{Tm}), the longer the linear region, and the larger the residual plastic deformation. Fig. S3-3 in the Supplementary Material 3. 4 shows the τ_T distributions during unloading. Throughout the unloading process, the delaminated region (τ_T = 0) in the analysis at τ_{Tm} = 300 MPa was smaller than that at 100 MPa (Fig. 3-5(f)). This led to a limited deformation restoration, resulting in a large plastic deformation after unloading.

Fig. 3-8(b) shows the effect of the height of the deformable layer h_n (= h/N, h = 0.33 μm) on the deformation properties. Using the semi-discrete layer model (CZM: recombination model, τ_{Tm} = 100 MPa, d_{max} = 166 nm), the cantilever height was held constant at h = 0.33 μm and h_n was set at 0.11, 0.055, and 0.030 μm for N = 3 (same as that shown in Fig.5), 6, and 11, respectively. The critical P during the rapid decrease was almost the same, regardless of h_n. The subsequent nonlinear deformation characteristics were significantly different. At h_n = 0.055 μm (N = 6) and h_n = 0.030 μm (N = 11), a region of gradual decrease in P appeared after the rapid decrease in P. Then, P began to increase, exhibiting nonlinearity with a gradually decreasing slope. As h_n decreased (N increased), the P at d_{max} and the slope of the nonlinear region decreased. The unloading behaviors were qualitatively similar, but as h_n decreased (N increased), the linear region shrank, and the plastic deformation after complete unloading increased. Fig. S3-4 in the Supplementary Material 3. 5 shows the τ_T distributions during the loading processes for

h_n of 0.055 ($N = 6$) and 0.030 μm ($N = 11$). In the region of the gradual decrease in P, a localized interlayer slip occurred in the region between the fixed end and the loading point along the neutral plane of the cantilever, and then localized interlayer slips also occurred in the upper and lower interlayers. In the subsequent P increasing region, interlayer slips progressed further, and the delaminated region expanded, particularly in the vicinity of the loading point.

Fig. 3-8(c) shows the deformed shape at d_{max} in the analyses for h_n of 0.055 and 0.030 μm. The deformed shape at h_n = 0.11 μm is shown in Fig. 3-5(b). As h_n decreased, the deformed shape changed from a straight shape bent upward at the fixed end to an S-shaped shape bent upward at the fixed end and downward at the loading point. For h_n of 0.055 and 0.030 μm, delaminated regions appeared in all interlayers near the loading point. This reduced the slip resistance near the loading point, resulting in a downward convex bending near the loading point. Since the bending stiffness decreased with a decrease in h_n, the bending curvature increased with a decreasing h_n owing to the discrete bending of each layer in the delaminated region. Therefore, as h_n decreased, the deformed shape transitioned from straight to S-shaped.

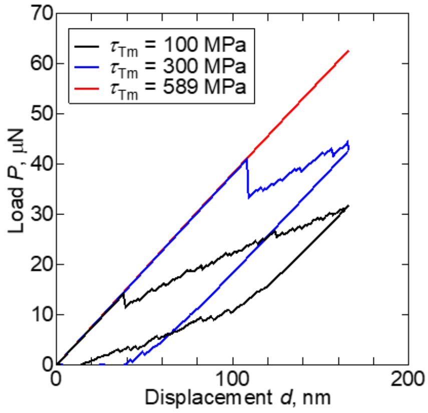

(a) Effect of τ_{Tm} on the P–d relationship (h_n = 0.11 μm, N = 3, h = 0.33 μm)

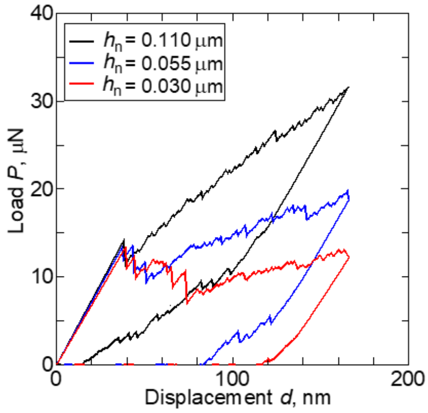

(b) Effect of h_n on the P–d relationship (τ_{Tm} = 100 MPa, h = 0.33 μm)

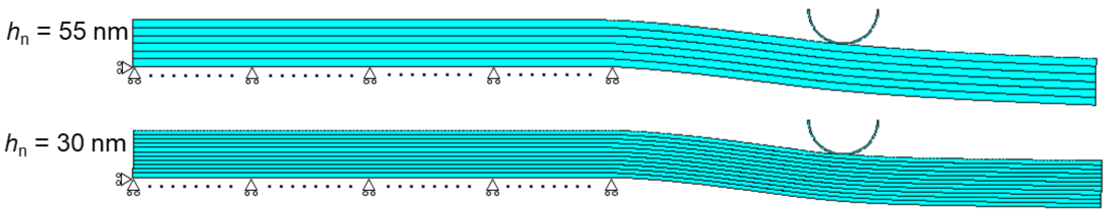

(c) Deformed shape at d_{max} (τ_{Tm} = 100 MPa, h = 0.33 μm)

Fig. 3-8: Effects of the interlayer shear strength and layer thickness on the deformation of HOPG cantilever (Recombination model)

These results indicate that the interlayer interaction and height of the deformable layers can significantly alter the deformation properties of vdW-layered materials. For example, if the interactions between layers can be engineered by intercalation [20, 21], the deformation properties of the structure can be significantly controlled. In the FIB process, which can process submicron- to microsized structures from bulk vdW-layered materials, a damaged layer in the order of 10 nm is formed on the processed surface [22–25]. The thickness of the damaged layer depends on the ion beam conditions, such as the acceleration voltage and irradiation angle [22–24]. Since the presence of such damaged layers can resist an interlayer slip, the interlayer interaction can be controlled by the processing conditions. Furthermore, the spacing of the interlayer grain boundaries [6] and the height of the layers can be changed during the manufacturing of vdW-layered materials. The mechanical model developed in this study for vdW-layered materials can predict variations in the deformation properties owing to interlayer interactions and microstructures such as grain boundaries.

3.4.2 Deformation of the $MoTe_2$ cantilever

Fig. 3-9 shows the results of a semi-discrete layer model (CZM: fracture model, $N = 10$, $h_n = 0.45$ μm, $\tau_{Tm} = 320$ MPa, $\delta_{Tm} = 40$ nm) for a micro $MoTe_2$ cantilever. The experimental *P*-*d* relationship (Fig. 3-9(a)) revealed that *P* increased almost linearly with an increase in *d*, followed by an intermittent decrease in *P*. Most of the deformation was restored by unloading. In the results of the analysis (red line), *P* increased linearly with an increase in *d* in the initial stage and then *P* continued to increase with a slightly decreasing slope. At $d = 6.8$ and 7.3 μm, two rapid decreases in *P* occurred. The unloading process was almost linear, with a slight increase in the slope with a decreasing d, and the deformation was almost completely restored. These qualitative characteristics were in agreement with the experimental results.

Fig. 3-9 (b) shows the τ_T distribution at a d_{max} = 8.58 μm. During the early loading stage, a localized interlayer slip occurred in the stress-concentration region at the bottom of the fixed end and propagated to the right. Subsequently, a new localized slip occurred along the neutral plane of the cantilever in the support region on the right side of the fixed end where the first load drop occurred. Subsequently, another localized interlayer slip occurred in the region below the neutral axis, causing a second load drop. The regions of these localized slips induced delamination (τ_T = 0). These localized slip locations were almost identical to those of the experimentally observed traces of the discrete interlayer slip (Fig. 3-9(c)). The semi-discrete layer model reproduced the deformation characteristics of the micro $MoTe_2$ cantilever. The analysis on the $MoTe_2$ cantilever using a recombination model was conducted. The result is shown in Supplementary Material S3.6. Although qualitatively similar behavior was reproduced, the fracture model was quantitatively closer to the experiment.

The qualitative behaviors of the deformation properties of the submicron HOPG and micro $MoTe_2$ cantilevers differed due to their different dimensions and materials (Figs. 3-1(a) and (b)). The semi-discrete layer model can effectively reproduce these deformation characteristics by appropriately setting the material parameters. In other words, the model can be universally applied to reproduce the bending deformation characteristics of a variety of vdW-layered materials.

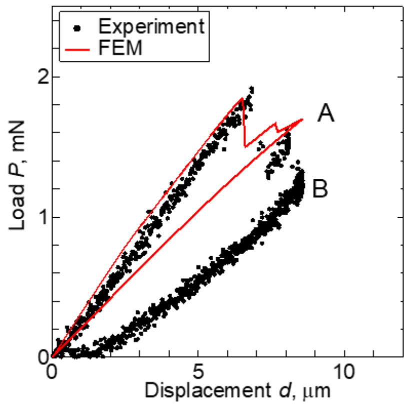

(a) P–d relationship

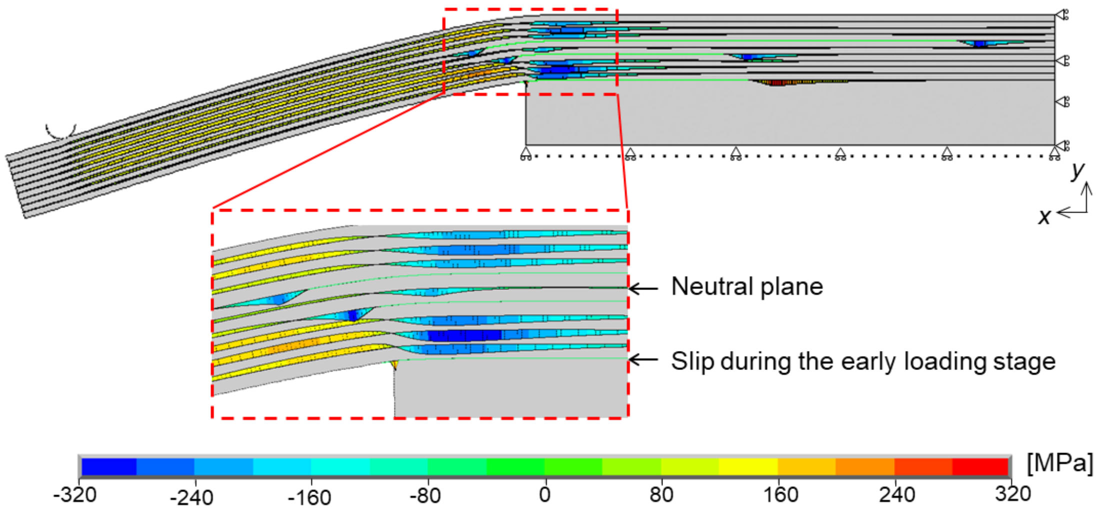

(b) Distribution of τ_T

Fig. 3-9: Comparison of the deformation behavior of $MoTe_2$ cantilever between the fracture model ($N = 10$, $h_n = 0.45$ μm, $\tau_{Tm} = 320$ MPa, $\delta_{Tm} = 40$ nm) and the experiment at $d_{max} = 8.58$ μm

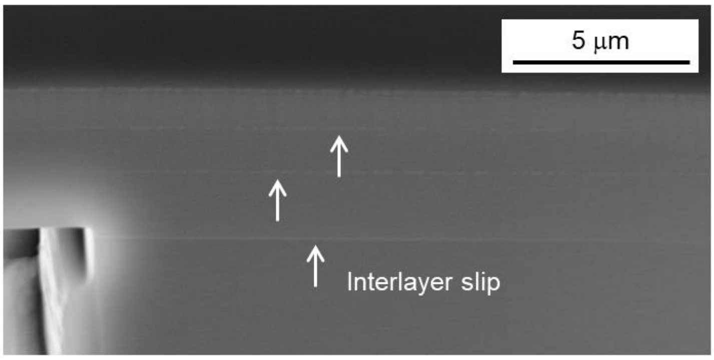

(c) SEM micrograph around the fixed end after the test. White lines indicated by the arrows are traces of the discrete interlayer slip.

Fig. 3-9: Continued.

3.4.3 Pure bending of HOPG

Using the semi-discrete layer model (CZM: recombination model, $h_n = 0.1$ μm, $\tau_{Tm} = 100$ MPa), which reproduced well the experimental behavior (Section 3.4.1), the deformation properties under pure bending and the specimen size effects were analyzed. The height of the deformable layer h_n was held constant, and the height and half-length of the specimen, h and L, were similarly changed as the number of layers N increased, i.e., $h = N\,h_n$ and $L = 25\,h = 25\,N\,h_n$ with respect to N, respectively. Fig. 3-10(a) shows the relationship between the curvature $\kappa = 1/\rho$ and M_z. Regardless of N, the loading process exhibited non-linearity, in which M_z increased linearly with an increase in κ and then the slope decreased. As in the case of the cantilever, the nonlinearity was due to the occurrence and propagation of the interlayer slips. In the unloading process, M_z decreased linearly as κ decreased, and had a slope similar to that of the initial stiffness in the loading process.

Fig. 3-10(b) shows the deformed shape for $\rho = 6L = 150h$ (normalized curvature $\kappa h =$

1/150 $\approx$ 0.00667). The overall deformation shapes were similar. Figs. 3-10(c)–(e) show the τ_T distributions. At $N = 3$ (Fig. 3-10(c)), interlayer slips occurred and propagated in both interlayers. The interlayer slip started from the free end of the plate and propagated toward the center. At $N = 5$ (Fig. 3-10(d)) and $\kappa = 0.00589$ μm^{-1}, interlayer slips occurred in the two interlayers above and below the neutral plane (second and third interlayers from the bottom). Subsequently, as κ increased, the interlayer slip occurred in the first layer from the bottom ($\kappa = 0.00890$ μm^{-1}), followed by an interlayer slip in the fourth layer from the bottom. At $N = 7$ (Fig. 3-10(e)), the interlayer slips occurred in the two interlayers above and below the neutral plane (third and fourth interlayers from the bottom), followed by interlayer slips in the outer layers (second and fifth interlayers from the bottom). Even at the maximum curvature of $\kappa h = 0.00667$ ($\kappa = 0.00953$ μm^{-1}), no interlayer slip occurred in the outermost layers (the first and sixth interlayers from the bottom). That is, as the deformation progressed, interlayer slips occurred in the interlayer closest to the neutral axis from the free end, and then these slips occurred sequentially in the outer interlayers.

Fig. 3-10(f) shows the relationship between κh and the normalized bending stiffness D/h^3 during the loading process. κ was normalized by multiplying it by h, and D was normalized by dividing it by h^3. Although the κh–D/h^3 relationships were discontinuous because the analysis was divided into four regions, the overall behavior was almost the same even when the entire region was analyzed without unloading. When κh was small, D/h^3 remained the same, regardless of N. This value was close to the solution for continuum linear elastic body (dotted line in the figure), thus indicating that in the linear region before the interlayer slip occurred, D was proportional to the cube of height h, or obeyed the classical bending theory of a continuum linear elastic body (cube law). As κh increased, D/h^3 began to deviate from the continuum solution to the lower-stiffness side, and the amount of deviation increased as the deformation progressed. This can be attributed to the decrease in stiffness in the nonlinear region owing to the interlayer slips. In a κh range of 0.002–0.003, the κh–D/h^3 relationships were almost similar regardless of N, thus indicating that the cube law was still valid in the small κh regions, although interlayer slips occurred. This is because interlayer slips occurred only in the two interlayers closest to the neutral axis, regardless of N (Figs. 3-10(c)–(e)), although the number of potential interlayer slip sites increased with an increasing N. In the κh range of 0.003–0.00667, the κh–D/h^3 relationships for $N = 5$ and $N = 7$ deviated to the lower-stiffness side compared with that for $N = 3$. The number of interlayers in which the interlayer slip occurred increased from two to four for $N = 5$ and 7, respectively, whereas only two interlayers slipped for $N = 3$. This resulted in a greater reduction in the normalized bending stiffness for $N = 5$ and 7. A further decrease in D/h^3 is expected for larger dimensions.

The bending stiffness of the vdW-layered materials described by the semi-discrete layer model deviated from the continuum theory to the lower-stiffness side owing to interlayer slips in the nonlinear deformation region. As the specimen sizes increased, the deviation from the continuum solution increased. This is because the number of potential interlayer slip locations increased with increasing specimen size. In other words, semi-discrete layer structures, or vdW-layered materials, exhibit different bending deformation properties and specimen size effects than continuum.

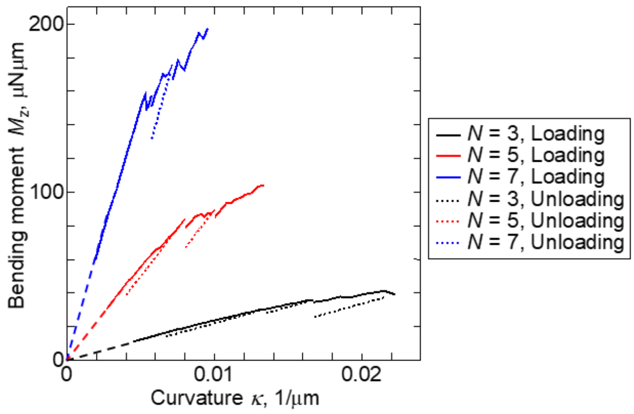

(a) Relationship between M_z and κ

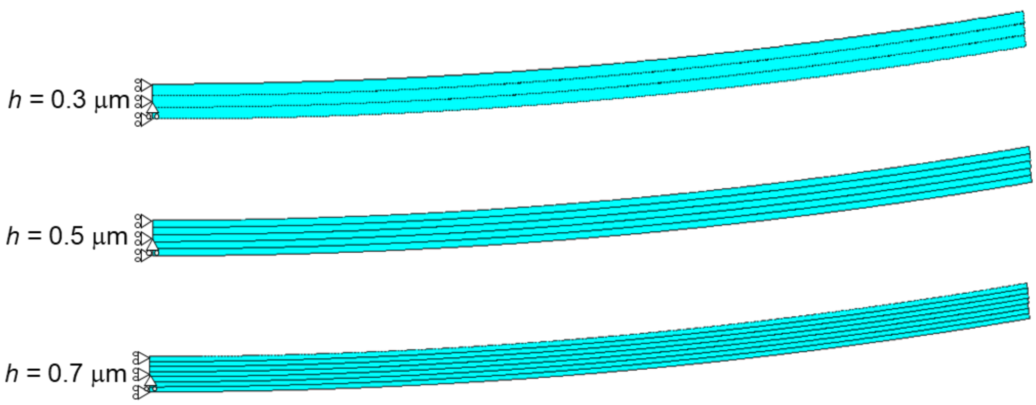

(b) Deformed shape at $\kappa h = 1/150 \approx 0.00667$

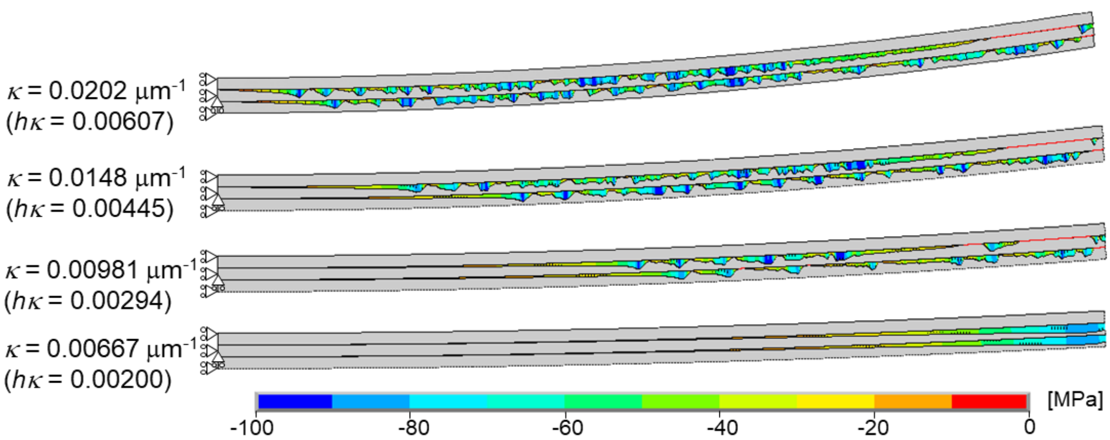

(c) τ_T and deformed shape: $N = 3$

Fig. 3-10: Pure bending properties and size effects of the HOPG cantilever

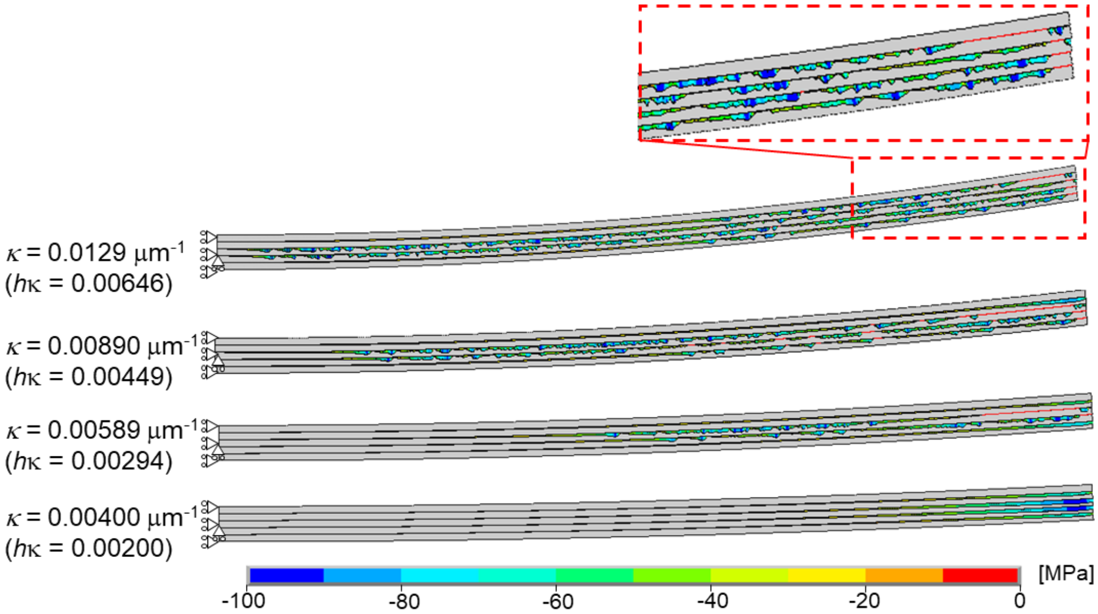

(d) τ_T and deformed shape: $N = 5$

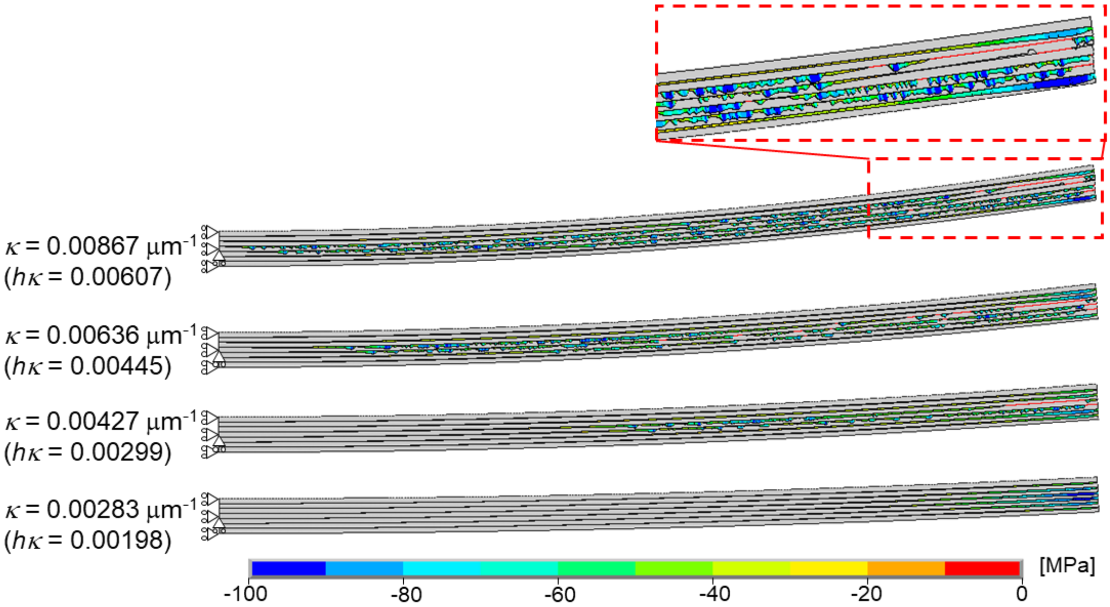

(e) τ_T and deformed shape: $N = 7$

Fig. 3-10: Continued.

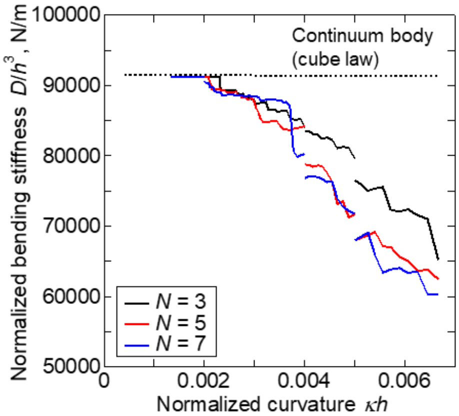

(f) Size effect on the relationship between D/h^3 and κh

Fig. 3-10: Continued.

3.4.4 Strengths and limitations of the semi-discrete layer model

MD simulation [7–9, 11] is an effective method for analyzing bending deformation of Vdw-layered materials. In principle, bending deformation of vdW-layered materials can be reproduced by MD using an appropriate potential. However, performing MD analysis on submicron- to micron-sized structures with hundreds to thousands of layers is extremely impractical in terms of computational cost. For this reason, theoretical models [7–14] based on the Euler-Bernoulli beam theory have been proposed. The simplest model is the Timoshenko beam model (TBM) [26], which takes into account the deflection of beam caused by both bending moment and shear force. Furthermore, a modified Timoshenko beam model [12] considering the bending stiffness of each layer and models [9, 13, 14] taking into account the failure of the planar-section hypothesis due to interlayer slip have been proposed. Huang et al. [14] proposed a centerline-based stacked model, which takes into account expansion and contraction, bending of each layer, and interlayer shear stiffness. On the other hand, these theoretical models can only provide solutions for simple shapes and boundary conditions, such as the bending of a beam. FEM analysis is used to analyze deformation characteristics for arbitrary shapes and boundary conditions.

We compared and examined whether these representative models could predict the experimental results of submicron HOPG. The models selected were TBM, Huang's model [14], anisotropic linear elastic body FEM [1], and the present research model (the semi-discrete layer model). TBM and Huang's model assumed three-point bending, and the FEM used a model that reproduced the shape of the cantilever specimen. To compare the models, the effective bending stiffness D_{eff} was used. The evaluation formula of D_{eff} and material constants used for each model are shown in Supplementary Material S3.7. Table 3-1 shows the obtained D_{eff}s with the experimental results. The order of all D_{eff}s agreed with the experiment, and it was found that they are effective in predicting the initial bending stiffness in small deformations.

However, in the bending deformation of submicron to micron scale vdW-layered materials, when the deformation becomes large, the occurrence and propagation of localized interlayer slips play an important role. Therefore, in Sections 3. 4. 1 and 3. 4. 2, the evaluation index of the model is to reproduce the characteristics of the load-displacement relationship of the cantilever specimen. We focused on being able to reproduce not only the initial stiffness, but also the nonlinear deformation characteristics and the hysteresis loop that is a characteristic of the loading-unloading curve. The above theoretical models and the anisotropic linear elastic FEM analysis cannot reproduce these behaviors. Although it is possible to reproduce experimental results using a continuum model by constructing a nonlinear constitutive equation, it is not possible to analyze the occurrence and propagation behavior of localized interlayer slips. On the other hand, the semi-discrete layer model developed in this study can analyze bending deformation of arbitrary structures and reproduce deformation behavior based on microscopic mechanisms such as localized interlayer slip.

Table 3-1 Comparison of effective bending stiffness among theoretical and numerical models

		Experiment	SDLM [a]	FEM (Ref. [1])	TBM (Ref. [26])	CSM (Ref. [14])
Specimen 1 h = 327 nm, b = 1.1 μm	D_{eff}, $\times 10^{-10}$ Nm	3.11	3.66	3.51	3.66	4.66
	Error %	-	17.7	12.9	17.7	49.8
Specimen 6 h = 396 nm, b = 1.2 μm	D_{eff}, $\times 10^{-10}$ Nm	4.62	5.55	4.67	4.82	6.25
	Error %	-	20.1	1.1	4.3	35.3
Specimen 8 h = 400 nm, b = 2.2 μm	D_{eff}, $\times 10^{-10}$ Nm	4.22	5.41	4.9	5.07	6.56
	Error %	-	28.2	16.1	20.1	55.5

[a] This study

3.5 Conclusions

A mechanical model that reproduces the characteristic nonlinear and reversible deformation of vdW-layered materials by considering microscopic mechanisms (discrete interlayer slips) was developed. The vdW-layered material was modeled as a stack of interacting discrete deformable layers (semi-discrete layer model), and the interlayer interaction was modeled using a CZM that reproduced the localized interlayer slip. A bending deformation analysis was performed on the HOPG and $MoTe_2$ cantilevers, and the validity of the model was verified by comparing it with experimental results.

The analysis using a semi-discrete layer model with a recombination CZM accurately reproduced the *P*–*d* relationship and the deformed shape of the experiments for submicron HOPG cantilevers, or the large nonlinear and reversible deformation with a hysteresis loop. In the analyses of submicron HOPG cantilevers, the interlayer slip accompanied by a shear fracture and recombination occurred in both the loading and unloading processes, thus resulting in a large nonlinear deformation and energy dissipation. The model considered delamination, where no recombination occurred owing to the out-of-plane delamination stress. The delaminated region expanded as loading proceeded. Surprisingly, even in the unloading stage, the delaminated region of the cantilever expanded and the resistance to an interlayer slip decreased. Therefore, the stored elastic strain energy in each deformable layer almost completely restored the shape of the cantilever upon unloading. In addition, the delaminated region shrank during subsequent loading. The nonlinear deformation was reversible for cyclic loading. Furthermore, the analyses revealed that the interlayer interaction and height of the deformable layers can significantly alter the deformation properties of vdW-layered materials.

Bending analysis using a semi-discrete layer model with a fracture CZM reproduced well the characteristics of bending experiments for micro $MoTe_2$ cantilevers, or the intermittent decreases in stiffness during the loading process and deformation restoration during the unloading process. The semi-discrete layer model developed in this study is universally applicable for reproducing the bending deformation characteristics of various vdW-layered materials by appropriately setting the material parameters.

The deformation properties of the HOPG plates under pure bending and the size effects were analyzed using a semi-discrete layer model with a recombination CZM, which reproduced the experimental behavior well. In the small-deformation region, the bending stiffness was proportional to the cube of the height or obeyed the classical continuum theory. As deformation progressed, the bending stiffness started deviating from the continuum solution to the lower-stiffness side, and the amount of deviation increased because of the interlayer slip. As the dimensions increased, the deviation from the continuum solution increased which can be attributed to the increase in the number of potential interlayer slip locations with an increase in dimensions. In other words, semi-discrete layer structures, or vdW-layered materials, exhibited different bending deformation properties and dimensional effects than the continuum body.

This model has room for improvement in two areas. The first point is the implementation of the coupled effect of the out-of-plane and in-plane interactions. The delamination distance in the out-of-plane direction affects the in-plane interaction [27]. Therefore, the reproducibility of the model could be improved by incorporating the combined effect of the in-plane and out-of-plane interactions. The second point is to provide guidelines for determining the material constants (h_n, τ_{Tm} and δ_{Tm}) for the CZM. In this study, the fracture and recombination models were selected, and material constants were determined by a trial-and-error method to reproduce the load-displacement relationships in bending tests. It is necessary to further consider guidelines for determining material constants to universally reproduce deformation characteristics regardless of material, geometry, or loading.

In this study, the height dependence of bending stiffness, the size effect in pure bending, and the breakdown of continuum theory due to increased displacement were confirmed for HOPG. However, for materials with different properties, the size dependence of the bending stiffness and the conditions under which the continuum theory breaks down remain to be clarified. Further, the deformation characteristics were clarified for out-of-plane loads on cantilever beams, but the deformation characteristics for arbitrary shapes and arbitrary loads remain to be clarified. We believe that the experimental methods and mechanical models developed in this study can be developed to elucidate them. In terms of fracture, we were also able to confirm high toughness due to the disappearance of the singular stress field. However, a universal mechanical law corresponding to the stress intensity factor has not yet been clarified. Furthermore, the fatigue fracture and creep fracture laws, which are necessary for implementing vdW-layered materials in society, have not yet been clarified. It will be possible to study them by developing the experimental methods and mechanical models developed in this study.

References

[1] M. Akiyoshi, S. Koike, T. Shimada, and H. Hirakata, Bending deformation and self-restoration of submicron-sized graphite cantilevers, *Acta Mater*. **241**, 118381 (2022).

[2] P. Wang, K. F. Wang, B. L. Wang, L. Xi, K. Sano, T. Shimada, H. Hirakata, and D. N. Fang, Interlaminar fracture toughness measurement of multilayered 2D thermoelectric materials Bi_2Te_3 by a tapered cantilever bending experiment, *Exp*. *Mech*. **62**, 165 (2022).

[3] H. Hirakata, M. Akiyoshi, R. Masuda, and T. Shimada, High fracture toughness in van der Waals-layered $MoTe_2$: Disappearance of stress singularity, *Eng*. *Fract*. *Mech*. **277**, 108974 (2023).

[4] Z. Liu, S. M. Zhang, J. R. Yang, J. Z. Liu, Y. L. Yang, and Q. S. Zheng, Interlayer shear strength of single crystalline graphite, *Acta Mech*. *Sin*. **28**, 978 (2012).

[5] Z. Liu, J. R. Yang, F. Grey, J. Z. Liu, Y. L. Liu, Y. B. Wang, Y. L. Yang, Y. Cheng, and Q. S. Zheng, Observation of microscale superlubricity in graphite, *Phys*. *Rev*. *Lett*. **108**, 205503 (2012).

[6] S. Park, H. C. Floresca, Y. Suh, and M. J. Kim, Electron microscopy analyses of natural and highly oriented pyrolytic graphites and the mechanically exfoliated graphenes produced from them, *Carbon* **48**, 797 (2010).

[7] Y. K. Shen and H. A. Wu, Interlayer shear effect on multilayer graphene subjected to bending, *Appl*. *Phys*. *Lett*. **100**, 101909 (2012).

[8] Y. L. Liu, Z. P. Xu, and Q. S. Zheng, The interlayer shear effect on graphene multilayer resonators, *J*. *Mech*. *Phys*. *Solids* **59**, 1613 (2011).

[9] F. Pan, G. R. Wang, L. Q. Liu, Y. L. Chen, Z. Zhang, and X. H. Shi, Bending induced interlayer shearing, rippling and kink buckling of multilayered graphene sheets, *J*.

Mech. *Phys*. *Solids* **122**, 340 (2019).

[10] X. M. Chen, C. L. Yi, and C. H. Ke, Bending stiffness and interlayer shear modulus of few-layer graphene, *Appl*. *Phys*. *Lett*. **106**, 101907 (2015).

[11] R. Nazemnezhad, Nonlocal Timoshenko beam model for considering shear effect of van der Waals interactions on free vibration of multilayer graphene nanoribbons, *Compos*. *Struct*. **133**, 522 (2015).

[12] H. S. Qin, Y. B. Yan, H. C. Liu, J. R. Liu, Y. W. Zhang, and Y. L. Liu, Modified Timoshenko beam model for bending behaviors of layered materials and structures, *Extreme Mech*. *Lett*. **39**, 100799 (2020).

[13] X. J. Ma, L. Q. Liu, Z. Zhang, and Y. G. Wei, Bending stiffness of circular multilayer van der Waals material sheets, *J. Appl*. *Mech*. **89**, 031011 (2022).

[14] Z. C. Huang, Z. Z. He, Y. B. Zhu, and H. A. Wu, A general theory for the bending of multilayer van der Waals materials, *J. Mech*. *Phys*. *Solids* **171**, 105144 (2023).

[15] G. Alfano and M. A. Crisfield, Finite element interface models for the delamination analysis of laminated composites: mechanical and computational issues, *Int*. *J. Numer*. *Methods Eng*. **50**, 1701 (2001).

[16] A. Bosak, M. Krisch, M. Mohr, J. Maultzsch, and C. Thomsen, Elasticity of single-crystalline graphite: Inelastic x-ray scattering study, *Phys*. *Rev*. *B* **75**, 153408 (2007).

[17] C. M. O. Bastos, R. Besse, J. L. F. Da Silva, and G. M. Sipahi, Ab initio investigation of structural stability and exfoliation energies in transition metal dichalcogenides based on Ti-, V-, and Mo-group elements, *Phys*. *Rev*. *Mater*. **3**, 044002 (2019).

[18] G. Levita, E. Molinari, T. Polcar, and M. C. Righi, First-principles comparative study on the interlayer adhesion and shear strength of transition-metal dichalcogenides and graphene, *Phys*. *Rev*. *B* **92**, 085434 (2015).

[19] Y. Wang, J. Xiao, H. Y. Zhu, Y. Li, Y. Alsaid, K. Y. Fong, Y. Zhou, S. Q. Wang, W. Shi, Y. Wang, A. Zettl, E. J. Reed, and X. Zhang, Structural phase transition in monolayer MoTe2 driven by electrostatic doping, *Nature* **550**, 487 (2017).

[20] L. Daukiya, M. N. Nair, M. Cranney, F. Vonau, S. Hajjar-Garreau, D. Aubel, and L. Simon, Functionalization of 2D materials by intercalation, *Prog. Surf. Sci.* **94**, 1 (2019).

[21] K. M. Ji, J. H. Han, A. Hirata, T. Fujita, Y. Shen, S. C. Ning, P. Liu, H. Kashani, Y. Tian, Y. Ito, J. Fujita, and Y. Oyama, Lithium intercalation into bilayer graphene, *Nat. Commun.* **10**, 275 (2019).

[22] T. Ishitani, K. Umemura, T. Ohnishi, T. Yaguchi, and T. Kamino, Improvements in performance of focused ion beam cross-sectioning: aspects of ion-sample interaction, *J. Electron Microsc.* **53**, 443 (2004).

[23] S. Rubanov and P. R. Munroe, Damage in III–V compounds during focused ion beam milling, *Microsc. Microanal.* **11**, 446 (2005).

[24] D. Kiener, C. Motz, M. Rester, M. Jenko, and G. Dehm, FIB damage of Cu and possible consequences for miniaturized mechanical tests, *Mater. Sci. Eng. A* **459**, 262 (2007).

[25] J. Mayer, L. A. Giannuzzi, T. Kamino, and J. Michael, TEM sample preparation and FIB-induced damage, *MRS Bull.* **32**, 400 (2007).

[26] S. P. Timoshenko, On the correction for shear of the differential equation for transverse vibrations of prismatic bars, *Philos. Mag.* **41**, 744 (1921).

[27] Y. F. Guo, W. L. Guo, and C. F. Chen, Modifying atomic-scale friction between two graphene sheets: A molecular-force-field study, *Phys. Rev. B* **76**, 155429 (2007).

Chapter 4

High fracture toughness in van der Waals-layered $MoTe_2$: Disappearance of stress singularity

4. 1 Introduction

VdW-layered materials have mechanical anisotropy owing to this structural anisotropy, which is considered to affect the strength against fracture. In particular, the discrete deformation nature revealed in Chapters 2 and 3 will affect the fracture behavior. Fracture is a phenomenon caused by a local mechanical field owing to a defect inside a material: for example, stress concentration at a notch root or a singular stress field formed at a crack tip [1]. Considering the structural anisotropy of vdW-layered materials, typical cracks are classified as in-plane cracks (Fig. 1-3(a)) or out-of-plane cracks (Fig. 1-3(b)). In in-plane cracks, stress is transmitted by a strong bond in the plane of the 2D material; therefore, they can be regarded as continuum bodies in the in-plane direction, and a singular stress field is formed at a crack tip. On the other hand, in out-of-plane cracks, the interaction between layers is weak, and the force is difficult to transmit between layers. As an extreme assumption, if there is no interaction between layers (complete discrete body), each layer behaves as an isolated element, and no force is transmitted in the out-of-plane direction; thus, stress concentration does not occur. Because vdW-layered materials comprise weakly interacting 2D material elements, it is expected that a singular stress field for out-of-plane cracks is unlikely to occur (and the stress concentration in the notch root is reduced). However, research from this perspective has not been sufficiently conducted.

The purpose of this chapter is to determine the fracture mechanisms in vdW-layered materials and experimentally demonstrate the high fracture toughness owing to the disappearance of the singular stress field. Fracture toughness tests were conducted for in-plane and out-of-plane cracks in the microscale vdW-layered material $MoTe_2$, which is a typical TMD material. By comparing the fracture toughness of in-plane and out-of-plane cracks, the high fracture toughness of the material against out-of-plane cracks was demonstrated.

4.2 Experimental method

4.2.1 In-plane crack

a. Fracture toughness test

A chevron-notched microcantilever test [2, 3] was performed to evaluate the fracture toughness of in-plane cracks. The chevron notch test was developed as a method for evaluating the fracture toughness of ceramic materials, for which it is difficult to introduce pre-cracks [4, 5]. In this method, under a monotonically increasing load, the crack generated from the chevron notch tip grows stably, leading to an unstable fracture. Because the crack growth driving force curve has a downward convex shape with a minimum value, the fracture toughness value can be determined from the critical load at an unstable fracture without measuring the crack length. The cantilever-type test is suitable for micro-sized specimens because a micromechanical testing technique of nanoindentation can be used to apply a load to the cantilever with an indenter. Furthermore, it is possible to perform *in situ* electron microscopy experiments. Fig. 4-1(a) shows a schematic of the chevron-notched microcantilever specimen used for evaluating the fracture toughness of in-plane cracks. The in-plane direction of the 2D material coincided with the *XY* plane of the cantilever, and the *Z* direction was the stacking direction of the 2D material. A chevron notch was placed at the fixed end of the cantilever beam. Fig. 4-1(b) shows a cross-sectional view of the notch in the *X* direction. The crack front length increased as the crack grew. Applying a load in the -*Y* direction near the free end of the beam generated bending stress, and a Mode I load was applied to the crack.

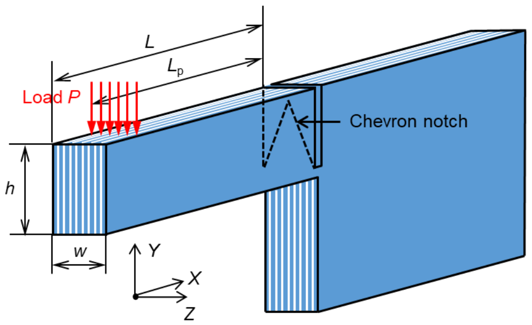

(a) Schematic of specimen and loading

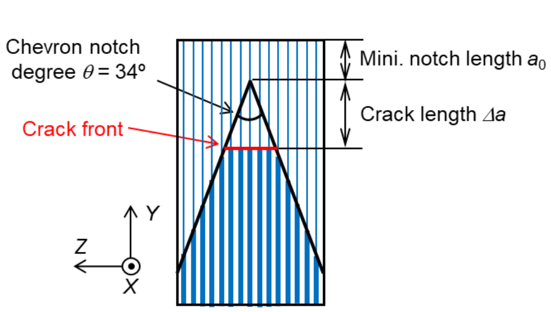

(b) Cross-section of Chevron-notch

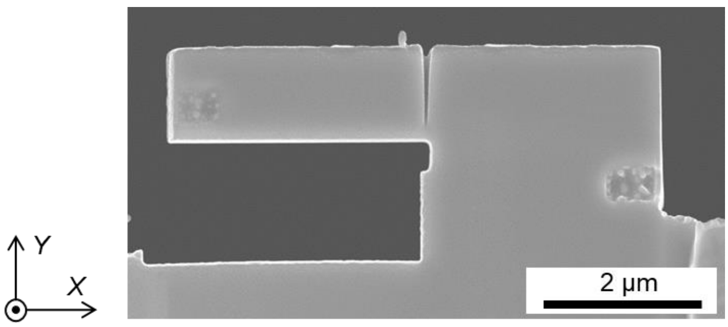

(c) SEM image of Specimen ISA

Fig. 4-1: Fracture toughness test for in-plane crack using chevron-notched microcantilever specimen

The tested material was single-crystal 2H-phase $MoTe_2$ (2D Semiconductors). The specimens were taken from a bulk $MoTe_2$ sample using a focused ion beam (FIB) processing system (Hitachi High-Tech Corp., FB2200). The details of the specimen processing procedure are provided in Supplementary Material S4.1. After creating the cantilever beam, a chevron notch with $\theta = 34$ ° was machined near the fixed end of the beam, as shown in Fig. 4-1(a) and (b). Two small specimens (ISA and ISB) and a large specimen (IL) were prepared. Table 4-1 lists the dimensions of each specimen, where L is the length, h is the height, w is the width, a_0 is the minimum notch length, Δa is the crack length, and L_P is the distance from the cantilever fixed end to the loading point. A scanning electron microscopy (SEM) image of Specimen ISA is shown in Fig. 4-1(c), and the SEM Images of Specimens ISB and IL are shown in Supplementary Material S4.2.

An electrostatic force-type micromechanical test device (Bruker Corp., PI 95 TEM PicoIndenter) was used for *in situ* transmission electron microscopy (TEM). This device consists of a transducer that controls and measures the load P and displacement d of the indenter, and a three-dimensional (3D) piezo stage for positioning. A diamond rectangular cuboid indenter (processed using FIB) was used as the indenter. The test was conducted under *in situ* observation using TEM (JEOL ltd., JEM-2100). The acceleration voltage of the electron beam was 200 kV, and the pressure in the chamber was 1.5×10^{-5} Pa. The temperature of the specimen was not controlled, and the temperature in the laboratory was set to approximately 293 K. The test was performed under displacement control at a displacement rate of 2 nm/s, and the specimen was loaded until it was completely fractured.

Table 4-1: Specimen dimensions of in-plane fracture toughness test

	Specimen ISA	Specimen ISB	Specimen IL
Hight h, μm	1.30	1.25	6.52
Width w, μm	0.74	0.60	4.02
Length L, μm	3.51	4.33	13.45
Distance between loading point and notch L_P, μm	3.35	4.26	13.02
Mimi. notch length a_0, μm	0.11	0.10	0.42

b. Stress analysis

During the in-plane crack test, the stress is transmitted in the in-plane direction through the atomic bond to generate an in-plane stress concentration and singular stress field. The vdW-layered $MoTe_2$ was treated as a continuum body (anisotropic linear elastic body), and the stress intensity factor was evaluated using finite element method (FEM) stress analysis. Commercial FEM software (Abaqus 2017) was used for the analysis. The analytical model of Specimen IL is shown in Fig. 4-2(a). A 3D model was created, and the displacement of the bottom surface of the support section of the cantilever was fixed. A uniformly distributed load equivalent to the fracture load P_C obtained in the experiment was applied at the load position on the upper surface of the cantilever beam. A hexahedral 20-node quadratic element was used in the vicinity of the notch, including the crack, and a tetrahedral 10-node quadratic element was used in the other sections. The minimum element size of the crack tip was 10 nm. The anisotropic elastic constants of $MoTe_2$ were set to C_{11} = 123 GPa, C_{12} = 28 GPa, C_{13} = 9 GPa, C_{33} = 37 GPa, C_{44} = 18 GPa, and C_{66} = 47 GPa [6]. A sharp crack was introduced in the center of the chevron notch, and the crack front was a straight line, as shown by the red line in the cross section of Fig. 4-2(a). To evaluate the minimum value of the crack growth driving force (Mode I stress intensity factor K) curve, we created multiple models with different crack lengths Δa and evaluated the K–Δa relationship.

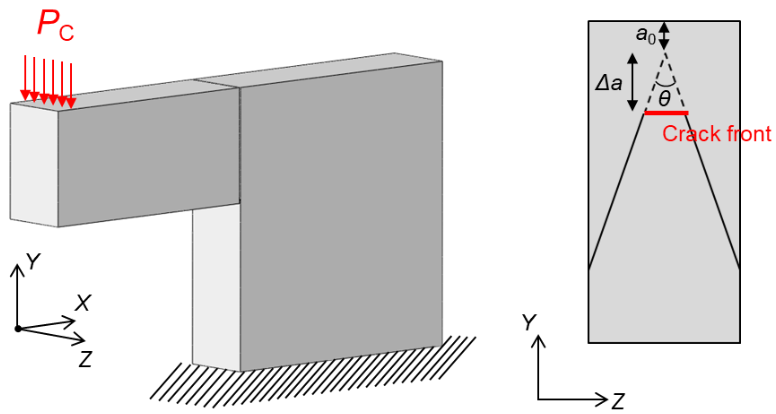

(a) In-plane crack specimen (Specimen IL)

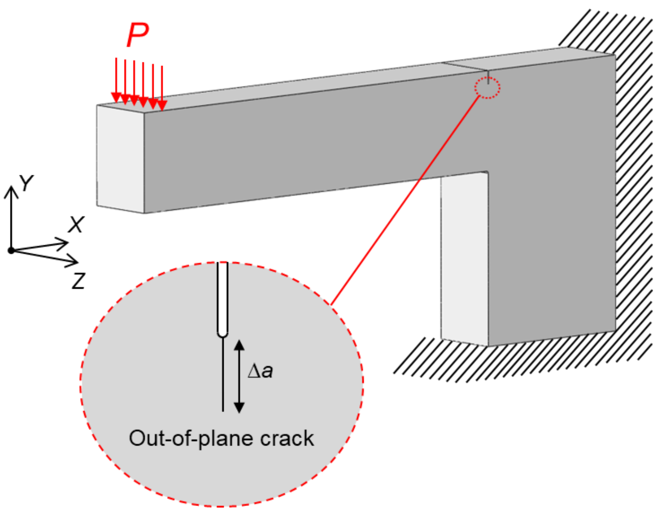

(b) Out-of-plane crack (Specimen OC)

Fig. 4-2: FEM models of in-plane and out-of-plane crack specimens (continuum model)

4.2.2 Out-of-plane crack

a. Fracture toughness test

To evaluate fracture toughness, it is necessary to introduce a sharp pre-crack that stops or extends stably. In out-of-plane cracks, high fracture toughness is expected owing to the disappearance of the singular stress field due to the structural discreteness (Fig. 1-3(b)). Therefore, a cantilever bending test with a uniform out-of-plane notch in the width direction was adopted. It is assumed that even if a crack is generated from the notch root, it can be stopped by this discreteness. Fig. 4-3(a) shows a schematic of the specimen and loading, and a magnified view around the notch is shown in Fig. 4-3(b). The specimen was a cantilever beam, and the in-plane direction of the vdW-layered $MoTe_2$ was the XZ plane. By applying a load to the position at a distance L_p from the fixed end (notch) using an indenter in the -Y direction, bending stress is applied to the notch of the cantilever beam. This was intended to generate an out-of-plane crack from the notch root and propagate in the -Y direction. In Fig. 4-3(b), $a_0 + \Delta a$ corresponds to the effective crack length.

The tested material was single-crystal 2H-phase $MoTe_2$ (2D Semiconductors). The specimens were fabricated from the bulk 2H-phase $MoTe_2$ sample using an FIB processing system (Thermo Fisher Scientific, Scios 2). The details of the specimen processing procedure are provided in Supplementary Material S4.3. Three specimens (OA, OB, and OC) with different cantilever heights were prepared; their dimensions are listed in Table 4-2. Fig. 4-3(c) shows the SEM image of Specimen OC with the largest h, and the SEM images of Specimens OA and OB are shown in Supplementary Material S4.4. The notch root had a rounded shape, and the radius of curvature of the notch root evaluated from the SEM images was larger on the FIB irradiation side (front) than on the back.

A small mechanical test device (Unisoku Co., ltd.) for *in situ* SEM was used. This device has a piezo stage for positioning (SmarAct GmbH, XYZ axis stage), a load cell for measuring the indenter load *P* (Kyowa Electronic Instruments Co., ltd., LVS-A, rated capacity ± 200 mN), and a piezo actuator (Piezomechanik GmbH, PSt 150/5/80 VS10, Max. Stroke 80 μm), which controls the displacement of the indenter *d*. A diamond spherical indenter (Bruker Corp.) with a tip radius of curvature of approximately 1 μm was used as the indenter. The test was conducted under *in situ* SEM (Thermo Fisher Scientific, Scios 2) observation with an acceleration voltage of 30 kV (Specimens OA and OB) and 20 kV (Specimen OC). The tests were performed by controlling the voltage applied to the piezo actuator, and the displacement was increased by increasing the applied voltage from 0 to 0.04 V/s; after reaching the predetermined displacement, it was pulled back at 0.04 V/s. For each specimen, multiple tests were performed, in which the maximum displacement was increased in order. Six tests (OA1–OA6) were performed on Specimen OA, four tests (OB1–OB4) were performed on Specimen OB, and three tests (OC1–OC3) were performed on Specimen OC. In each specimen, the position where the indenter came into contact with the specimen in the first test was set as the origin of the displacement of the indenter *d*.

Table 4-2: Specimen dimensions of out-of-plane fracture toughness test

	Specimen OA	Specimen OB	Specimen OC
Height h, μm	3.3	5.2	9.1
Width w, μm	6.7	8.1	6.5
Length L, μm	36.7	39.6	40.6
Distance between loading point and notch L_p, μm	34.6	35.6	38.2
Notch length a_0, μm	1.0	0.9	1.2
Radius of curvature of notch root (front), μm	0.04	0.11	0.04
Radius of curvature of notch root (back), μm	0.30	0.31	0.35

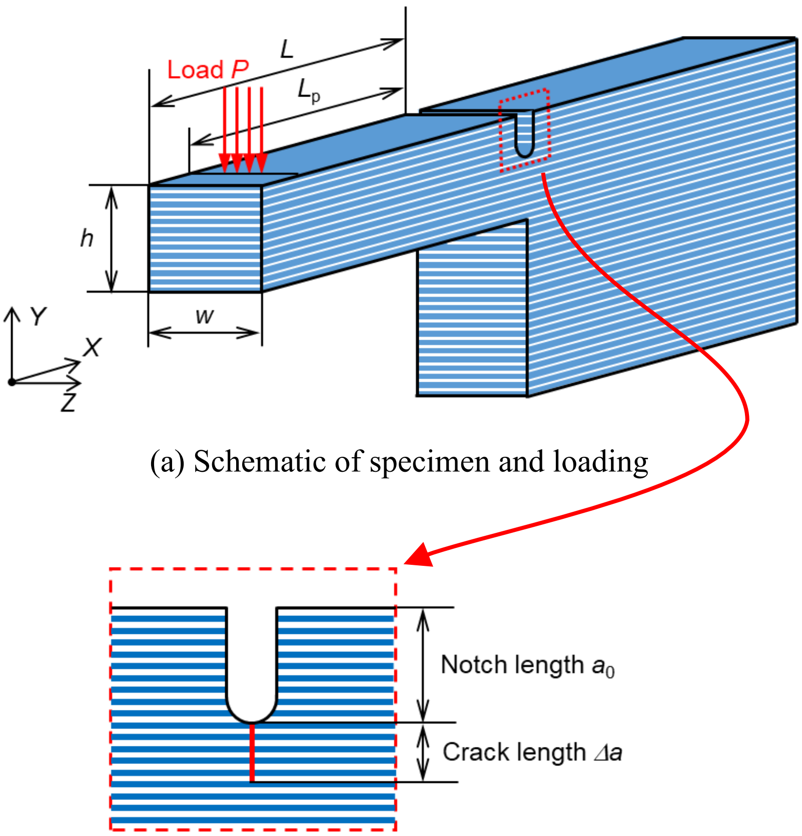

(a) Schematic of specimen and loading

(b) Magnified view of notch and crack

Fig. 4-3: Fracture toughness test for out-of-plane crack using uniform-notched microcantilever specimen

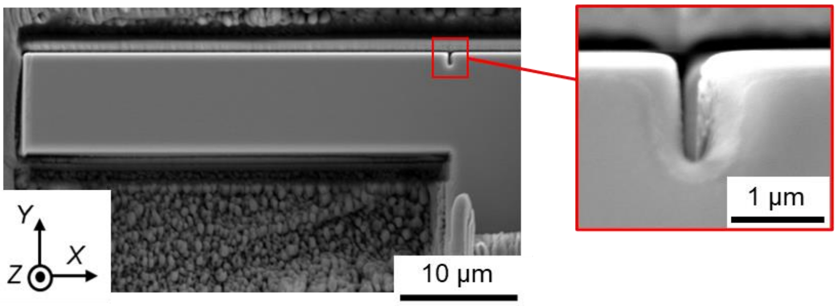

(c) SEM image of Specimen OC

Fig. 4-3: Continued.

b. Stress analysis based on continuum and discrete models

Because the vdW-layered material can be considered a discrete body for out-of-plane cracks, stress analysis based on the continuum assumption is not valid. Therefore, in addition to the stress analysis based on the continuum assumption, a deformation analysis was performed using a discrete model that considers the discrete nature of the layers. The fracture toughness evaluated based on the continuum assumption is “apparent” because it does not consider the discrete nature of the layers. Nevertheless, in this study, the “apparent” fracture toughness K_{C_O} of the out-of-plane crack was evaluated based on the continuum assumption to observe the differences in the results. The high fracture toughness owing to the discrete body was examined by comparing K_{C_O} with the fracture toughness for the in-plane crack K_{C_I}. Therefore, FEM stress analysis was performed assuming $MoTe_2$ as a continuum (anisotropic linear elastic body). The analysis model (Specimen OC) is shown in Fig. 4-2(b). A 3D model was created, and the displacements of the bottom and side surfaces of the support section of the cantilever beam were fixed. The notch shape was uniform in the width direction (Z direction), and the notch root radius of curvature was the value on the back side of the specimen (the side with the smaller radius of curvature). An out-of-plane crack was introduced at the notch root. When performing an analysis on Specimen OA that considers the interlayer delamination that occurred during the test (details will be described Section 4. 3), both out-of-plane and delamination cracks were created in the model, as shown in Fig. S4-5. A uniformly distributed load corresponding to the fracture load P_C or the maximum load P_{max} obtained in the experiment was applied to the load position on the upper surface of the cantilever beam. The other analysis methods were the same as those used for in-plane cracks.

In addition, deformation analysis was performed using the semi-discrete layer model in Chapter 3 to incorporate discrete interlayer slip. Fig. 4-4 shows the analytical model. This model consists of stacked continuum layers interacting by vdW forces. The continuum layer was treated as an anisotropic linear elastic body, the vdW interaction between layers was modeled by a CZM. The maximum value of τ_T , τ_{Tm}, and the slip distance at τ_{Tm}, $\delta_{Tm}/2$, were determined to reproduce the deformation behavior of smooth specimens (Specimens OS-I and OS-II) without notches. The material constants determined were $\tau_{Tm} = 250$ MPa and $\delta_{Tm} = 30$ nm, respectively. Details of the deformation test on smooth specimens and the method for determining material constants are shown in Supplementary materials S3.1 and 4.6. The out-of-plane interactions between the layers were modeled by a nonlinear spring with varying contact stiffness to prevent delamination and overlap. The height of the continuum layer was set to 450 nm because the localized interlayers slip occurred at an average interval of roughly 0.5 μm, as shown in Fig. S3-1(f). A critical load P_C at the onset of crack propagation was applied to the loading point for the out-of-plane crack specimen (Specimen OC, Test OC2). Assuming plane strain, a triangular 6-node quadratic element was used as the element. FEM software (ANSYS) was used for the analysis.

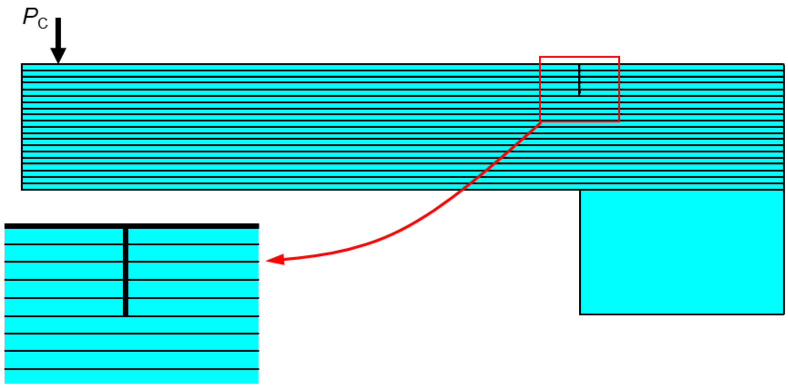

Fig. 4-4: Analytical model with out-of-plane crack in the specimen

4.3 Results and discussions

4.3.1 In-plane crack

Fig. 4-5(a) shows the load P – displacement d relationship for the Specimen ISA test. As d increased, P increased linearly and then decreased rapidly at d = 81 nm and $P = P_C$ = 27.5 μN. Fig. 4-5(b)–(d) show *in situ* TEM images of the specimen before the test, at P_C, and immediately after the load dropped. After the cantilever beam was slightly bent, as shown in Fig. 4-5(c), the crack began to propagate in the chevron notch in the -Y direction, as shown in Fig. 4-5(d), leading to fracture. Thus, P_C can be regarded as the critical load for the chevron crack propagation. The other specimens exhibited qualitatively similar behaviors. The critical loads P_C of Specimens ISB and IL were determined to be 17.7 μN and 484 μN, respectively.

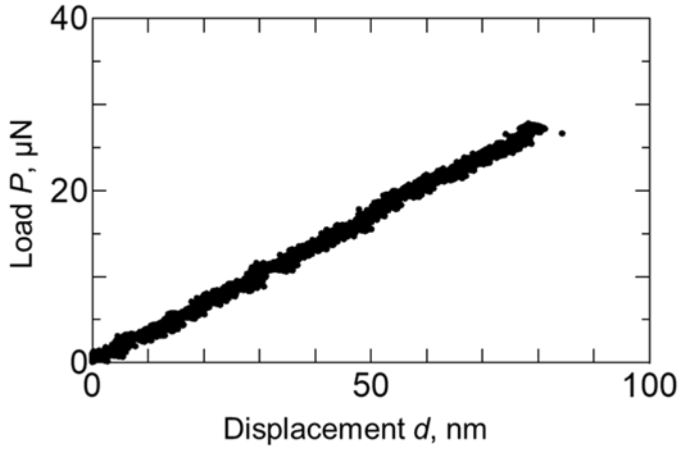

(a) Load-displacement curve

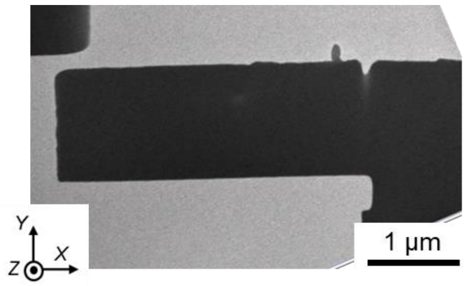

(b) Before loading

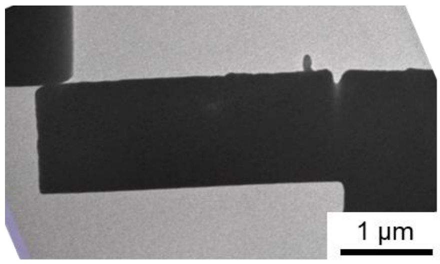

(c) At maximum load $P = P_C$

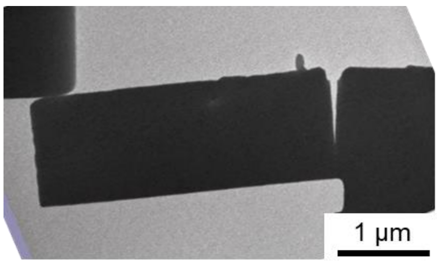

(d) In-plane crack propagation

Fig. 4-5: Experimental results of in-plane crack fracture toughness test for Specimen ISA. (b)–(d) show *in situ* TEM images in the test.

Fig. 4-6 shows the stress intensity factor K – crack length Δa relationships of the three specimens evaluated by FEM analysis. Because these graphs show the K–Δa curve at the fracture load P_C, the minimum value of K can be regarded as the fracture toughness of the in-plane crack K_{C_I}. From Fig. 4-6(a), in Specimens ISA and ISB, the minimum value of K occurred at Δa = 290 nm and Δa = 270 nm, respectively, and K_{C_I} = 1.07 MPa m$^{1/2}$ and K_{C_I} = 1.01 MPa m$^{1/2}$ were determined. From Fig. 4-6(b), in Specimen IL, K_{C_I} = 0.83 MPa m$^{1/2}$ at Δa = 1000 nm was determined. K_{C_I} of Specimen IL was approximately 20 % lower than those of Specimens ISA and ISB. The fracture toughness values are summarized in Table 4-3.

Table 4-3: Fracture toughness

In-plane crack	Fracture toughness K_{C_I}, MPa m$^{1/2}$
Specimen ISA	1.07
Specimen ISB	1.01
Specimen IL	0.83
Out-of-plane crack	Fracture toughness K_{C_O}, MPa m$^{1/2}$
Specimen OA	> 1.4
Specimen OB	> 2.1
Specimen OC	1.8

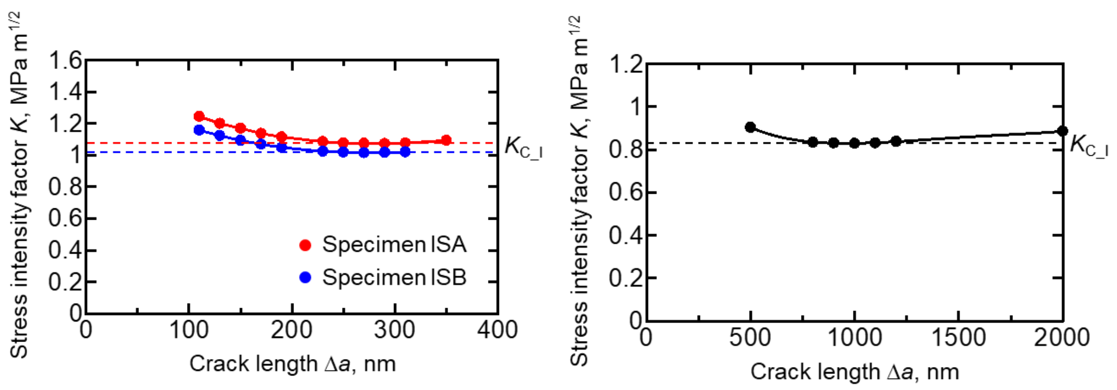

(a) Specimens ISA and ISB (b) Specimen IL

Fig. 4-6: Relationship between stress intensity factor K and crack length Δa at the critical load P_C in the in-plane crack fracture toughness tests

An FIB-induced damage layer existed on the surface of the FIB-processed specimens [7, 8], and the influence of this layer is considered one of the reasons why K_{C_I} of the large Specimen IL was lower than those of the small Specimens ISA and ISB. Fig. 4-7(a) shows the SEM image of the fracture surface of Specimen IL; the image was taken from a direction inclined by 30 ° from the Y direction and magnified twice vertically. On the fracture surface, linear striped patterns, with widths on the order of 10 nm, reflecting the layered structure, were observed. In the vicinity of the FIB-milled surface of the chevron notch, a different fracture surface morphology was confirmed with a thickness of approximately 30 nm. This region could be an FIB-damaged area. From Fig. 4-6, it is estimated that the crack growth of Specimens ISA and IL became unstable at Δa = 290 nm and Δa = 1000 nm, respectively; the crack front lengths at this time were approximately 180 nm and 610 nm, respectively. As shown in Fig. 4-7(b), the proportion of the FIB-damaged layer in the crack front increased as the specimen size decreased; the smaller the specimen size, the more the evaluated fracture toughness reflects the characteristics of the damaged layer. Therefore, the evaluated K_{C_I} of the smaller Specimens ISA and ISB could potentially be inflated. The value of the larger Specimen IL was considered to be more accurate.

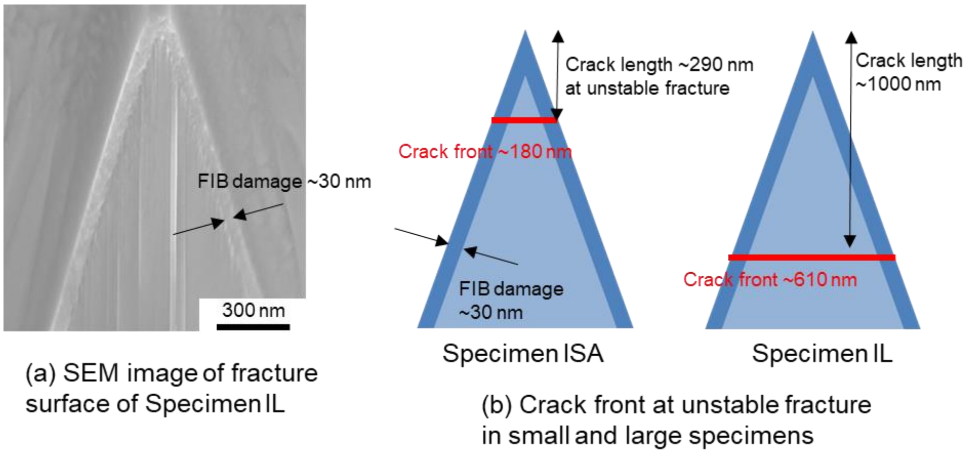

Fig. 4-7: Effect of FIB-induced damage layer on the estimation of in-plane crack fracture toughness

4.3.2 Out-of-plane crack

a. Specimen OA

Fig. 4-8(a) shows the load P vs displacement d relationship in the first test (Test OA1) with a maximum displacement of d = 6.0 μm. The black and blue marks indicate the loading and unloading curves, respectively. Fig. 4-8(b) and (c) show the SEM images during Test OA1, which correspond to Points A and B shown in Fig. 4-8(a), respectively. During loading, P increased linearly with an increase in d up to the maximum displacement. The oscillation in the P – d relationship was due to the resolution of the load cell and did not indicate the occurrence of any phenomenon accompanied by the oscillation. During this loading period, delamination occurred from the notch toward the free end of the cantilever at the section surrounded by the red dashed line in Fig. 4-8(c) and progressed to approximately 4 μm. P decreased linearly during unloading, and the bending deformation of the specimen was almost recovered. There was no evidence of out-of-plane cracking at the notch root. In Test OA1, delamination occurred starting from the notch, without the occurrence of out-of-plane cracks. Test OA2, with a maximum displacement of d = 6.8 μm, showed similar behavior to that of Test OA1.

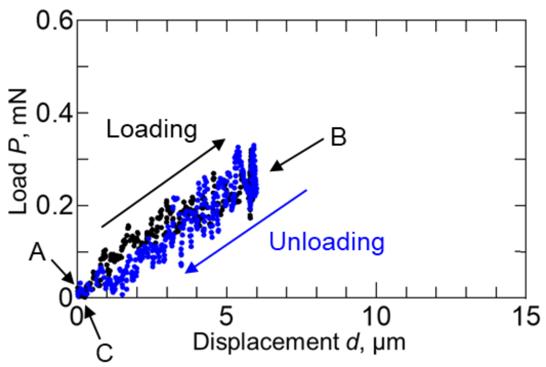

(a) Relationship between load P and displacement d in Test OA1

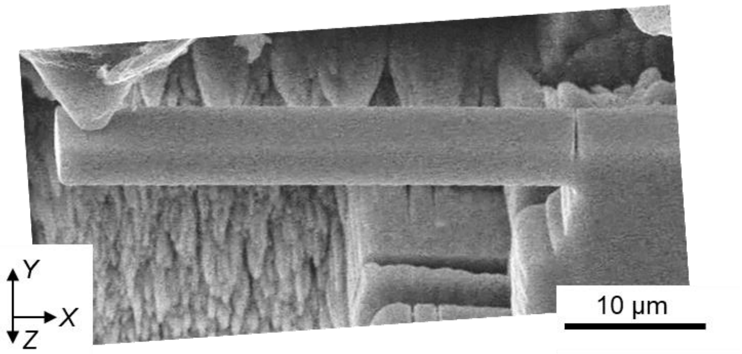

(b) Before loading (A in Fig. 4-8(a))

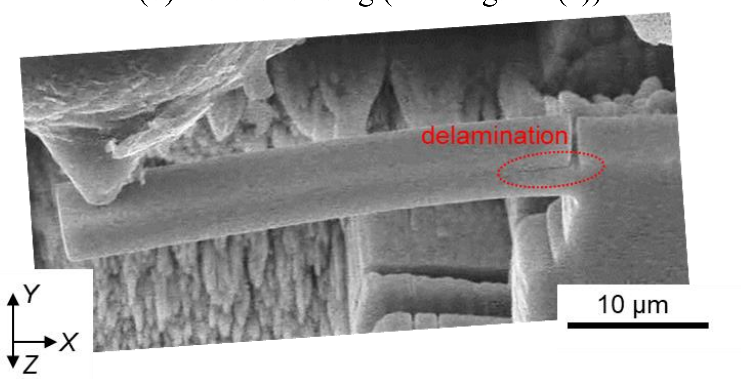

(c) At maximum displacement (B in Fig. 4-8(a))

Fig. 4-8: Experimental results of out-of-plane crack fracture toughness test in Test OA1. (b)–(d) show *in situ* SEM images in the test and (e) shows a SEM image around the notch after test.

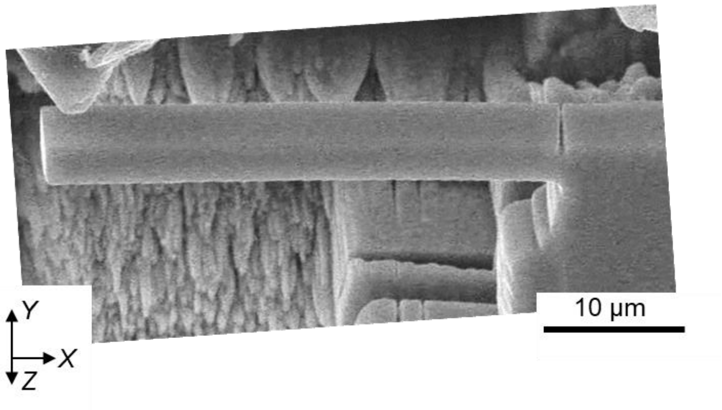

(d) After unloading (C in Fig. 4-8(a))

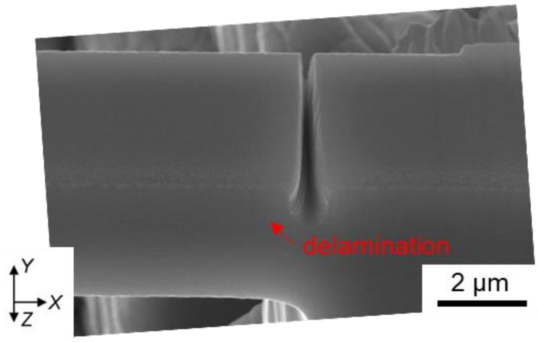

(e) Magnified image around the notch after Test OA1

Fig. 4-8: Continued.

Fig. 4-9 shows the *P*–*d* relationship and *in situ* SEM images of Test OA3 with a maximum displacement of d = 9.3 μm. During loading, a delamination crack spread approximately 20 μm from the notch, as shown in Fig. 4-9(c). Subsequently, at Point B: d = 7.5 μm, a discontinuous decrease in P was observed in the *P*–*d* relationship. Fig. 4-9(d) shows an SEM image at Point C: d = 8.0 μm immediately after the rapid decrease in P. An out-of-plane crack occurred at the notch root and was then arrested. Furthermore, damage occurred from the out-of-plane crack tip toward the free end of the cantilever.

This damage was not accompanied by an opening during the test, and was therefore considered a localized interlayer slip. After that, P increased again linearly with an increase in d, and the load at the maximum displacement $d = 9.3$ μm was $P_{max} = 0.20$ mN. No further downward progression of the out-of-plane crack was observed. After unloading at Point D, the plastic deformation remained in the specimen, as shown in Fig. 4-9(e). This corresponded to a loading-point displacement of approximately 2–3 μm. Fig. 4-9(f) shows the SEM image near the fixed end after the test. The out-of-plane crack extended approximately 480 nm below the notch root and was arrested. In summary, after delamination occurred, an out-of-plane crack was introduced from the notch root, and damage appearing to be an interlayer slip occurred from the out-of-plane crack tip toward the free end.

In Tests OA4–OA6, as the maximum displacement was further increased, the delamination cracks progressed further as well; however, no new out-of-plane cracks were observed.

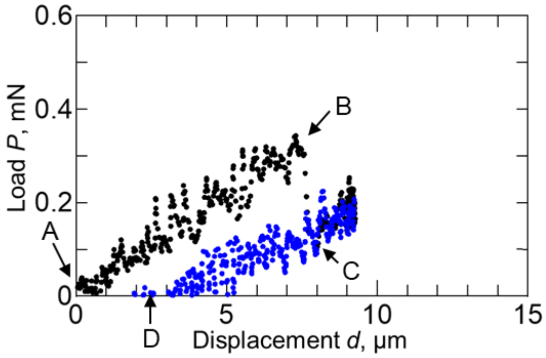

(a) Relationship between load P and displacement d in Test OA3

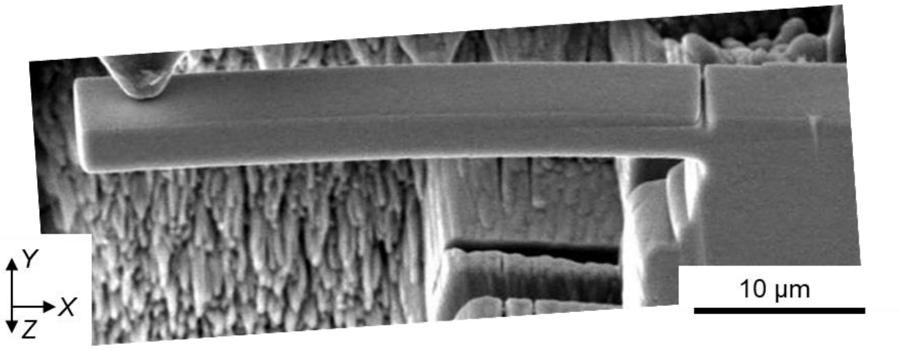

(b) Before loading (A in Fig. 4-9(a))

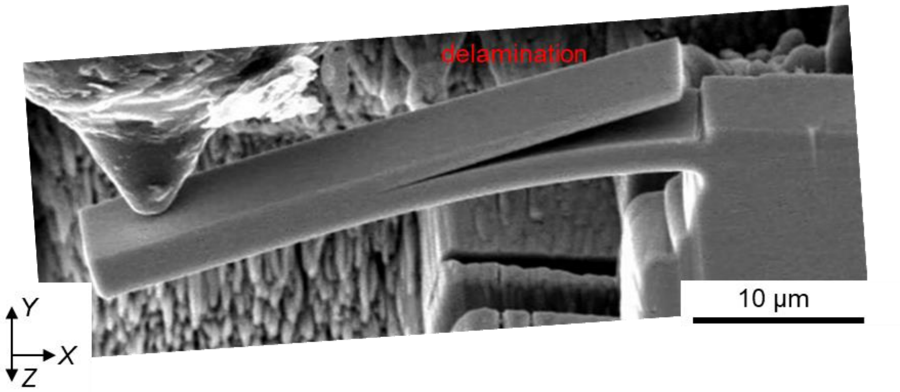

(c) Before out-of-plane crack initiation (B in Fig. 4-9(a))

Fig. 4-9: Experimental results of out-of-plane crack fracture toughness test in Test OA3. (b)–(e) show *in situ* SEM images in the test and (f) shows a SEM image around the notch after test.

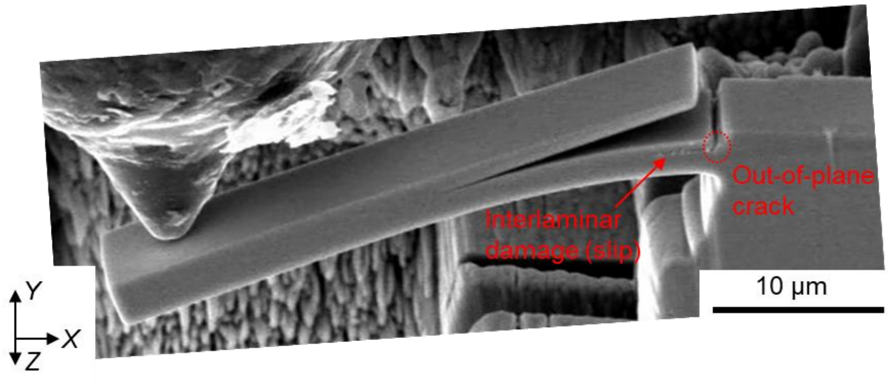

(d) Out-of-plane crack initiation and arrest (C in Fig. 4-9(a))

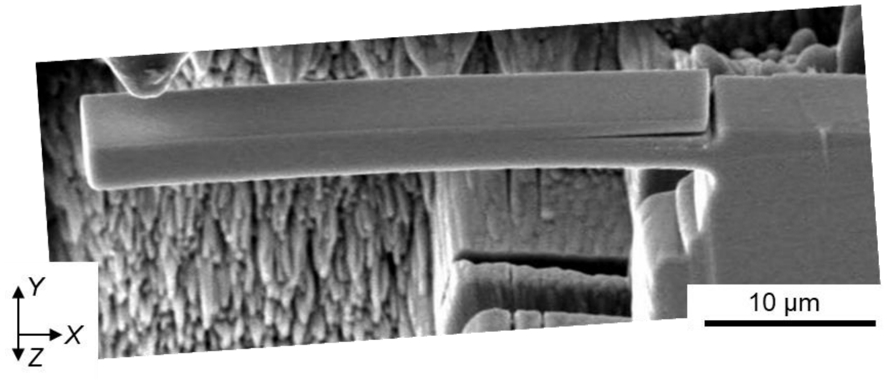

(e) After unloading (D in Fig. 4-9(a))

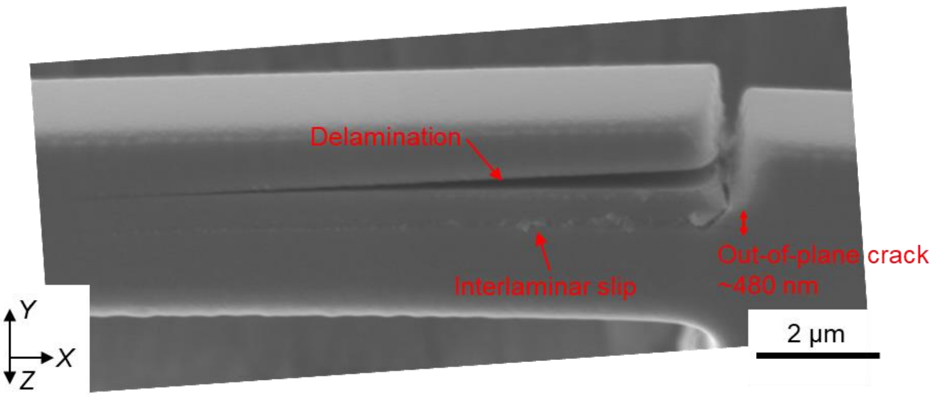

(f) Magnified image around the notch after Test OA3

Fig. 4-9: Continued.

b. Specimen OB

In the first test (Test OB1), with a maximum displacement of d = 5.7 μm and a beam height 1.6 times that of Specimen OA, a linear elastic P–d relationship was observed. Fig. 4-10(a) shows the P–d relationship of Test OB2 with a maximum displacement of d = 8.8 μm. During loading, P increased linearly as d increased, and P decreased rapidly at Point A: d = 7.3 μm. An SEM image at Point B: d = 7.7 μm is shown in Fig. 4-10(b). Delamination did not occur, but an out-of-plane crack occurred at the notch root, as seen in the magnified SEM image of the notch obtained after the test (Fig. 4-10(c)). After loading to a maximum displacement of d = 8.8 μm, the load was removed. During unloading, P decreased almost linearly as d decreased. The load at the maximum displacement was P_{max} = 1.2 mN. After unloading, the bending deformation of the specimen was almost restored. As shown in Fig. 4-10(c), the generated out-of-plane crack reached approximately 250 nm below the notch root. In addition, multiple localized interlayer slips toward the free and fixed ends were observed near the notch root. Thus, in Test OB2, an out-of-plane crack was introduced without delamination, and multiple interlayer slips occurred near the notch root.

Fig. 4-11 shows the P–d relationship and *in situ* SEM images of Test OB3 with a maximum displacement of d = 11.2 μm. At Point B (Fig. 4-11(c)), delamination occurred from the notch root and stably propagated toward the free end. During this period, no discontinuous changes in the load were observed. In the P–d relationship shown in Fig. 4-11(a), there were two discontinuous decreases in P, i.e., B: d = 9.2 μm → C: d = 9.4 μm and D: d = 10.6 μm → E: d = 11.2 μm. As shown in the red-dashed circle in Fig. 4-11(d), at B → C, a localized interlayer slip occurred in the fixed part of the specimen. At D → E, local buckling was observed near the bottom surface of the cantilever near the fixed end (yellow-dashed circle). After unloading at Point F, the plastic deformation remained in the specimen, as shown in Fig. 4-11(e). Fig. 4-11(f) shows the SEM image of the fixed section of the specimen after the test. Multiple interlayer slips were observed in the specimen. Thus, in Test OB3, no downward (out-of-plane) extension of the out-of-plane crack that was generated in Test OB2 was observed.

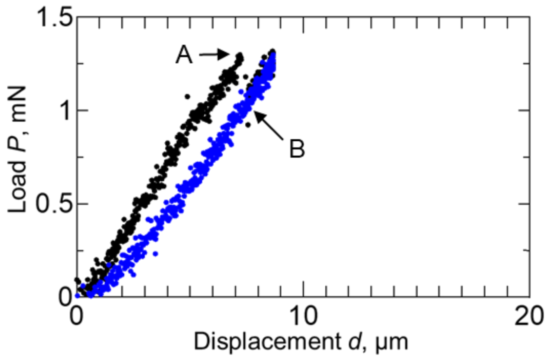

(a) Relationship between load P and displacement d in Test OB2

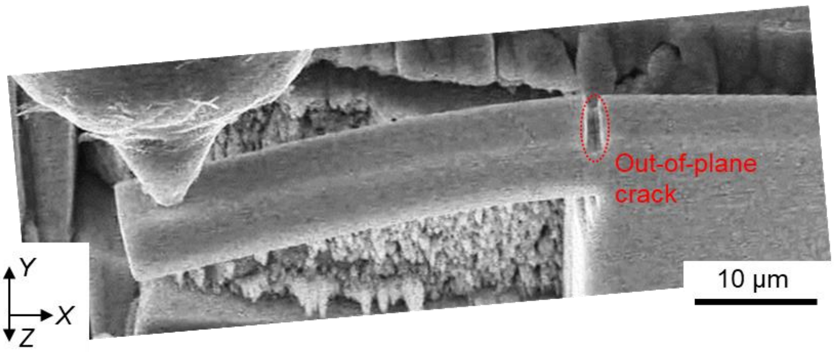

(b) Out-of-plane crack arrested (B in Fig. 4-10(a))

Fig. 4-10: Experimental results of out-of-plane crack fracture toughness test in Test OB2. (b) shows an *in situ* SEM image in the test and (c) shows a SEM image around the notch after test.

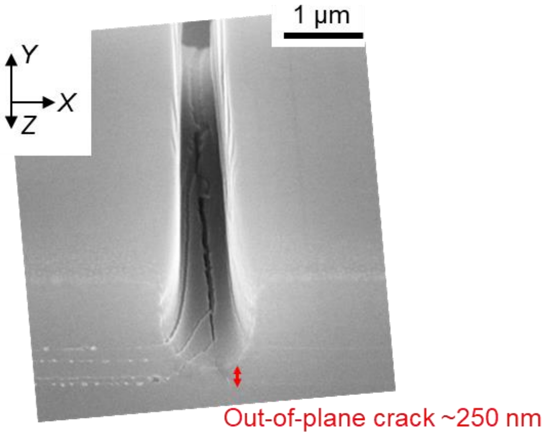

(c) Magnified image around the notch after Test OB2

Fig. 4-10: Continued.

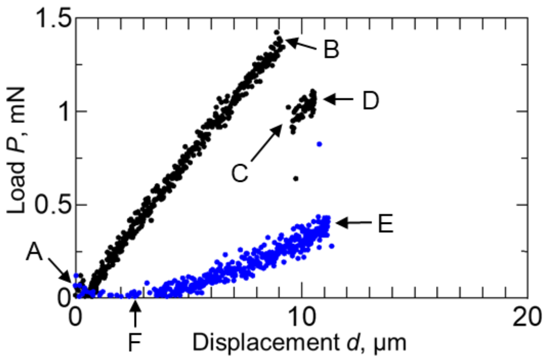

(a) Relationship between load P and displacement d in Test OB3

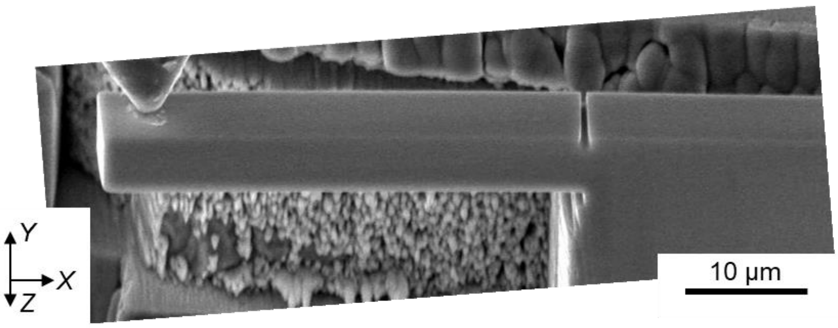

(b) Before loading (A in Fig. 4-11(a))

Fig. 4-11: Experimental results of out-of-plane crack fracture toughness test in Test OB3. (b)–(e) show *in situ* SEM images in the test and (f) shows a SEM image around the notch after test.

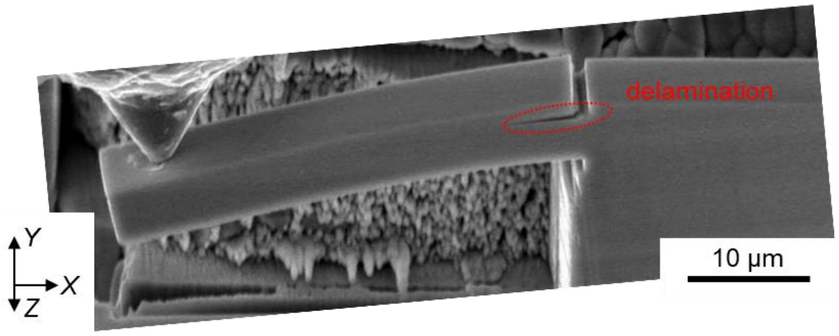

(c) Delamination from the notch (B in Fig. 4-11(a))

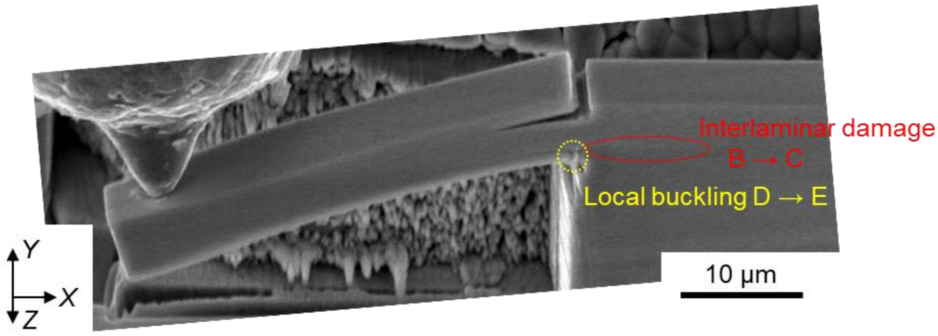

(d) At maximum displacement (E in Fig. 4-11(a))

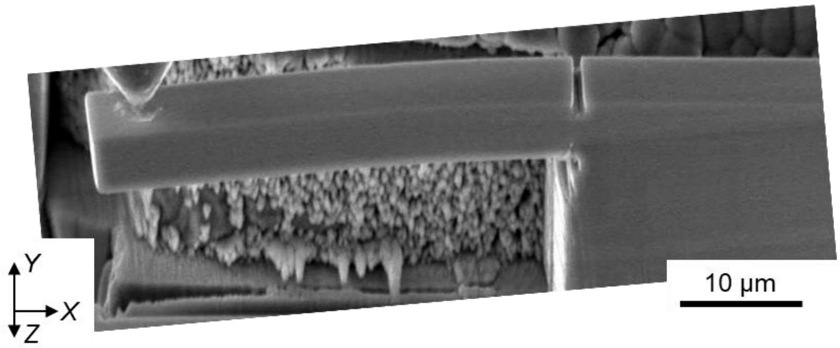

(e) After unloading

Fig. 4-11: Continued.

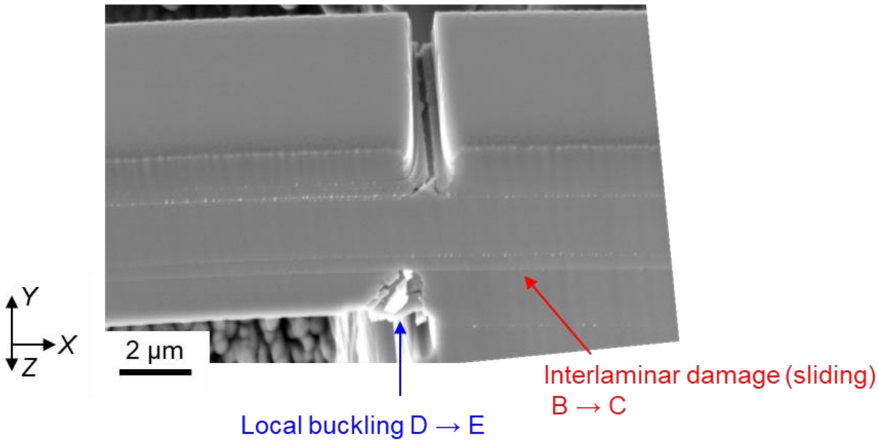

(f) SEM image around the notch after Test OB3

Fig. 4-11: Continued.

c. Specimen OC

Fig. 4-12(a) shows the *P*–*d* relationship of Test OC1 with a maximum displacement of *d* = 2.0 μm and a height 2.8 times that of Specimen OA. *P* decreased rapidly at Point A: *d* = 1.4 μm. No clear buckling or delamination occurred in the cantilever beam, and an out-of-plane crack was generated at the notch root, as shown in Fig. 13(b). An SEM image around the notch root after the test is shown in Fig. 4-12(c). The out-of-plane crack extended approximately 1100 nm downward from the notch root and was arrested. In Test OC1, pre-cracking was successful without delamination or other damage. Fig. 4-13(a) shows the *P*–*d* relationship of Test OC2 with a maximum displacement of *d* = 4.6 μm. As the loading progressed, an interlayer slip occurred in the direction of the free end of the cantilever from the pre-crack tip, and the crack tip blunted as shown in Fig. 4-13(b). *P* decreased rapidly at Point A: *d* = 3.0 μm, and the pre-crack progressed in the out-of-plane direction, as shown in Fig. 4-13(c). The critical load at the start of crack propagation was P_C = 1.6 mN. An SEM image around the notch after the test is shown in Fig. 4-13(d).

Compared with Test OC1, the out-of-plane crack extended downward from the pre-crack tip, and the crack length reached approximately 2000 nm from the notch root. In addition, an interlayer slip occurred in the direction of the free end of the cantilever from the crack tip. Thus, in Test OC2, the crack propagation test from the pre-crack tip was successfully conducted without delamination.

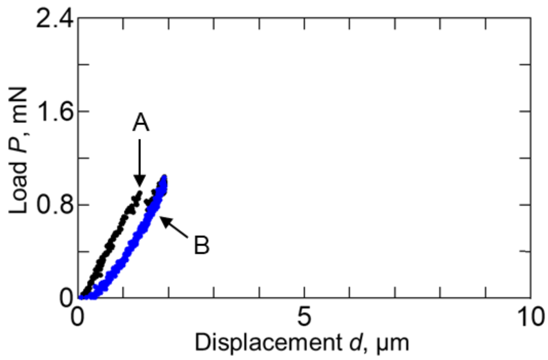

(a) Relationship between load P and displacement d in Test OC1

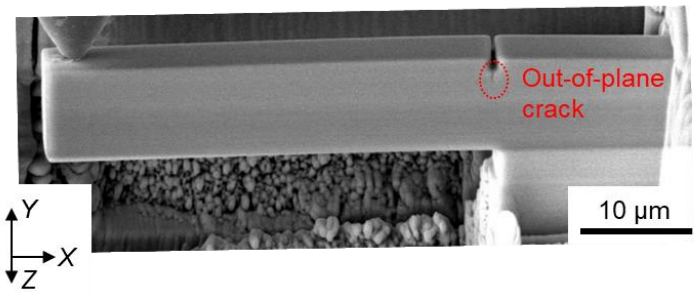

(b) Out-of-plane crack initiation and arrest (B in Fig. 4-12(a))

Fig. 4-12: Experimental results of out-of-plane crack fracture toughness test in Test OC1. (b) shows an *in situ* SEM image in the test and (c) shows a SEM image around the notch after test.

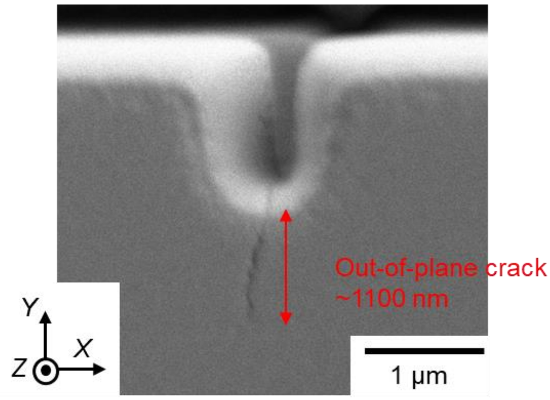

(c) SEM image around the notch after Test OC1

Fig. 4-12: Continued.

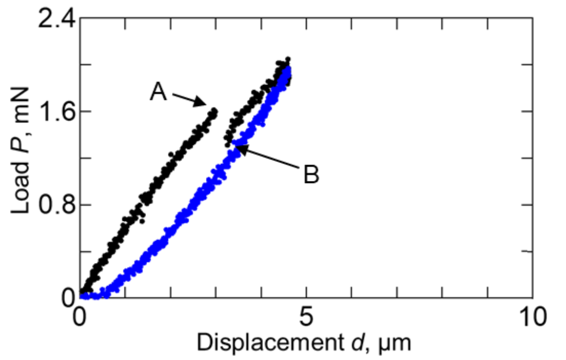

(a) Relationship between load *P* and displacement *d* in Test OC2

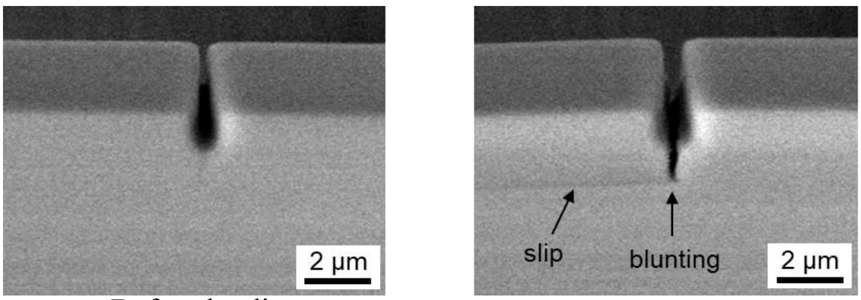

Before loading At critical load (A in Fig. 4-13(a))

(b) *In situ* SEM images under loading

Fig. 4-13: Experimental results of out-of-plane crack fracture toughness test in test OC2. (b) shows *in situ* SEM images in the test, (c) shows an *in situ* SEM image after crack propagation and arrest and (d) shows a SEM image around the notch after test.

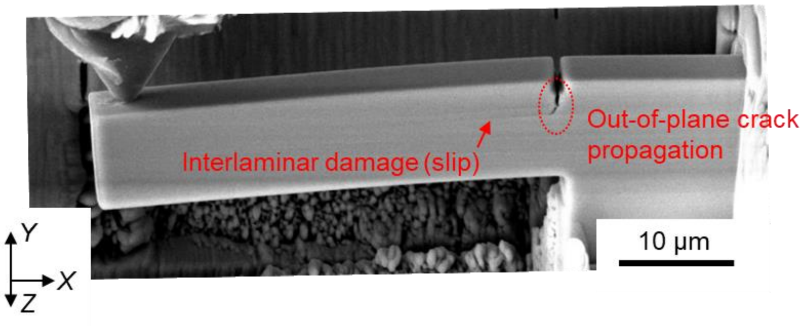

(c) After crack propagation and arrest (B in Fig. 4-13(a))

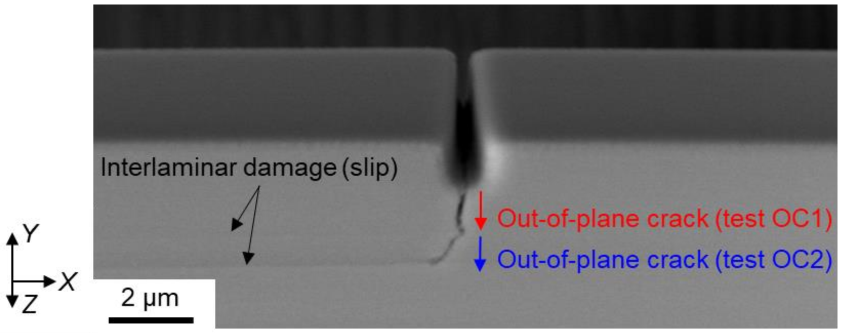

(d) SEM image of after Test OC2

Fig. 4-13: Continued.

4.3.3 High fracture toughness of out-of-plane crack

First, the apparent fracture toughness was evaluated under the continuum assumption. FEM analysis assuming vdW-layered $MoTe_2$ as a continuum body was performed, and the out-of-plane crack fracture toughness K_{C_O} was evaluated. Delamination was incorporated into the model as a delamination crack, as shown in Fig. S4-5, whereas interlayer slip was not considered. In Specimen OA, the out-of-plane crack (Fig. 4-9(f)) generated in Test OA3 was reproduced, and the crack length was set at Δa = 480 nm, which was uniform in the width direction (Z direction). A delamination crack of approximately 20 μm that occurred before the out-of-plane crack initiation (Fig. 4-9(C)) was introduced into the analysis model. In general, fracture toughness is evaluated using a critical load at the start of crack growth. However, because the out-of-plane crack introduced in Specimen OA did not propagate, the maximum stress intensity factor K_{max} at the maximum load P_{max} after the out-of-plane crack was introduced was estimated. In Test OA3, K_{max} = 1.4 MPa m$^{1/2}$ was determined at P_{max} = 0.20 mN. As the cracks did not propagate at P_{max}, the fracture toughness of the out-of-plane crack of Specimen OA was determined to be K_{C_O} > 1.4 MPa m$^{1/2}$.

In Specimen OB, the out-of-plane crack (Fig. 4-10(c)) of Δa = 250 nm introduced in Test OB2 was modeled, and K_{max} = 2.1 MPa m$^{1/2}$ was determined at P_{max} = 1.2 mN. Therefore, the out-of-plane crack fracture toughness of Specimen OB was K_{C_O} > 2.1 MPa m$^{1/2}$.

In Specimen OC, the critical load P_C at the start of out-of-plane crack growth from the introduced pre-crack tip (Fig. 4-12(c)) was obtained. Using the out-of-plane crack length Δa = 1100 nm generated in Test OC1 and the critical load P_C = 1.6 mN in Test OC2, K_{C_O} = 1.8 MPa m$^{1/2}$ was determined. This was approximately twice the fracture toughness of the in-plane crack K_{C_I} = 0.82–1.07 MPa m$^{1/2}$. These values are summarized in Table 4-3.

The out-of-plane fracture toughness K_{C_O} evaluated using vdW-layered $MoTe_2$ exceeded the in-plane fracture toughness K_{C_I} of the same material. The fracture toughness of brittle materials without plastic deformation reflects the strength of the interatomic bond at the crack tip [9]. If the fractures for the in-plane and out-of-plane cracks are completely brittle, the fracture toughness should be equal. However, the apparent fracture toughness evaluated by the stress analysis based on the continuum assumption was higher for out-of-plane cracks than for in-plane cracks. This indicates that some type of stress relaxation mechanism works on the out-of-plane cracks.

In Specimen OA, delamination occurred before the occurrence of an out-of-plane crack. When the layers are separated at a delamination crack, the interaction between the layers completely disappears, and the stress transmission is cut off. In this case, the stress concentration of the notch disappears; thus, delamination reduces the driving force for the occurrence of an out-of-plane crack. It should be noted that in the above K_{C_O} evaluation, the effect of delamination was considered by introducing delamination cracks into the model. Nevertheless, K_{C_O} was estimated to be higher than K_{C_I}, suggesting another stress relaxation mechanism.

In all tests, multiple localized interlayer slips occurred before and after the occurrence of out-of-plane cracks (e.g., Fig. 4-10(c) and 4-13(b)). It is inferred that this interlayer slip is the key to high fracture toughness. It is known that in vdW-layered materials such as graphite, once interlayer slip occurs under deformation, the interlayer configuration changes from a well-matched commensurate state to an incommensurate contact; thus, the resistance to slip becomes extremely low, showing superlubricity [10, 11]. Therefore, a deformation analysis using the discrete model shown in Fig. 4-4 was conducted to incorporate this interlayer slip. Fig. 4-14(a) and (b) show the results of the continuum analysis and the analysis using the semi-discrete layer model for Specimen OC (Test OC2). Both figures show the deformation and the distribution of normal stress σ_x at the critical load P_C. In the continuum model, a singular stress field was generated at the crack tip, whereas in the semi-discrete layer model, the crack tip was blunted by interlayer slip originating at the crack tip. In the semi-discrete layer model, interlayer slip also occurred in other regions and large deformation was accommodated. As shown in the *in-situ* SEM image of the crack tip in Fig. 4-13(b), the crack tip blunted as the deformation progressed, indicating that interlayer slip occurred at the crack tip. This is consistent with the analysis results shown in Fig. 4-14(b). Fig. 4-14(c) shows the σ_x field near the crack tip. For comparison, the results of continuum models (in-plane and out-of-plane cracks) without consideration of interlayer slip are also shown. In the continuum models, a singular stress field was formed at the crack tip and showed high stress. On the other hand, in the semi-discrete layer model considering interlayer slip, the singular stress field disappeared and became a finite stress field. The maximum stress was ~ 1.6 GPa.

In the out-of-plane crack test, localized interlayer slip occurred as the deformation progressed, and the singular stress field disappeared due to this discrete nature. Therefore, the fracture mechanics concept, which evaluates fracture toughness in terms of the intensity of the singular field, is not valid. On the other hand, since the in-plane crack has a singular stress field (as shown in blue line in Fig. 4-14(c)), the fracture toughness is characterized by the stress intensity factor *K*. For this reason, it is not possible to strictly compare their strengths. Nevertheless, the "apparent" fracture toughness K_{C_O} evaluated from the continuum stress analysis for the out-of-plane crack, which did not consider interlayer slip, was higher than that of the in-plane crack, K_{C_I}. In addition, as shown in Fig. 4-14(c), the stress in the semi-discrete layer model for the out-of-plane crack was also higher than that of the in-plane crack in the surrounding region except in the region near the crack tip. Therefore, out-of-plane cracks have a higher resistance to crack propagation than in-plane cracks. This experiment and analysis demonstrated that vdW-layered materials exhibit high fracture toughness for out-of-plane cracks.

In addition, the bending tests of smooth cantilever specimens without notches (Specimens OS-I and OS-II) did not cause delamination and caused local interlayer slip, which allowed a large bending deformation without breaking (Supplementary Material

S3.1) [12]. This result indicates that vdW-layered materials prevent the generation of high stress that breaks the interatomic bond in the in-plane direction through the occurrence of interlayer slip due to weak vdW interaction under bending deformation.

The vdW-layered materials have high deformability accompanied by interlayer slip, and they are less likely to cause stress concentration and singular stress fields at notches and cracks. Therefore, vdW-layered materials can achieve not only high toughness and flexibility but also high strength. In this study, we have partially demonstrated this, but the mechanical law of deformation and fracture in such semi-discrete structures has not been completely elucidated. For example, it would be interesting to determine the mechanics of the initiation and propagation of interlayer slip and delamination, as well as fatigue and creep characteristics, which we plan to study in the near future.

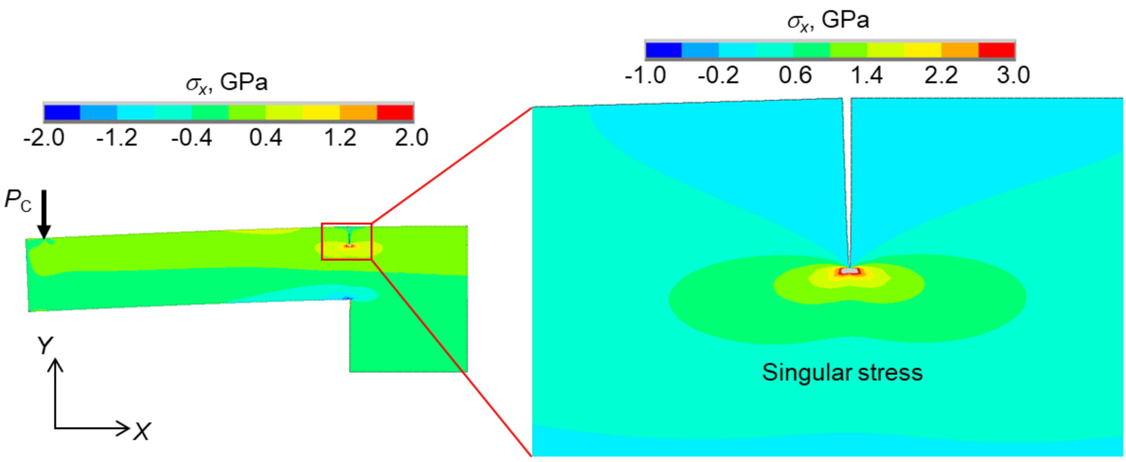

(a) Deformation and stress distribution in continuum model

Fig. 4-14: Disappearance of stress singularity of the out-of-plane crack in vdW-layered material. Stress singularity at the crack tip disappears owing to the interlayer slips due to the discreteness.

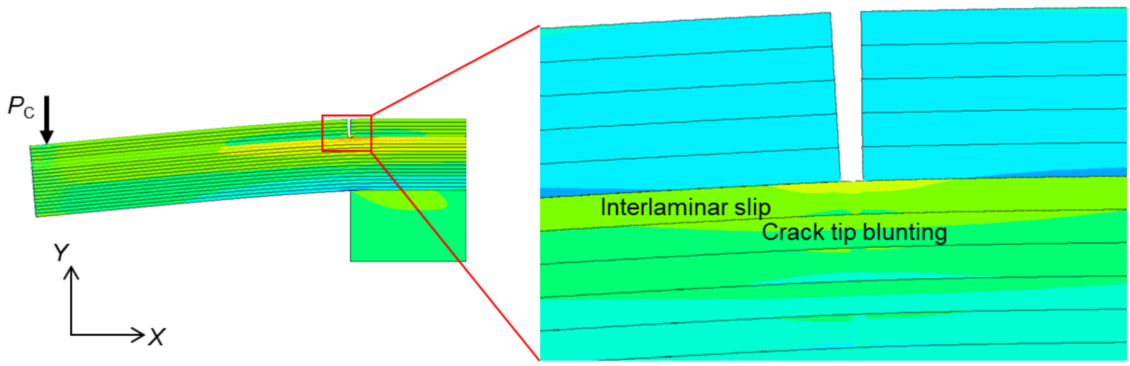

(b) Deformation and stress distribution in semi-discrete layer model

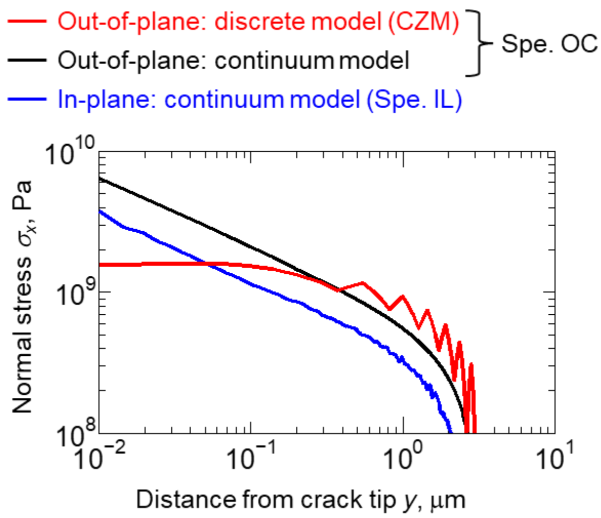

(c) Stress distribution near the crack tip at the critical load. Stress singularity disappears

Fig. 4-14: Continued.

4.4 Conclusions

The purpose of this chapter is to elucidate the fracture mechanism in vdW-layered materials and experimentally demonstrate the high fracture toughness owing to the disappearance of the singular stress field. We conducted fracture toughness tests for in-plane and out-of-plane cracks in microscale vdW-layered $MoTe_2$. The results are summarized as follows.

In the in-plane crack fracture toughness test using a cantilever-type chevron-notched specimen, an in-plane crack initiated and propagated from the chevron notch. Based on the experimental results, an FEM stress analysis, assuming a continuum body (anisotropic linear elastic body), was performed to evaluate the fracture toughness. The in-plane crack fracture toughness K_{C_I} of this material was evaluated as 0.82–1.07MPa m$^{1/2}$. An out-of-plane fracture toughness test was performed using a cantilever specimen with a notch. In the specimen with a small cantilever thickness, delamination occurred from the vicinity of the notch root, and then a crack was initiated in the out-of-plane direction from the notch root and was arrested. Interlayer slips were also observed at that time. When the specimen thickness increased, an out-of-plane crack was generated and arrested from the notch root without delamination, and multiple interlayer slips were observed. In the thickest specimen, a crack propagation test from the pre-crack tip was successfully conducted without delamination. The crack tip was blunted by interlayer slip originating at the crack tip. Although interlayer slips occurred prior to crack growth, the out-of-plane crack "apparent" fracture toughness was evaluated based on the continuum assumption, without considering the slip. The out-of-plane crack apparent fracture toughness K_{C_O} was determined as 1.8 MPa m$^{1/2}$, which was roughly twice that of the in-plane crack fracture toughness K_{C_I}. In addition, a deformation analysis was performed using a CZM to incorporate discrete interlayer slip. The result indicates that the crack tip was blunted by interlayer slip originating at the crack tip and the singular stress field disappeared due to the discrete nature. Therefore, out-of-plane cracks have a higher resistance to crack propagation than in-plane cracks. This experiment and analysis demonstrated that vdW-layered $MoTe_2$ exhibits a high fracture toughness against out-of-plane cracks.

References

[1] T. Sumigawa, H. Hirakata, M. Takemura, S. Matsumoto, M. Suzuki, and T. Kitamura, Disappearance of stress singularity at interface edge due to nanostructured thin film, *Eng*. *Fract*. *Mech*. **75**, 3073 (2008)

[2] B. S. Li, T. J. Marrow, S. G. Roberts, and D. E. J. Armstrong, Evaluation of fracture toughness measurements using chevron-notched silicon and tungsten microcantilevers, *New Developments in Nanomechanical Methods* **71**, 3378(2019).

[3] M. G. Mueller, V. Pejchal, G. Zagar, A. Singh, M. Cantoni, and A. Mortensen, Fracture toughness testing of nanocrystalline alumina and fused quartz using chevronnotched microbeams, *Acta Mater*. **86**, 385(2015).

[4] ASTM-E1304-97(2020). Standard Test Method for Plane-Strain (Chevron-Notch) Fracture Toughness of Metallic Materials.

[5] D. Munz, R. T. Bubsey, and J. L. Shannon Jr., Fracture toughness determination of Al203 using four-point-bend specimens with straight-through and chevron notches, *J*. *Am*, *Ceram*. *Soc*. **63**, 300(1980).

[6] C. M. O. Bastos, R. Besse, J. L. F. Da Silva, and G. M. Sipahi, Ab initio investigation of structural stability and exfoliation energies in transition metal dichalcogenides based on Ti-, V-, and Mo-group elements, *Phys*. *Rev*. *Mater*. **3**, 044002(2019).

[7] S. Rubanov and P. R. Munroe, FIB-induced damage in silicon, *J. of Microscopy* **214**, 213(2004).

[8] J. Mayer, L. A. Giannuzzi, T. Kamino, and J. Michael, TEM sample preparation and FIB-induced damage, *MRS Bull*. **32**, 400(2007).

[9] T. Sumigawa, T. Shimada, S. Tanaka, H. Unno, N. Ozaki, S. Ashida, and T. Kitamura, Griffith criterion for nanoscale stress singularity in brittle silicon, *ACS Nano* **11**,

6271(2017).

[10] Z. Liu, J. R. Yang, F. Grey, J. Z. Liu, Y. L. Liu, Y. B. Wang, Y. L. Yang, Y. Cheng, and Q. S. Zheng, Observation of microscale superlubricity in graphite, *Phys*. *Rev*. *Lett*. **108**, 205503(2012).

[11] E. M. Han, J. Yu, E. Annevelink, J. Son, D. A. Kang, K. Watanabe, T. Taniguchi, E. Ertekin, P. Y. Huang, and A. M. van der Zande, Ultrasoft slip-mediated bending in few-layer graphene, *Nat*. *Mater*. **19**, 305(2020).

[12] M. Akiyoshi, S. Koike, T. Shimada, and H. Hirakata, Bending deformation and self-restoration of submicron-sized graphite cantilevers, *Acta Materialia* 241, 118381(2022).

Chapter 5

Conclusions

The purpose of this study was to elucidate the mechanics of deformation and fracture of vdW-layered materials. Focusing on the deformation under out-of-plane loading, the bending deformation characteristics and self-restoration properties were experimentally clarified. Then, considering the microscopic mechanism of bending deformation of vdW-layered materials (i.e., discrete interlayer slip), a mechanical model that universally reproduced the characteristic nonlinear and self-restoration deformation characteristic was constructed. Furthermore, the fracture mechanisms in vdW-layered materials were determined and the high fracture toughness owing to the disappearance of the singular stress field is experimentally demonstrated.

In Chapter 2, *in situ* TEM bending deformation experiments were conducted on submicron-sized HOPG cantilevers to determine the bending deformation characteristics and self-restoring properties. It was clarified that the loading–unloading curves were nonlinear, indicative of reversible behavior, and contained a large hysteresis loop. Moreover, similar loading–unloading curves were obtained during multiple loading tests performed on the same specimen, indicating that the mechanical properties of the specimens were restored upon unloading, even in the case of large nonlinear deformations. As the deformation increased, plastic deformation occurred, and the self-restoration property was lost. However, no clear fracture was observed in the cantilevers. The nonlinearity of the load–displacement curves can probably be ascribed to a reduction in the stiffness because of the occurrence and propagation of interlayer slip in the high shear stress region. The results confirmed that vdW-layered materials can accommodate large out-of-plane bending deformations without fracturing and that these deformations are reversible. As a result, these materials exhibit high durability against repeated loading.

In Chapter 3, a mechanical model that reproduces the characteristic nonlinear and reversible deformation of vdW-layered materials by considering microscopic mechanisms (discrete interlayer slips) was developed. The vdW-layered material was modeled as a stack of interacting discrete deformable layers (semi-discrete layer model), and the interlayer interaction was modeled using a CZM that reproduced the localized interlayer slip. A bending deformation analysis was performed on the HOPG and $MoTe_2$ cantilevers. The analysis using a semi-discrete layer model with a recombination CZM accurately reproduced the deformation characteristics for submicron HOPG cantilevers, or the large nonlinear and reversible deformation with a hysteresis loop. The interlayer slip accompanied by a shear fracture and recombination occurred in both the loading and unloading processes, thus resulting in a large nonlinear deformation and energy dissipation. The delaminated region expanded as loading proceeded and the stored elastic strain energy in each deformable layer almost completely restored the shape of the cantilever upon unloading. In addition, the bending analysis using a semi-discrete layer model with a fracture CZM reproduced well the characteristics of bending experiments for micro $MoTe_2$ cantilevers, or the intermittent decreases in stiffness during the loading process and deformation restoration during the unloading process. These results indicated that the semi-discrete layer model developed in this study is universally applicable for reproducing the bending deformation characteristics of vdW-layered materials. This was not possible with conventional continuum models.

In Chapter 4, fracture toughness tests were conducted for in-plane and out-of-plane cracks in microscale vdW-layered $MoTe_2$. The in-plane crack fracture toughness of this material was evaluated as 0.82–1.07 MPa $m^{1/2}$. In the out-of-plane fracture toughness test, the pre-crack tip was blunted by interlayer slip originating at the crack tip and then the crack was initiated to propagate. Although interlayer slips occurred prior to crack growth, the out-of-plane crack "apparent" fracture toughness was evaluated based on the continuum assumption, without considering the slip. The out-of-plane crack apparent fracture toughness was determined as 1.8 MPa $m^{1/2}$, which was roughly twice that of the in-plane crack fracture toughness. In addition, a deformation analysis was performed using the semi-discrete layer mode developed in Chapter 3 to incorporate discrete interlayer slip. The result indicated that the crack tip was blunted by interlayer slip originating at the crack tip and the singular stress field disappeared due to the discrete nature. Therefore, out-of-plane cracks have a higher resistance to crack propagation than in-plane cracks. This experiment and analysis demonstrated that vdW-layered $MoTe_2$ exhibits a high fracture toughness against out-of-plane cracks.

Regarding the mechanics of deformation and fracture on vdW-layered materials, there are some unresolved issues as follows. In bending deformation, it is well known that the dimensional dependence of stiffness does not follow the continuum theory. The semi-discrete layer model constructed in this study reproduces discrete features well. Therefore, it will be a powerful model for elucidating the size dependence of the bending stiffness of vdW-layered materials. This study focused on deformation and fracture characteristics under monotonous loading. However, there is diversity in deformation and fracture phenomena. These include creep deformation under a constant load, fatigue due to cyclic loads, and fracture assisted by the surrounding environment. When considering the long-term reliability of devices using vdW-layered materials, it is essential to elucidate the characteristics of these deformations and fractures It will be possible to study them by further developing the experimental methods and mechanical models developed in this study. Furthermore, vdW-layered materials exhibit rich physical properties such as electrical and chemical properties in addition to mechanical properties. There are many unknown problems regarding multiphysics phenomena between mechanical properties and other physical properties. By elucidating the laws governing deformation and fracture, it will be possible to study the interplay with other physical properties, and thereby the material functions can be utilized to the maximum. This leads to various engineering applications and has a large ripple effect. This research will be the beginning of achieving this goal.

Supplementary Materials on Chapter 2

S2.1 Specimen preparation by FIB

The specimens were fabricated from the HOPG bulk material by FIB milling such that the stacking direction of the graphene coincided with the thickness direction of the cantilever. The procedure for fabricating the specimens is shown in Fig. S2-1 and detailed below.

1) The orientation of the bulk material was adjusted so that the y-direction in Fig. S2-1(a) was the stacking direction of the graphene. The FIB was irradiated (irradiation current: 76.56 nA) from the p-axis direction, or negative z-direction, to remove the white region in Fig. S2-1(a) and create a prismatic block.

2) The stage was tilted by 60° around the y-axis, and the beam was irradiated (current: 22.66 nA) from the p-direction to deeply cut the area along the thick black line in Fig. S2-1(b) to create a gap.

3) The stage was tilted by -60° around the y-axis and by 90° around the z-axis. The probe tip was adhered to the edge of the prismatic block, as shown in Fig. S2-1(c), by tungsten deposition using an ion-induced method (hereafter referred to as “W depo”). The beam was irradiated from the p-direction with an irradiation current of 0.84 nA to cut the area along the thick black line in Fig. S2-1(c), which completely separated the prismatic block with a side length of ~10 μm from the bulk material.

4) The block was moved in the z-direction and irradiated (current: 3.91 nA) from the p-direction, as shown in Fig. S2-1(d), to shave the area along the thick black line and make the sample flat. It was then moved to the sample stage.

5) The sample stage and the block were glued together at the grid area in Fig. S2-1(e)

using W depo. The beam was irradiated from the *p*-direction with an irradiation current of 0.84 nA to cut the area along the thick black line and separate the probe from the block.
6) To firmly fix the block on the sample stage, the stage was rotated by 180° around the *y*-axis, and the grid area was glued using W depo, as shown in Fig. S2-1(f).
7) Fig. S2-1(g) shows a top view of the block. The beam was irradiated (current: 3.91 nA) from the *p*-direction, and the area outside the solid lines in Fig. S2-1(h) was shaved. The beam was irradiated (current: 0.12–0.84 nA) from the *p*-direction, and the dotted region between the two thick black lines was shaved. At this time, the stage was rotated by ±1.2° around the *x*-axis to keep the width of the specimen in the *z*-direction constant, given the effects of flaring.
8) The stage was rotated by 90° around the *x*-axis, and the beam was irradiated from the *p*-direction, as shown in Figs. S2-1(i) and (j), with an irradiation current of 0.12 nA to scrape the grid area. Subsequently, the beam was irradiated (current: 0.01 nA) from the *p*-direction to shave the dotted area. The stage was tilted by ±1.2° around the *x*-axis to keep the height of the specimen constant in the *y*-direction, given the effects of flaring.

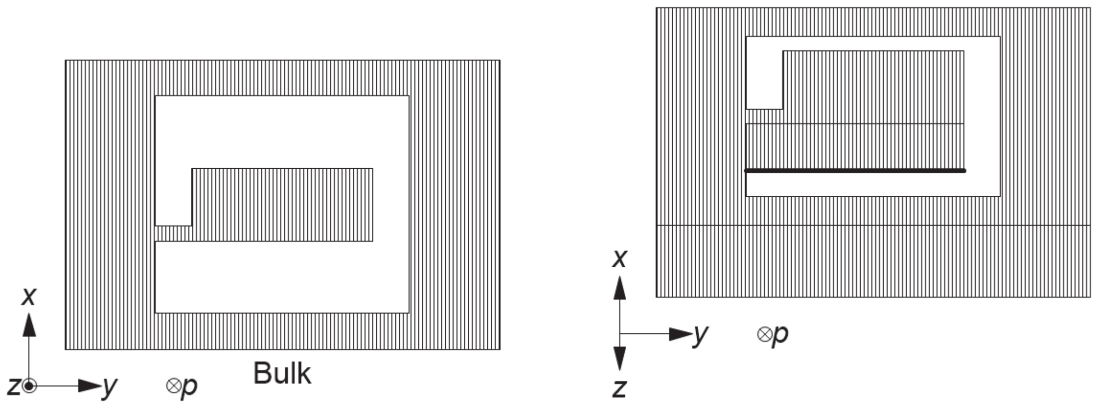

(a) 1st process (b) 2nd process

Fig. S2-1: The procedure for fabricating the specimens

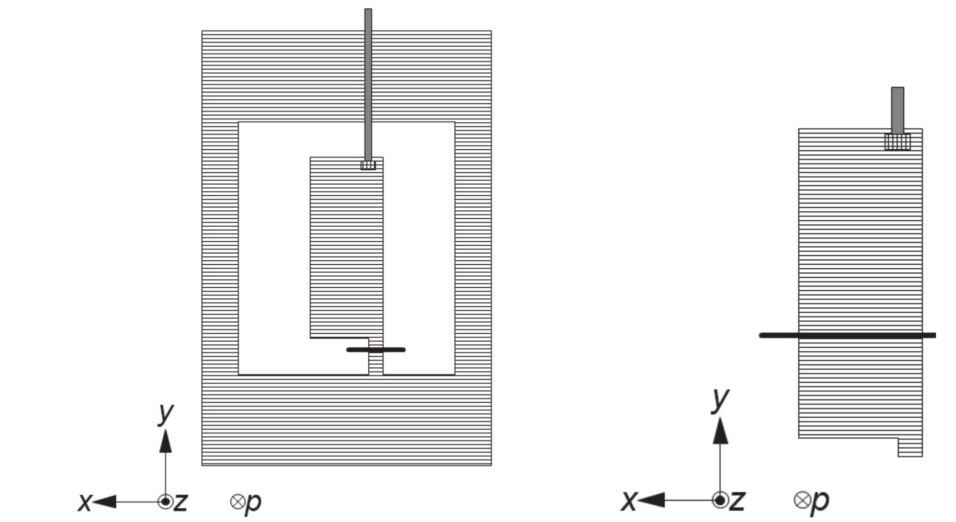

(c) 3^{rd} process (d) 4^{th} process

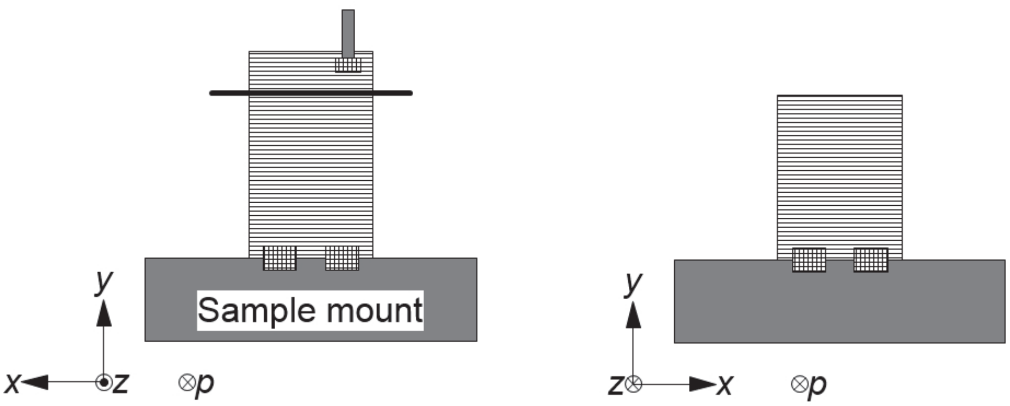

(e) 5^{th} process (f) 6^{th} process

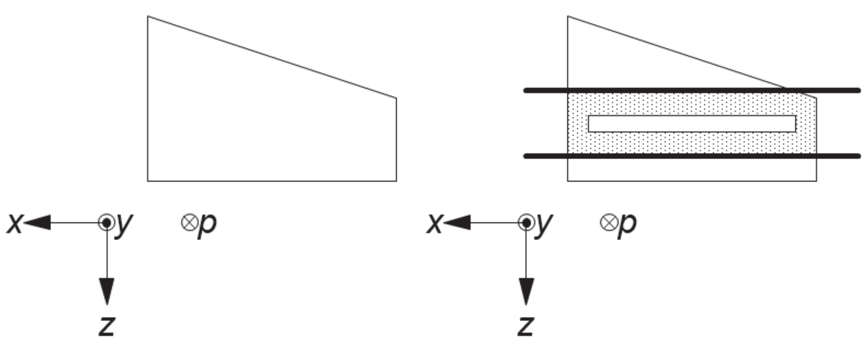

Fig. S2-1: Continued.

(g) 7th process (h) 8th process

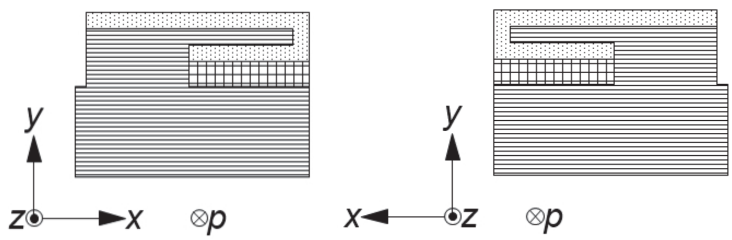

(i) 9th process (j) 10th process

Fig. S2-1: Continued.

S2.2 Specifications of loading apparatus and experimental conditions

Table S2-1 shows the specifications of the loading apparatus used in this study [1].

Table S2-1: Specifications of loading apparatus used

Maximum force	1.5 mN
Load resolution	≤ 3 nN
Load noise floor	200 nN
Maximum displacement	5 μm
Displacement resolution	≤ 0.02 nm
Displacement noise floor	0.4 nm

The order of the experiments and the maximum displacement, d_{max}, for each specimen are listed in Table S2-2. Multiple experiments with different d_{max} were performed for each specimen.

Table S2-2: Order and d_{max} (nm) of experiments for each specimen

Sample / Exp. no.	1	2	3	4	5	6	7	8	9	10	11
1st	17	166	64	239	150	187	97	76	47	122	69
2nd	34	180	90	398	368	284	55	63	72	162	72
3rd	13	152	112	507	475	284	18	62	82	205	48
4th	82	173	130	614	219	322		98	106		86
5th	136	275	125	757	347	347		134	157		92
6th	104	334	156	1070	341	403		168	181		111
7th	125	392	175	984	525	432		182	266		119
8th	131	412	186	1206	716	466		182	331		173
9th	166	411	199	1349		381		154	434		177
10th	212	446	200					179			143
11th	300	558	245					103			203
12th	320	707	315					199			242
13th	352	825	375					81			268
14th	245		495					83			211
15th	382		630					17			209
16th	485							59			236
17th	687							150			389
18th								208			413
19th								262			445
20th								306			549
21st								380			994
22nd								467			
23rd								602			
24th								669			
25th								648			

S2.3 Machine compliance

As the machine compliance (the reciprocal of the rigidity of the specimen and loading device other than the cantilever) differed for each specimen, the machine compliance C_m (m/N) was evaluated for all specimens to correct the displacement. The displacement of the loading point was measured from the TEM images, and C_m was estimated from the difference between the evaluated displacement and that measured by the displacement meter. The values of C_m are listed in Table S2-3. The displacement d_m measured by the displacement meter was corrected by applying the following equation.

$d = d_m - C_m P$ (S2-1)

where d is displacement and P is load.

Table S2-3: Machine compliance of each specimen

Specimen no.	1	2	3	4	5	6	7	8	9	10	11
Machine compliance C_m, 10^{-4} m/N	7.5	2.3	12.4	10.9	1.8	6.4	0.8	2.4	0.9	1.0	11.8

S2.4 SEM analysis of FIB-induced damage

Fig. S2-2 shows an SEM image of the fracture surface of the FIB-milled graphite specimen. A striped morphology, reflecting the layered structure of graphite, was present across most of the fracture surface. However, there was flat area near the processed surface. This region is considered to be the FIB processing damage layer, and its thickness was approximately 25 nm.

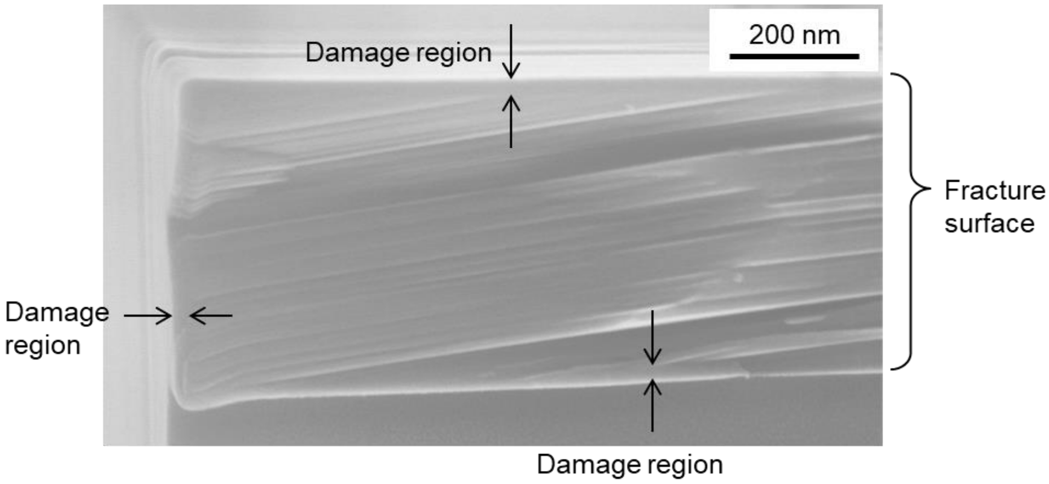

Fig. S2-2: SEM image of fracture surface of FIB-milled graphite specimen

S2.5 Relative intensity of D to G band in Raman spectra

The relative intensity of the D band to the G band in the Raman spectra of samples A and B is shown in Table S2-4.

Table S2-4: Relative intensity of D to G band in Raman spectra

Sample	Location	Electron beam	I_D/I_G
A	Free end	Non-irradiated	0.45
A	Free end	80 kV	0.48
A	Fixed end	Non-irradiated	0.45
A	Fixed end	80 kV	0.44
B	Free end	Non-irradiated	0.58
B	Free end	200 kV	0.59
B	Fixed end	Non-irradiated	0.59
B	Fixed end	200 kV	0.60

S2.6 FEM analysis of the bending properties of cantilever specimen

S2.6.1 Analysis method

The elastic deformation of the submicron-sized graphite cantilevers was analyzed using the finite element method (FEM). FEM software (Abaqus 2017) was used for the analysis. Fig. S2-3(a) shows the analytical model. Parametric analysis was performed with different heights (h = 300–500 nm) and lengths (L_p = 1300–1800 nm, measured from the fixed end to the loading point), where plane strain was assumed. To verify the validity of the plane analysis, three-dimensional (3D) analysis was also performed on Specimen 1 (Fig. S2-3(b)). The dimensions and shape of each specimen were reproduced with accuracy. As shown in the magnified view in Fig. S2-3(b), the corner shape at the fixed edge of the cantilever was measured from the TEM image, and a filet part with a radius of curvature R = 20 nm was modeled. Both the height and length of the cantilever support (left region in Fig. S2-3) were set to 3 μm, and the bottom face was completely fixed. The graphite was assumed to be an orthotropic elastic material, and the values shown in Table 2-3 were used as its elastic constants. The diamond indenter was modeled as a hemisphere in the 3D analysis, or a semicircle in the plane analysis, with a radius of 250 nm, Young's modulus of 1140 GPa, and Poisson's ratio of 0.07, based on an assumption of an isotropic elastic material. In the 3D analysis, a hexahedral 20-node quadratic element was used for the specimen, and a tetrahedral 10-node quadratic element was used for the indenter. An eight-node biquadratic element was used in the plane strain analysis. Geometrical nonlinearity was assumed, and the contact between the cantilever and indenter was set to be frictionless. The top surface of the indenter was subjected to displacement in the negative y-direction, as shown in Fig. S2-3.

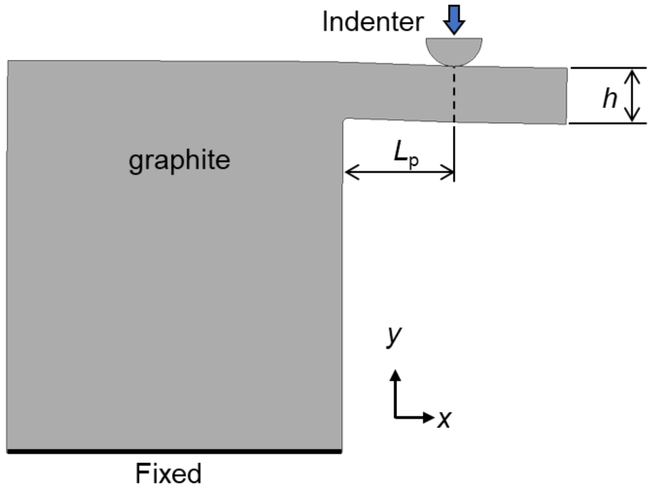

(a) Plane strain model

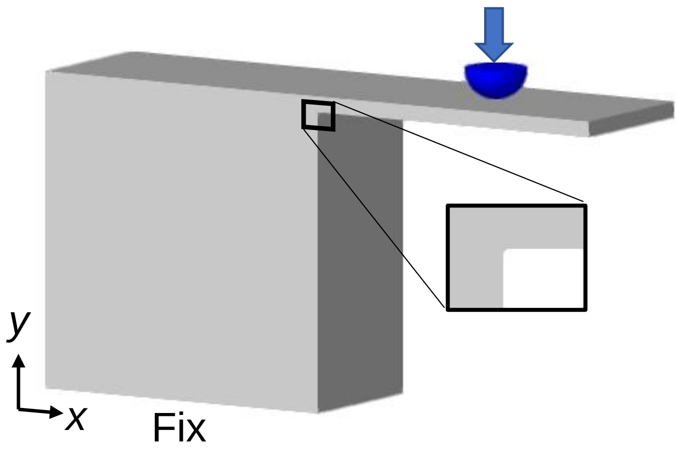

(b) 3D model

Fig. S2-3: Models for cantilever specimen used in FEM analysis

S2.6.2 Comparison between plane strain and 3D analyses

As shown in Figs. S2-3(a) and (b), 3D FEM analysis was performed for a cantilever specimen (Specimen 1), and the results were compared with those obtained from the plane strain analysis. The initial stiffnesses *S* according to these analyses were 0.31×10^9 N/m^2 (plane stain model) and 0.28×10^9 N/m^2 (3D model). Thus, the plane strain analysis provides a good approximation, although the stiffness is slightly overestimated. Therefore, in the parametric analysis, the plane strain analysis results were used considering the calculation cost.

S2.6.3 Effect of cantilever height and length on bending stiffness

Fig. S2-4 shows the dependence of the bending rigidity S of the cantilever per unit width on h and L_p. Here, S is the slope of the initial linear region of the normalized load–displacement ((P/w)–d) curve. As shown in Fig. S2-3(a), when h is constant, S decreases monotonically with increasing L_p. Fig. S2-4(b) shows the relationship between S and the normalized height (h/L_p). Although there is some variation due to the difference in h, S increases monotonically with increasing h/L_p and is distributed on approximately one curved band. In this range of h and L_p, S is roughly proportional to $(h/L_p)^{1.3}$. The least-squares approximation using the power law $S = k(h/L_p)^{\alpha}$ can be used to determine the value of the exponent ($\alpha = {\sim}1.3$). Thus, the height dependence of the bending stiffness of the cantilevers lies between the linear and cubic laws even in the continuum theory. S of the specimens does not obey the cubic law ($\alpha = 3$), but rather is close to a linear law ($\alpha = {\sim}1.3$).

This is because h of the cantilever specimens is approximately 1/5–1/3 of L_p, and comparable bending and shearing stresses act on the cantilever, so the beam approximation is not valid. In addition, graphite has strong elastic anisotropy, and the elastic constant C_{11} for in-plane deformation, which is dominant in bending deformation, is two orders of magnitude larger than the elastic constant C_{44} for shear deformation (as shown in Table 2-3). Therefore, the graphite cantilever beams are difficult to bend and easy to shear, and the isotropic continuum beam theory ($\alpha = 3$) cannot be applied.

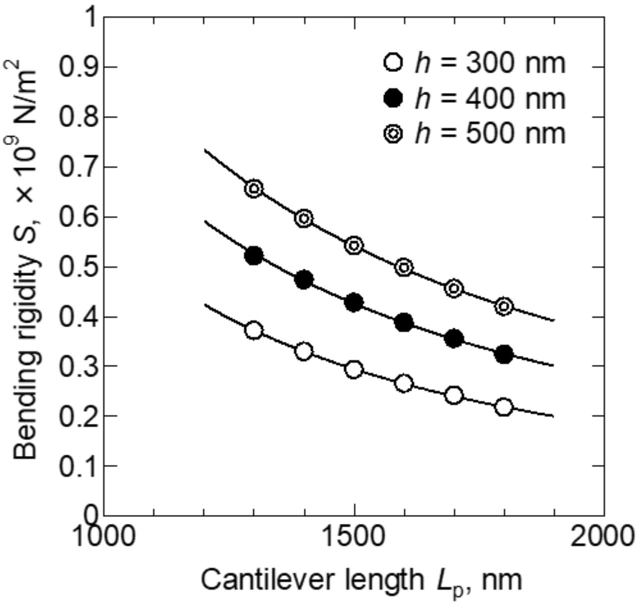

(a) Dependence on height and length

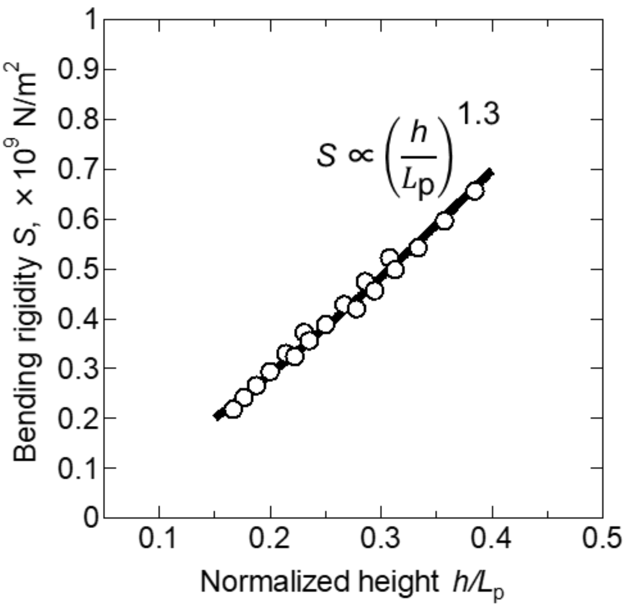

(b) Dependence on normalized height

Fig. S2-4: Effect of cantilever height and length on bending rigidity according to FEM analysis

S2.6.4 Effects of the presence of a-C layer

The effects of the amorphous carbon (a-C) layers on the upper and lower surfaces of the cantilever on the bending deformation were analyzed. The elastic properties of a-C are dependent on its structure, with the Young's modulus and Poisson's ratio ranging from 200 to 1000 GPa and 0.12 to 0.25, respectively [2]. For example, the Young's modulus of a 10-nm-thick layer of a-C has been experimentally estimated to be 211 GPa [3]. Although the mechanical properties of a-C produced by the current FIB processing method are unknown, we assumed it acts an isotropic elastic body with a Young's modulus of 300 GPa and Poisson's ratio of 0.2, and analyzed how it affected the bending deformation properties of the cantilever specimens by FEM. As shown in Fig. S2-5, a model with a 25-nm-thick a-C layer on the surface of the cantilever was created, and the same elastic analysis as that in Supplementary Material 2. 6. 1 was performed. Fig. S2-6(a) shows the relationship between the bending stiffness S and normalized height h/L_p. For comparison, the figure also shows the results without the a-C layer. In the small h/L_p region, where the bending contribution was large, S was approximately 6 % lower than that of the specimen without the a-C layer. In the large h/L_p region, where the shear contribution was large, S was a maximum of ~2% higher than that of the specimen without the a-C layer. In the middle region, the two effects canceled each other out, resulting in almost the same S value with and without the a-C layer. As a result, although the exponent of the S–(h/L_p) relationship slightly increased from α = ~1.3 to ~1.4, it was found that the existence of the a-C layer with a thickness of 25 nm had little effect on the deformation properties.

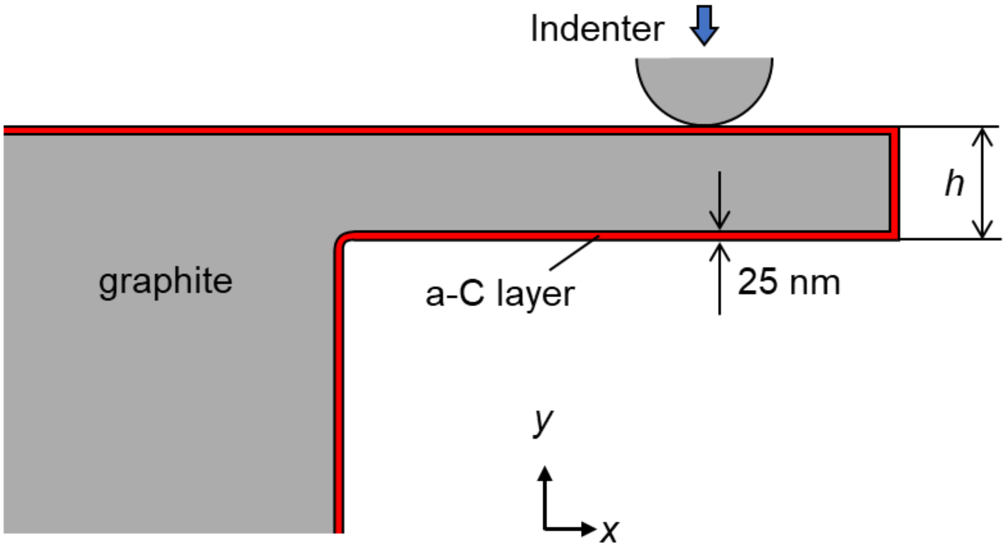

Fig. S2-5: FEM model of cantilever specimen with amorphous carbon (a-C) layer

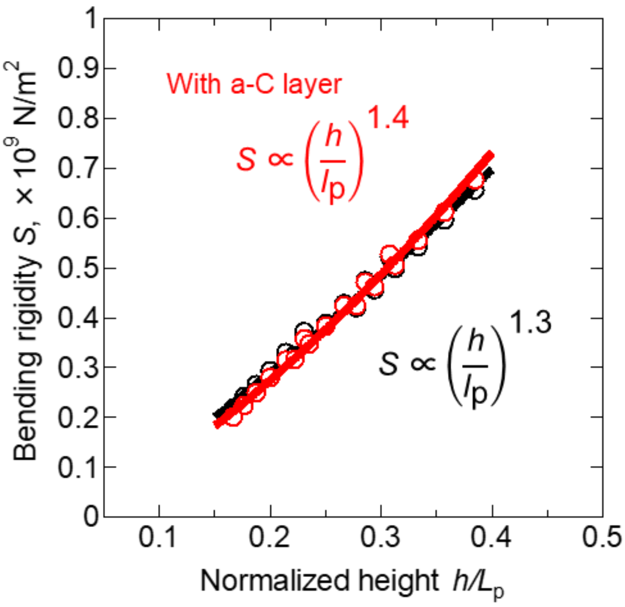

(a) Dependence on normalized height

Fig. S2-6: Effect of amorphous carbon (a-C) layer on the bending rigidity analyzed by FEM

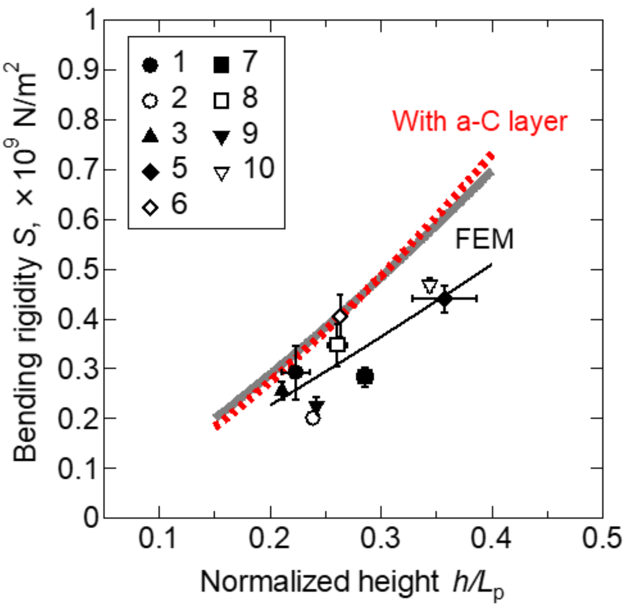

(b) Comparison with experimental results

Fig. S2-6: Continued.

S2.7 Effect of length on bending stiffness

To investigate the effect of L_p on the bending rigidity of the cantilever specimen, additional experiments with significantly different values of L_p (Specimen 10, h = 520 nm, L_p = ~1000, ~1700, and ~2500 nm) were performed. Fig. S2-7 presents the relationships between S and L_p obtained in the experiments. S decreased monotonically with increasing L_p, or proportionally to $L_p^{-1.5}$. In the figure, the estimation obtained from continuum FEM analysis (Fig. S2-4(a)) considering elastic anisotropy is represented by the dashed line. The analysis results are proportional to $L_p^{-1.4}$ and show almost the same tendency as the experimental results. Therefore, the initial stiffness was well reproduced by the anisotropic continuum analysis, including the case in which L_p changes significantly.

Ma et al. [4] conducted theoretical analysis of the ideal cylindrical bending of multilayer graphene and showed that the effective bending rigidity increases with increasing length and decreases with increasing curvature. The former tendency is the opposite of that observed in this study. The bending of the cantilever specimen in this study is different from pure cylindrical bending because both shear and bending stresses act on the cantilever. As the increase in length leads to increases in the bending moment and shear deformation, the rigidity tends to decrease. Therefore, the dependence on length is considered to be the opposite of the pure bending in the above study. On the other hand, the load–displacement relationship obtained in this study showed nonlinearity, in which the rigidity decreased as the deformation increased. It is considered that interlayer slip occurred and progressed as the deformation progressed and the rigidity decreased. These findings are qualitatively consistent with those of the theoretical analysis by Ma et al. [4].

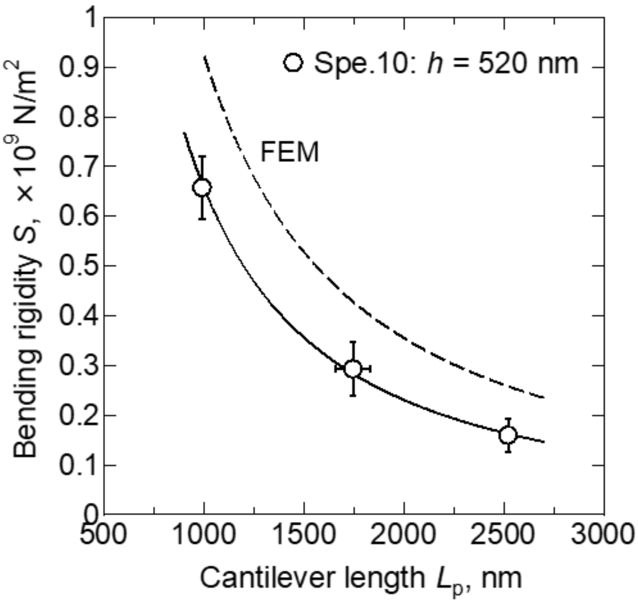

Fig. S2-7: Effect of cantilever length on bending rigidity

S2.8 Effect of electron-beam irradiation on bending properties

Figure S2-8 shows the results of a bending test performed under electron-beam irradiation at an accelerating voltage of 80 kV, where the effect of electron-beam irradiation was thought to be small. For comparison, the figure also shows the results obtained with an accelerating voltage of 200 kV. A typical normalized load–displacement relationship ((*P*/*w*)–*d*, Stage 2) showing nonlinearity, hysteresis, and recovery was obtained at both 80 and 200 kV, as shown in Fig. S2-8(a). Furthermore, as shown in Fig. S2-8(b), the initial stiffness *S* was in the same region at both 80 and 200 kV. From these results, it could be concluded that the electron-beam irradiation did not cause any significant structural changes in this specimen, and that the obtained mechanical properties reflect those of HOPG.

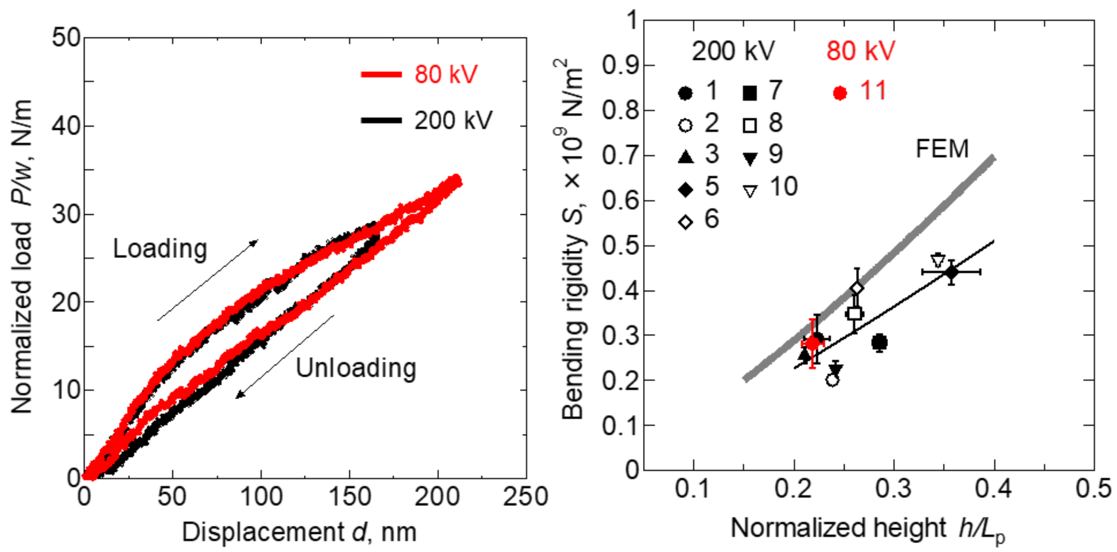

(a) Normalized load–displacement curves

(b) Bending stiffness as a function of normalized height

Fig. S2-8: Comparison of load–displacement (*P*–*d*) relationships and bending stiffness *S* under different accelerating voltages

S2.9 SEM analysis of deformed specimen

Fig. S2-9 shows SEM images of Specimen 4 after the bending experiments. Interestingly, even when the cantilever is deflected by θ_{max} = 62°, no distinct fracture is observed near the fixed end of the cantilever.

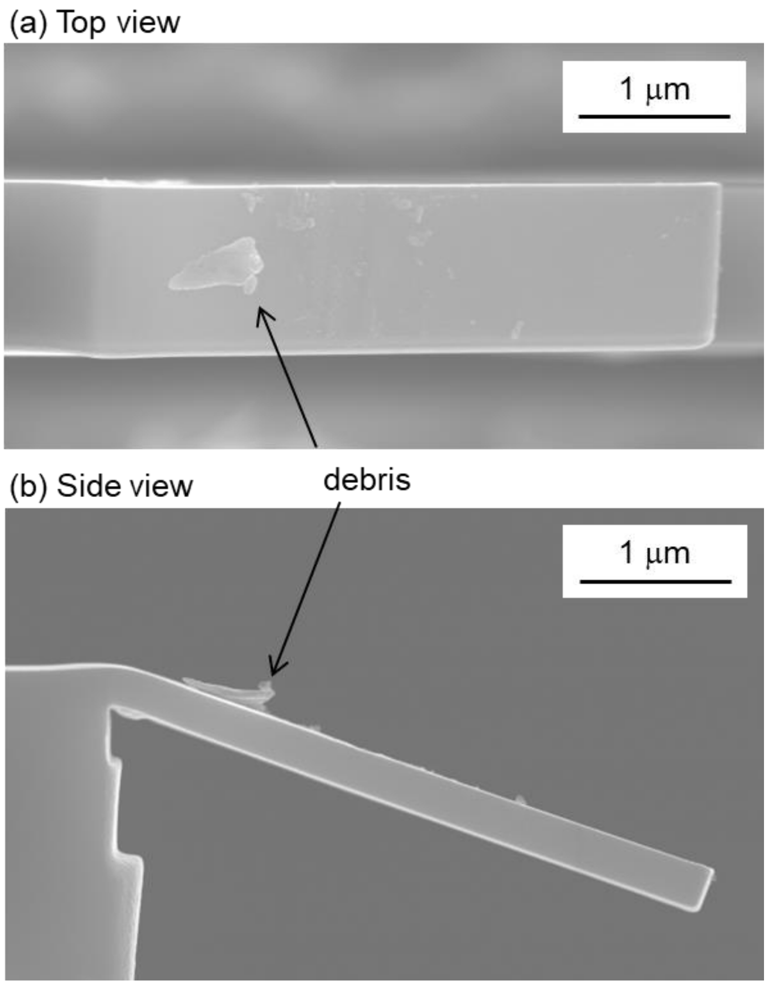

Fig. S2-9: SEM images of Specimen 4 after bending experiment

S2.10 FEM analysis of heat transfer in the cantilever specimen

As the electron beam irradiates the material, it penetrates into the sample while losing energy. The energy loss per electron can be estimated by the Bethe–Bloch equation [5, 6]:

$$-\frac{\mathrm{d}E}{\mathrm{d}x} = \frac{2\pi Z\rho(e^2/4\pi\epsilon_0)^2}{mv^2}\left\{\ln\left[\frac{E(E+mc^2)^2\beta^2}{2I_e^2 mc^2}\right] + (1-\beta^2) - \left(1-\sqrt{1-\beta^2}+\beta^2\right)\ln 2 + \frac{1}{8}\left(1-\sqrt{1-\beta^2}\right)^2\right\} \tag{S2-3}$$

where Z is the atomic number, r is the density, e is the electric charge, ϵ_0 is the dielectric constant, m is the electron mass, v is the velocity of the electron, c is the speed of light, $b = v/c$, E is the electron energy, and I_e is the mean excitation energy of the target material. The values listed in Table S2-5 were used. dE/dx per electron was estimated as 0.565 eV/nm or 9.06×10^{-11} J/m.

Table S2-5: Parameters used for estimating the temperature rise of the cantilever specimen

Z	r cm^{-3}	e C	ε_0 F/m	m kg	v at 200 keV m/s	c m/s	E keV	I_e eV
6	1.1257 $\times 10^{23}$	1.602 $\times 10^{-19}$	8.854 $\times 10^{-12}$	9.109 $\times 10^{-31}$	2.0845 $\times 10^{8}$	2.9979 $\times 10^{8}$	200	78

The irradiation current in the recovery period in the experiment on Specimen 4 was $I = 1.3 \times 10^3$ A/m^2. The volumetric heat flux H generated by the electron beam was calculated as 7.35×10^{11} J/sm^3 using the following equation [5].

$$H = \frac{I}{e}\frac{\mathrm{d}E}{\mathrm{d}x} \tag{S2-4}$$

The temperature rise due to this heat flux was calculated by thermal conduction analysis using FEM. The FEM software Abaqus 2017 was used for the analysis. The analysis model is shown in Fig. S2-10(a). The thermal conductivity of graphite has strongly anisotropy. Thermal conductivities of 1700 ± 100 W/mK in the in-plane direction and 8.0 ± 1.0 W/mK in the out-of-plane direction were used for the calculation [7]. The volumetric heat flux *H* was applied to the electron-beam irradiated region (radius 5 μm). The lower surface was fixed at room temperature (293 K) because it was fixed to the copper sample stage, which has a large heat capacity. Other boundaries were adiabatic conditions.

Fig. S2-10(b) shows the temperature distribution in the specimen. Owing to the anisotropic thermal conductivity, heat is transferred easily in the in-plane direction but poorly in the out-of-plane direction. As a result, the temperature was almost constant in the in-plane direction and a downward temperature gradient occurred. The maximum temperature rise in the specimen was estimated to be approximately 2.0 K. Thus, the temperature rise due to electron-beam irradiation was small, from which it was inferred that the deformation recovery was not due to heat.

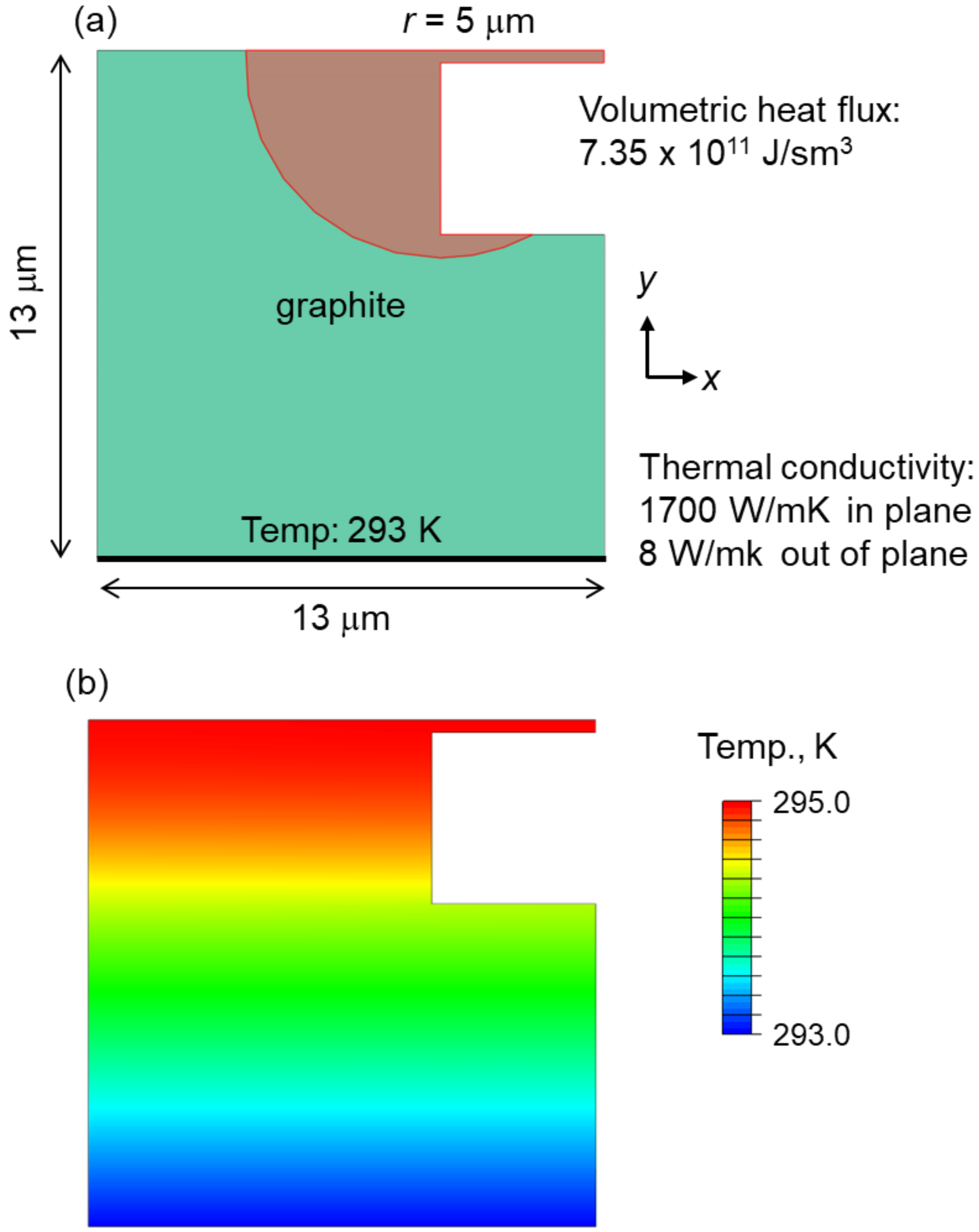

Fig. S2-10: FEM analysis of heat distribution in graphite specimen owing to electron-beam irradiation

References

[1] Hysitron, PI 95 TEM PicoIndenter User Manual Revision 9.2.1211(2011).

[2] R. Jana, D. Savio, V. L. Deringer, L. Pastewka, Structural and elastic properties of amorphous carbon from simulated quenching at low rates, *Model Simul. Mater. Sc.* **27**, 085009 (2019).

[3] J. W. Suk, S. Murali, J. An, R. S. Ruoff, Mechanical measurements of ultra-thin amorphous carbon membranes using scanning atomic force microscopy, *Carbon* **50**, 2220 (2012).

[4] X. J. Ma, L. Q. Liu, Z. Zhang, Y. G. Wei, A method to determine the geometry-dependent bending stiffness of multilayer graphene sheets, *J. Appl*. Mech. **88**, 011004 (2021).

[5] S. B. Fisher, On the temperature rise in electron irradiated foils, *Radiation Effects* 5, 239 (1970).

[6] I. Jencic, M. W. Bench, I. M. Robertson, M. A. Kirk, Electron-beam-induced crystallization of isolated amorphous regions in Si, Ge, Gap, and Gaas, *J. Appl. Phys*. 78, 974 (1995).

[7] Optigraph, 2011. http://www.optigraph.eu/basics.html.

Supplementary Materials on Chapter 3

S3.1 Cantilever bending experiment for $MoTe_2$

a. Experimental method

The cantilever specimens were processed from bulk material using a focused ion beam system (FB2200, Hitachi High-Tech Co.). The dimensions of the micro $MoTe_2$ specimens are shown in Table S3-1. The SEM images of Specimens OS-I and OS-II are shown in Figs. S3-1(a) and (b) Here, w is the width of specimen, h is the height of specimen, L is the length of specimen, and L_p is the distance between the fixed end and the loading point, as shown in Fig. 2-1(a). A load P was applied with a diamond indenter in the stacking direction. A displacement-controlled loading-unloading tests were performed. Multiple loading tests were conducted on each specimen by increasing the maximum displacement d_{max}. The tests for $MoTe_2$ were performed using a micromechanical testing device (Unisoku Co., Ltd.) driven by a piezo actuator under *in situ* scanning electron microscopy (Thermo Fisher Scientific, Scios2) observation. The displacement rate of the indenter was approximately 11 nm/s. Five tests (OS-I1–OS-I5) were performed on Specimen OS-I.

b. Experimental results

Figures S3-1(c) and (d) show the P–d relationship and SEM images in Test OS-I2, respectively. P increased linearly with an increase in d, and P rapidly dropped twice at Points B: d = 11.4 μm and D: d = 13.2 μm. From the SEM image at Point E, localized interlayer damage was observed in the specimen fixed section at B→C, and at D→E, localized interlayer slip with the appearance of a new surface at the free end of the cantilever beam was observed. After unloading, plastic deformation corresponding to d =

4.0 μm remained.

Tests OS-I3–OS-I5 exhibited qualitatively similar behaviors. In these tests, discrete interlayer slip occurred and progressed sequentially as the deformation progressed. In Test OS-I5, in-plane fracture of the 2D material did not occur even when deformed to d = 20 μm (Fig. S3-1(e)). As shown in the SEM image after the test (Fig. S3-1(f)), a localized interlayer slip was confirmed not only at the cantilever beam but also inside the fixed end (right side of the figure). The results for Specimen OS-II were qualitatively similar.

Table S3-1: Dimensions of $MoTe_2$ cantilever specimens

Specimen No.	w, μm	h, μm	L, μm	L_p, μm
OS-I	7.6	4.5	36.4	32.0
OS-II	6.1	6.8	36.6	34.0

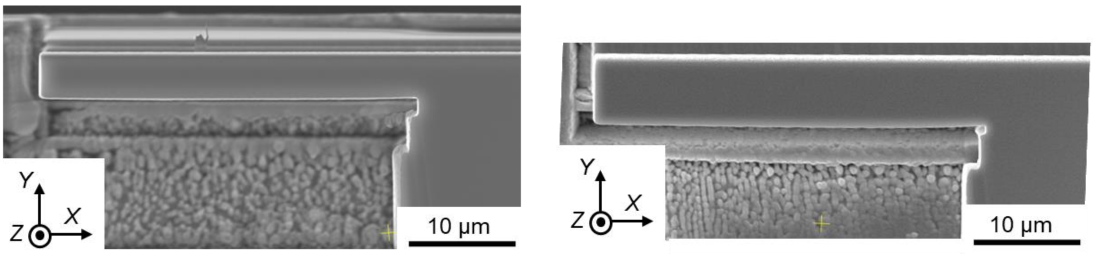

(a) SEM image of Specimen OS-I (b) SEM image of Specimen OS-II

Fig. S3-1: Results of bending experiment of $MoTe_2$

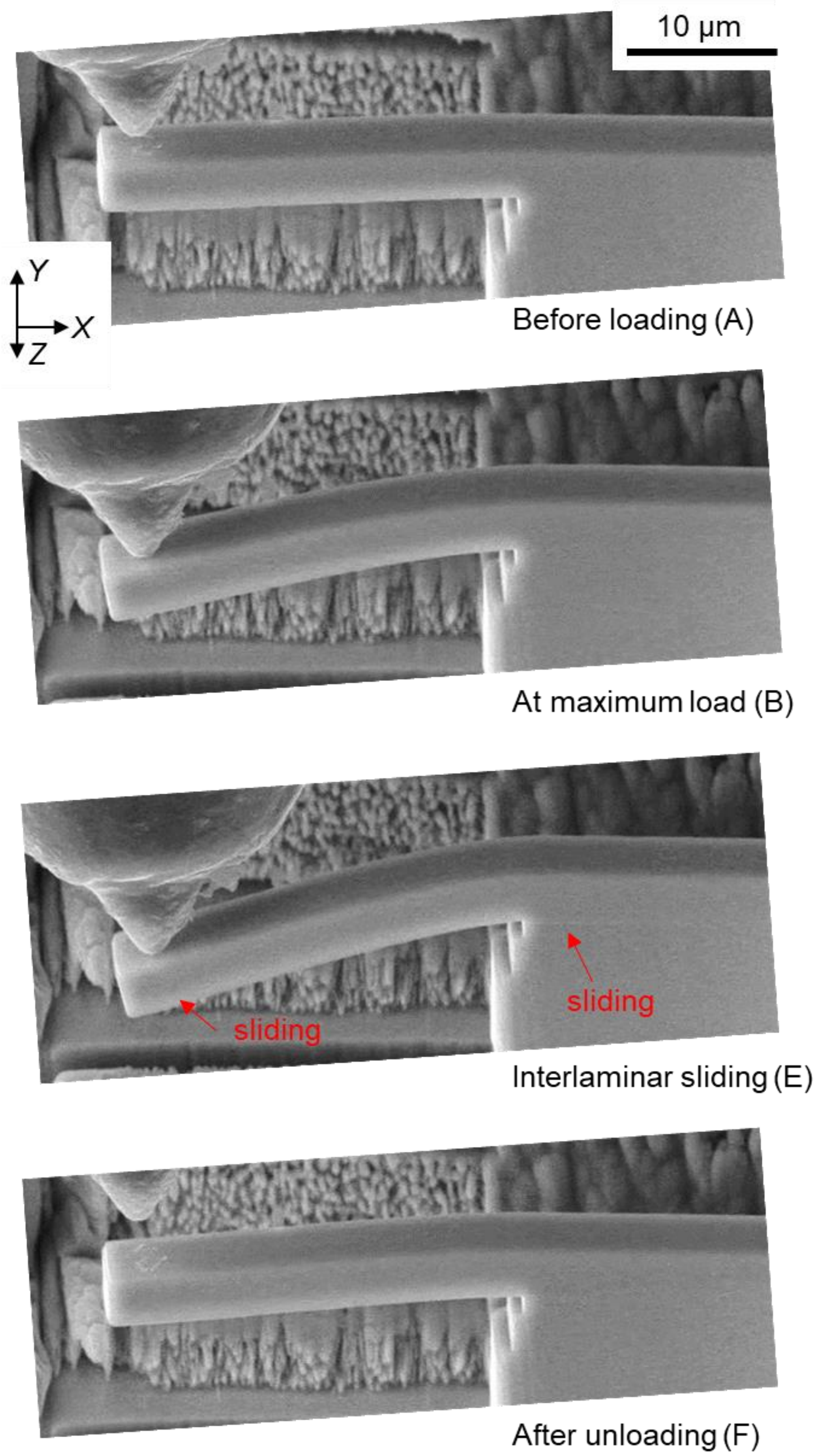

(d) SEM images in test OS-I2

Fig. S3-1: Continued.

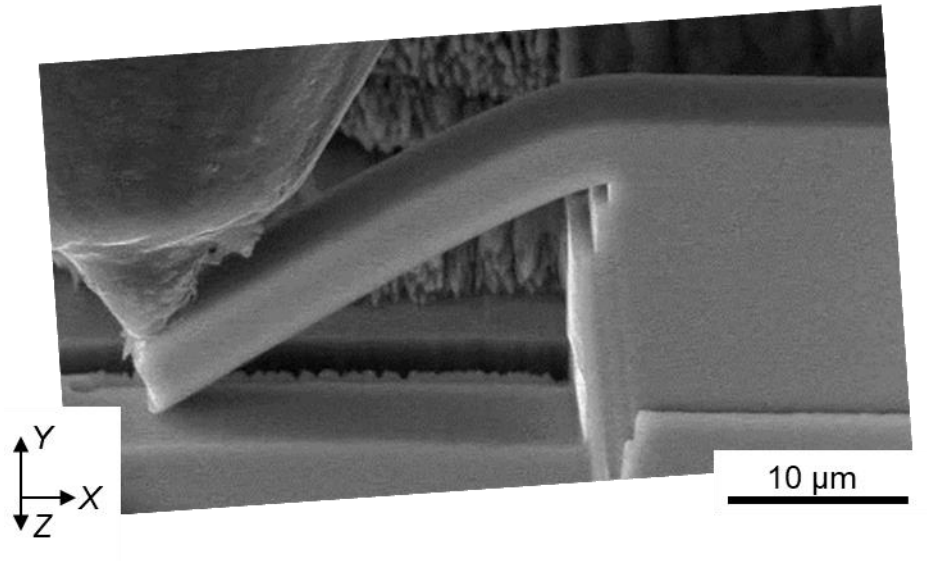

(e) SEM image of specimen in test OS-I5

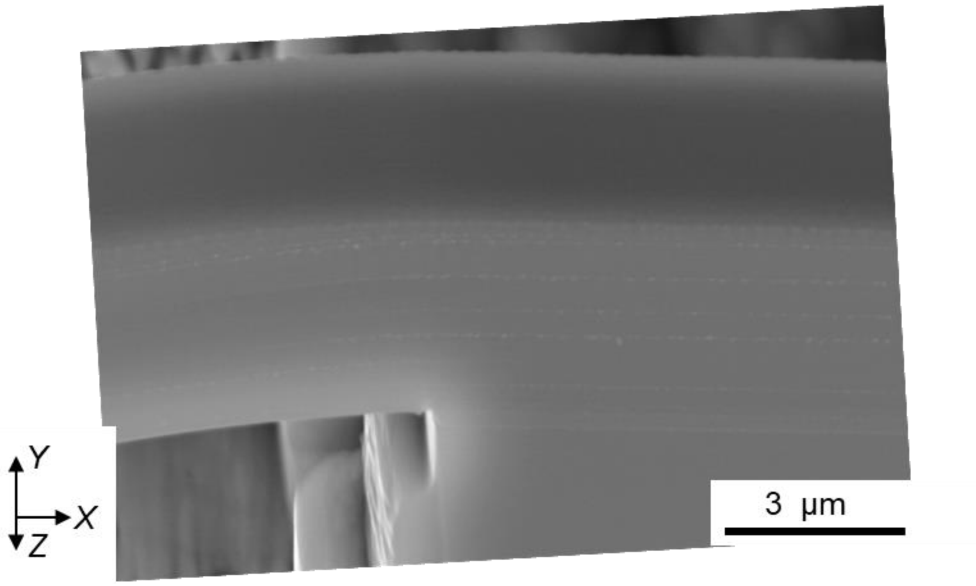

(f) SEM image of specimen after test OS-I5

Fig. S3-1: Continued.

S3.2 Constitutive equation of unloading process

Fig. S3-2 shows the constitutive equation for the unloading process of the recombination model, indicated by the red line. Different paths are followed depending on δ_T at the start of unloading. Fig. S3-2(a) shows the case where the unloading is started in the process of increasing τ_T. As δ_T decreases, τ_T decreases linearly with the same slope as the loading process up to point A in the figure ($\tau_T = 0$). It then follows the same constitutive equation as the loading process. However, the sign of τ_T becomes negative because the slip occurs in the opposite direction to the loading process.

Fig. S3-2(b) shows the case where the unloading is started in the decreasing process of τ_T. As δ_T decreases, τ_T decreases linearly on the line connecting the unloading start point S and point A ($\tau_T = 0$). After point A, the magnitude of τ_T increases with the same slope and reaches a maximum at point B (the same magnitude as τ_T in S). As δ_T decreases further, the magnitude of τ_T begins to decrease and thereafter follows the same constitutive equation as the loading process.

In the constitutive equation for the unloading process of the fracture model, after the fracture has occurred, $\delta_T > \delta_{Tm}$, $\tau_T = 0$ MPa at all values. When the unloading is done by the increasing process of τ_T, $\delta_T < \delta_{Tm}/2$, before the fracture occurs, $\delta_T < \delta_{Tm}$, as shown in Fig. S3-2(a), τ_T decreases linearly with the same slope as the loading process up to the origin, and then follows the same constitutive equation as the loading process. If the unloading is started in the decreasing process of τ_T, $\delta_{Tm}/2 < \delta_T < \delta_{Tm}$, the constitutive equation follows the same path as the SABC shown in Fig. S3-2(b).

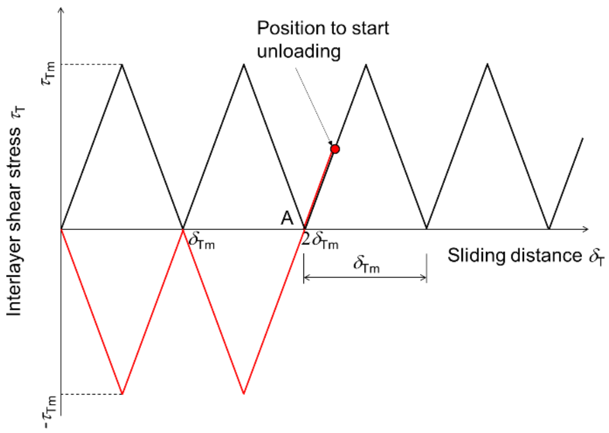

(a) Unloading at a point in the process of increasing τ_T

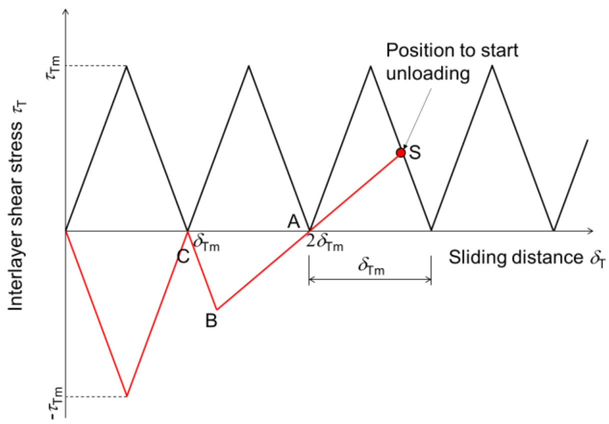

(b) Unloading at a point in the process of decreasing τ_T

Fig. S3-2: CZM in unloading process

S3.3 Method for non-linear FEM analysis

The Newton-Raphson method (line search method) was used as the analytical method for nonlinear analysis using the FEM with a maximum number of equilibrium iterations per sub-step of 20. A linear analysis was performed applying the full load F_a at a certain time step and the displacement x_1 was calculated $F_a = Kx_1$, where K is the stiffness matrix. Based on the obtained x_1, the sum of the internal forces F_1 is calculated, and when (F_a-

F_1) becomes less than the convergence criterion, the next sub-step is performed. The L2 norm of F_a multiplied by 0.5 % as a tolerance was used as the criterion for determining convergence. The loading and unloading processes were each divided into 10,000 sub-steps, and when a convergent solution could not be obtained in a sub-step, the sub-step was further subdivided into up to 10^7 sub-steps. In this paper, we show the solutions that were determined to be convergent under these conditions.

S3.4 τ_T distributions during the unloading process at τ_{Tm} = 300 MPa

Fig. S3-3 shows the τ_T distributions during the unloading process at τ_{Tm} = 300 MPa using the semi-discrete layer model (CZM: recombination model, N = 3, h_n = 0.110 μm). The τ_T distribution of cantilever was qualitatively similar to that at τ_{Tm} = 100 MPa. The interlayer delamination (τ_T = 0) appeared and extended as d decreased. The delaminated regions were confined into smaller regions compared with those at τ_{Tm} = 100 MPa.

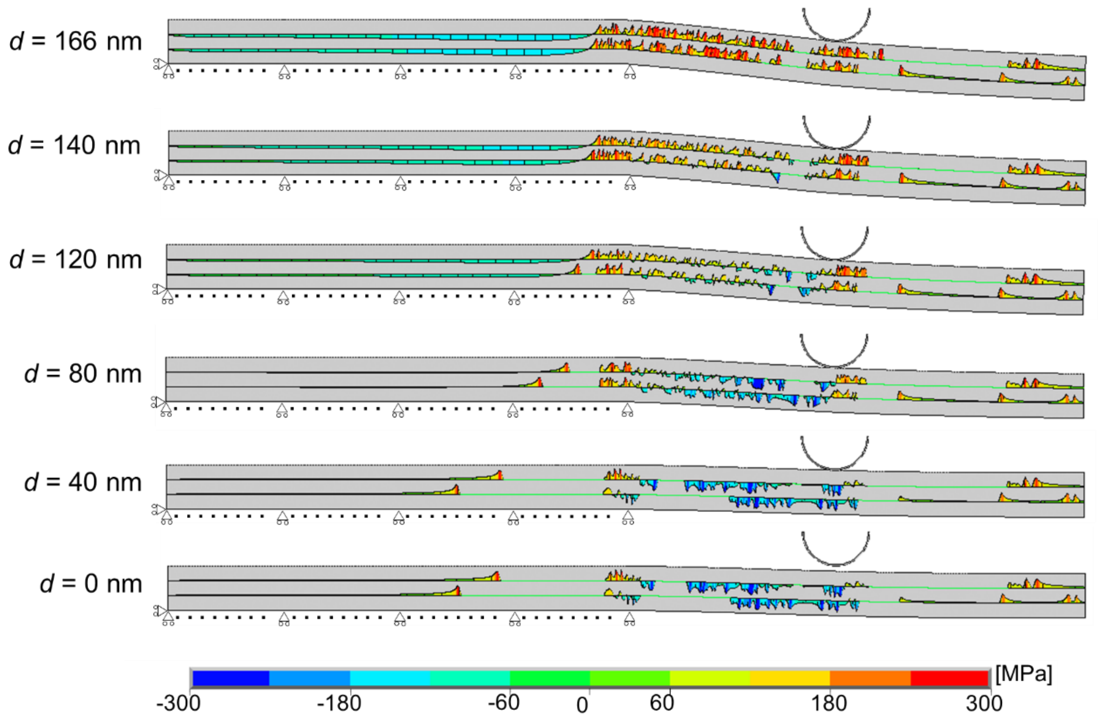

Fig. S3-3: Change in τ_T distribution in the unloading process: recombination model, N = 3, h_n = 0.11 μm, τ_{Tm} = 300 MPa

S3.5 τ_T distributions during the loading process of h_n = 0.055 μm (N = 6) and h_n = 0.030 μm (N = 11)

Figs. S3-4(a) and (b) show the τ_T distributions in the loading processes analyzed using the semi-discrete layer model (CZM: recombination model, τ_{Tm} = 100 MPa, h = 0.33 μm, and d_{max} = 166 nm) with h_n = 0.055 μm (N = 6) and h_n = 0.030 μm (N = 11).

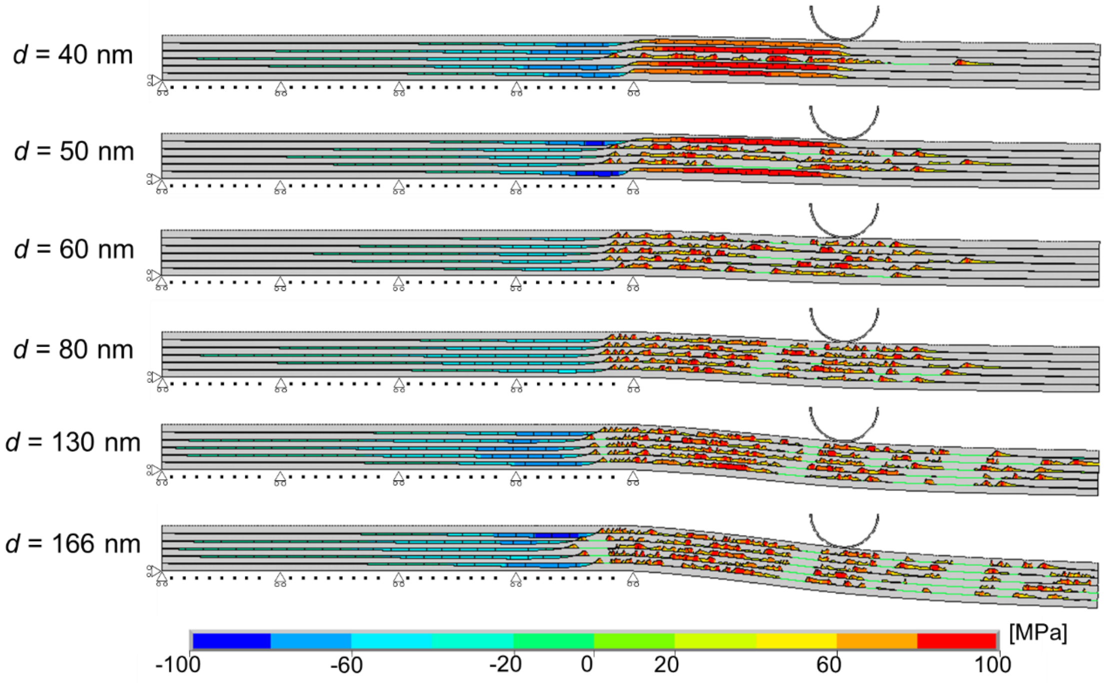

(a) $N = 6$, $h_n = 0.055$ μm

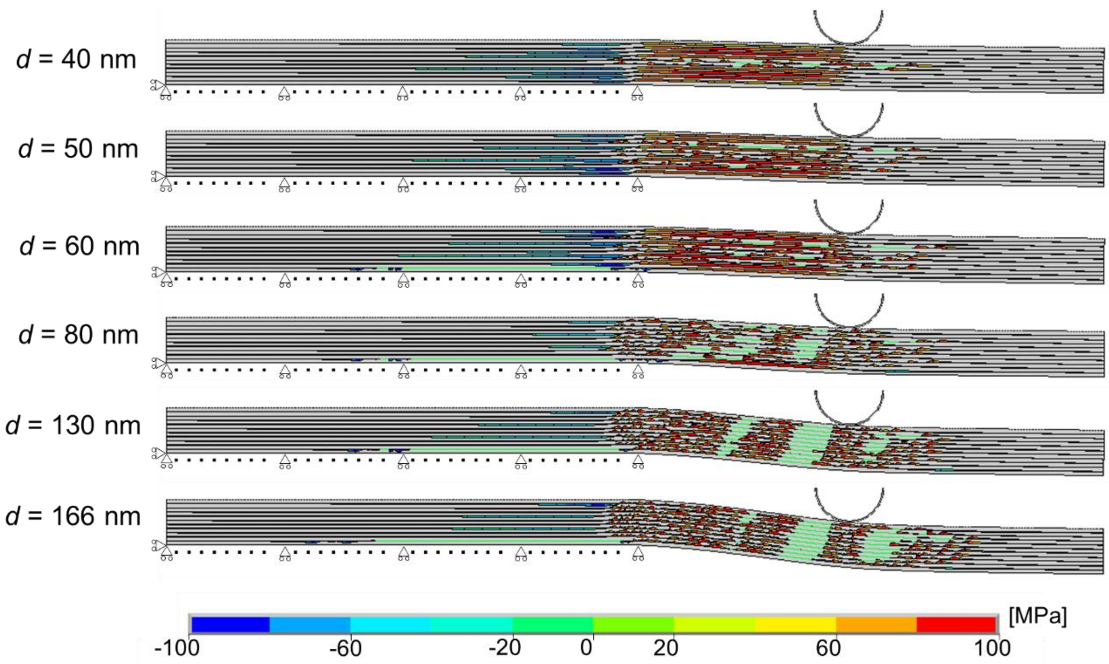

(b) $N = 11$, $h_n = 0.030$ μm

Fig. S3-4: Change in the distribution of τ_T in the loading processes: recombination model, $\tau_{Tm} = 100$ MPa

S3.6 Result of the recombination model for the $MoTe_2$ cantilever

Fig. S3-5 shows the results of a semi-discrete layer model (CZM: recombination model, $N = 10$, $h_n = 0.45$ μm, $\tau_{Tm} = 200$ MPa, $\delta_{Tm} = 25$ nm) for a micro $MoTe_2$ cantilever. The recombination model showed a qualitatively similar result to the fracture model shown in Fig. 3-9(a). In the loading process, P increases linearly with increasing d, followed by two rapid drops in P. During the unloading process, P decreased linearly with decreasing d, and a small amount of plastic deformation remained. These were consistent with the characteristic behavior of the experiment. However, the recombination model showed a large quantitative deviation from the experimental result in terms of higher initial stiffness, smaller sharp decrease in load, and closer slope of the loading and unloading curves. The fracture model, on the other hand, reproduced these features well and was therefore judged to be a more valid model.

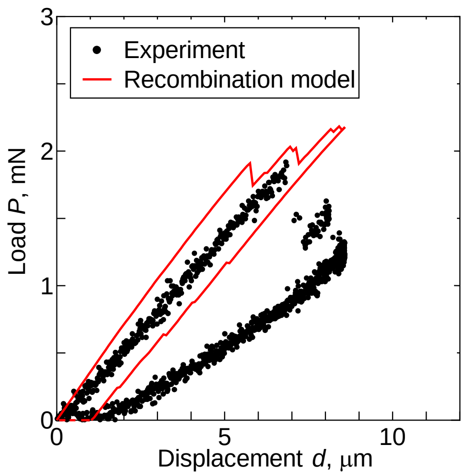

Fig. S3-5: Result of the recombination model for $MoTe_2$ cantilever

S3.7 Theoretical models

a. Timoshenko beam model [1]

The effective bending stiffness by the Timoshenko beam model is express by the following equation.

$$D_{\mathrm{eff}} = L_{\mathrm{p}}^3 \left(\frac{L_{\mathrm{p}}^3}{EI} + \frac{3\alpha L_{\mathrm{p}}}{GA} \right)^{-1} \qquad \text{(S3-1)}$$

L_{p} is the distance between fixed end to the loading point of cantilever, E is the in-plane Young's modulus of graphite (1010 GPa [2]), I is the moment of inertia, G is the interlayer shear modulus (2.66 GPa [3]), A is the cross-sectional area, and α is the coefficient depending on the cross-sectional shape, and is 1.5 for a rectangular cross-section.

b. Centerline-based stacked model [3]

The effective bending stiffness by the centerline-based stacked model is expressed by the following equation.

$$D_{\mathrm{eff}} = \frac{N^3 Eth^2}{96} \left\{ \sum_{m=1}^{\infty} \left[\frac{\lambda \mu^2 k^2}{N^2} a_m^4 - \frac{2 a_m k^3 \tanh\left(\frac{a_m (N-1)}{2k}\right)}{N^3 \left\{ 1 + \frac{a_m}{k} \tanh\left(\frac{a_m (N-1)}{2k}\right) \right\}} + \frac{a_m^2 (N-1)}{N} \frac{k^2}{N^2} \right]^{-1} \right\}^{-1} \qquad \text{(S3-2)}$$

L_{p} is the distance between the fulcrum and the loading point of the 3-point bending simply supported beam, E is the in-plane Young's modulus of single layer (1010 GPa [2]), G is the interlayer shear modulus (2.66 GPa [3]), t is the thickness of single layer (interlayer distance, 0.3365 nm), B_0 is the monolayer bending stiffness (1.8 eV [3]). $a_m = (2m-1)\pi$, λ, μ, and k are the dimensionless numbers defined below.

$$\lambda = L_{\mathrm{p}} / t \quad , \quad \mu = \frac{\sqrt{\frac{B_0}{G L_{\mathrm{p}}}}}{L_{\mathrm{p}}}, \quad k = \frac{L_{\mathrm{p}}}{\sqrt{\frac{Et^2}{G}}} \qquad \text{(S3-3)}$$

References

[1] S. P. Timoshenko, *Philosophical Magazine* **41**, 744 (1921).

[2] C. Lee, X. D. Wei, J. W. Kysar, and J. Hone, Measurement of the Elastic Properties and Intrinsic Strength of Monolayer Graphene, *Science* **321**, 385 (2008).

[3] Z. C. Huang, Z. Z. He, Y. B. Zhu, and H. A. Wu, A general theory for the bending of multilayer van der Waals materials, *Journal of the Mechanics and Physics of Solids* **171**, 105144 (2023).

Supplementary materials on Chapter 4

4.1 Fabrication procedure of in-plane fracture toughness specimens

The FIB procedure is shown in Fig. S4-1. As an in-plane crack fracture toughness specimen of vdW-layered material $MoTe_2$, a cantilever-type chevron-notched specimen was prepared such that the *XY* plane in the figure is the surface of the 2D material. An FIB system (Hitachi High-Tech Corp., FB2200) was used to process the specimen. Using a Ga+ ion beam, the acceleration voltage was set to 40 kV.

1) The irradiation current of the FIB was 20.7 nA. By irradiating from the *Z* direction, a prismatic block of approximately 25 mm × 15 mm was machined while leaving the arrowed section in Fig. S4-1(a). The stage was rotated 60° around the *Y*-axis, and the material was milled through the red line in Fig. S4-1(a) until it penetrated the back. Subsequently, the stage rotated around the *Y*-axis back to 0°. Next, the FIB was irradiated from the *Z* direction with an irradiation current of 4.18 nA, and the tip of the probe for pickup was fixed to the block portion with tungsten by the ion beam-induced deposition method. Then, the material was cut along the yellow line in the figure to separate the block from the bulk material. Finally, the probe was lifted in the *Z* direction, and the block was picked up.

2) The block was placed on the upper surface of the sample stage, FIB was irradiated from the *Z* and -*Z* directions with an irradiation current of 3.91 nA, and tungsten was deposited and fixed on the front and back sections using the ion beam-induced deposition method (Fig. S4-1(b)). Subsequently, the probe was separated using FIB.

3) With an irradiation current of 0.84 nA, the FIB was irradiated from the *Z* direction, and

the block was cut to the desired specimen width (Fig. S4-1(c)).

4) The FIB was irradiated from the Y direction to process the specimen in the thickness direction. The plate was processed with an irradiation current of 0.12 nA, and the irradiation current was changed to 0.01 nA for finishing in the thickness direction (Fig. S4-1(d)). Because the machined surface was tilted owing to the flare angle of the FIB, the stage was tilted by ±1.2° around the X-axis to make the thickness uniform.

5) The FIB was irradiated from the Z direction to finish the cantilever shape. The irradiation current was 0.01 nA, and the stage was tilted ±1.2° around the X-axis for machining so that the height of the beam became uniform (Fig. S4-1(e)).

6) The FIB was irradiated from the Y direction to machine the chevron notch. The chevron notch was machined by tilting the stage ±15° around the X-axis with an irradiation current of 0.01 nA. Owing to the influence of the flare angle, the chevron notch angle was approximately $\theta = 34°$ (Fig. S4-1(f)).

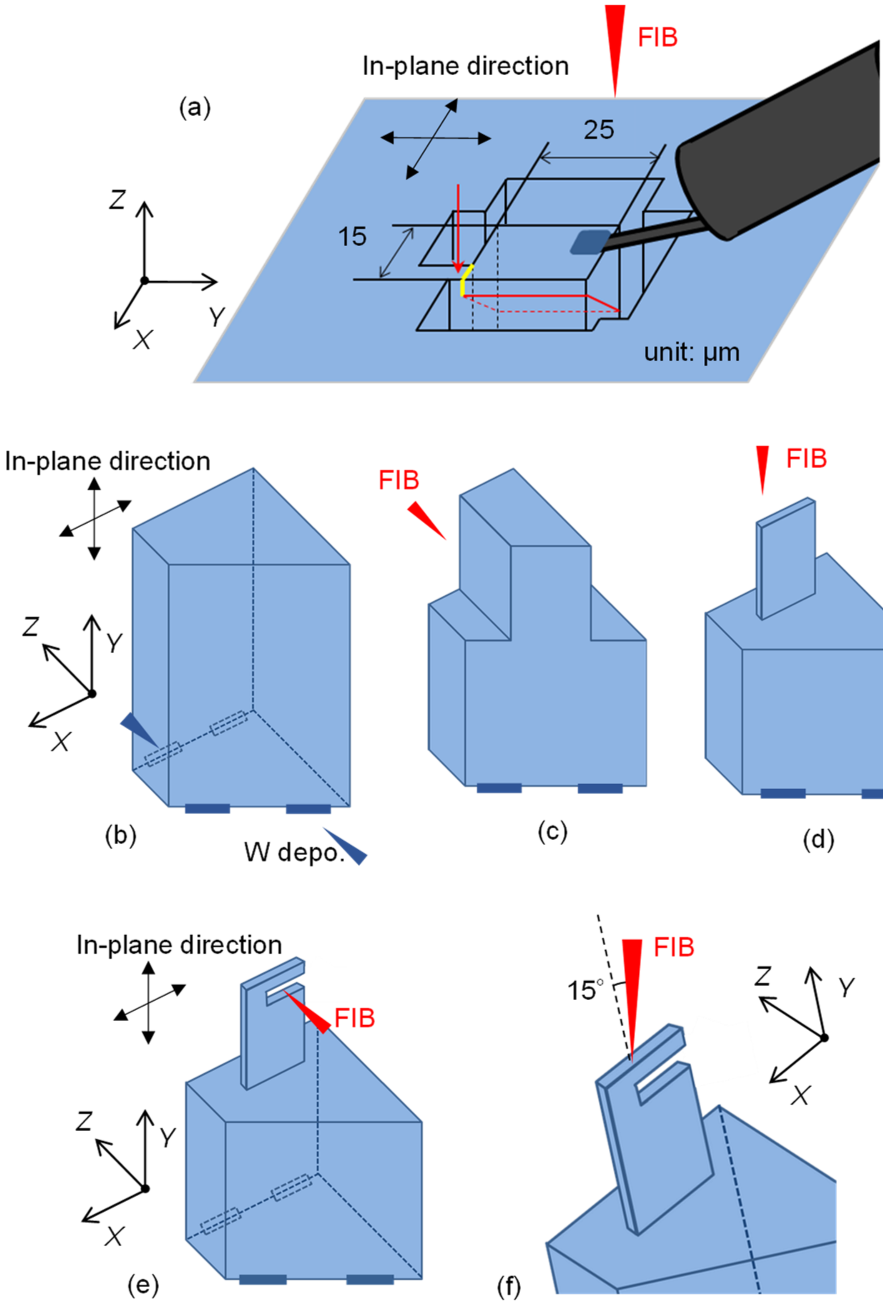

Fig. S4-1: FIB processing procedure of specimens for in-plane crack fracture toughness tests

4.2 SEM micrographs of in-plane fracture toughness specimens

Figures S4-2(a) and (b) show the SEM images of Specimens ISB and IL, respectively.

(a) Specimen ISB

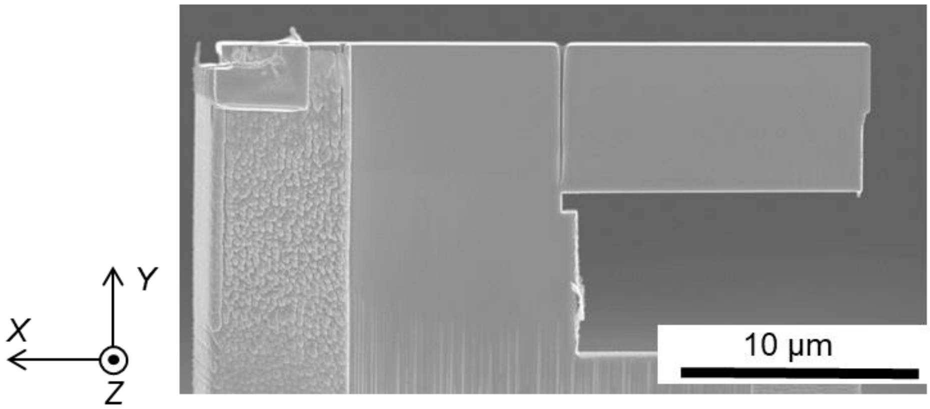

(b) Specimen IL

Fig. S4-2: SEM images of in-plane crack fracture toughness specimens

4.3 Fabrication procedure of out-of-plane fracture toughness specimens

The FIB procedure is shown in Fig. S4-3. For the out-of-plane crack fracture toughness specimen of vdW-layered material $MoTe_2$, a cantilever-type notched specimen was prepared such that the *XZ* plane in the figure was the surface of the 2D material. An FIB system (Thermo Fisher Scientific, Scios 2) was used to process the specimen. Using a Ga+ ion beam, the acceleration voltage was set to 30 kV.

1) The FIB was irradiated from the *Y* direction and the shaded area in Fig. S4-3(a) was milled. After milling a wide area around the specimen with an irradiation current of 50 nA, processing was performed while gradually reducing the irradiation current to 5.0 nA.

2) The FIB was irradiated in the *Z* direction with an irradiation current of 5.0 nA, and the shaded area in Fig. S4-3(b) was milled to form a cantilever shape. Because the machined surface was tilted owing to the flare angle of the FIB, when processing the top and bottom of the cantilever beam, the stage was tilted ±2.0° around the *Y*-axis to ensure a uniform thickness.

3) As shown in Fig. S4-3(c), the surface of the specimen was finished by irradiating from the *Y* direction with an irradiation current of 1.0 nA. The stage was tilted ±2.0° around the *X*-axis for machining so that the width of the beam became uniform.

4) As shown in Fig. S4-3(d), the notch was machined by irradiating in the *Z* direction with an irradiation current of 0.1 nA. By inclining the stage 2.0° around the *X*-axis, the notch length was kept constant in the width direction.

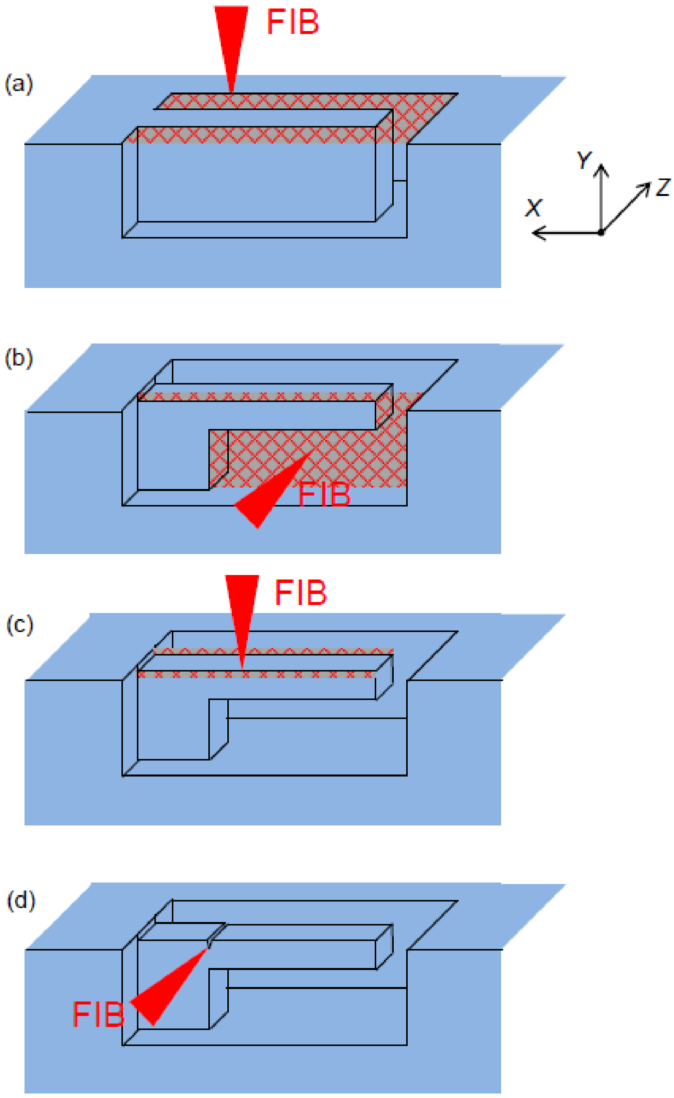

Fig. S4-3: FIB processing procedure of specimens for out-of-plane crack fracture toughness tests

4.4 SEM micrographs of out-of-plane fracture toughness specimens

Figures S4-4(a) and (b) show the SEM images of Specimens OA and OB, respectively.

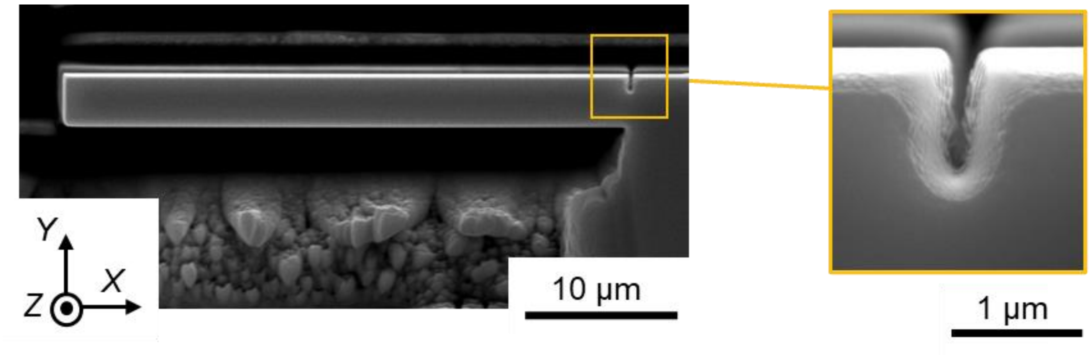

(a) Specimen OA

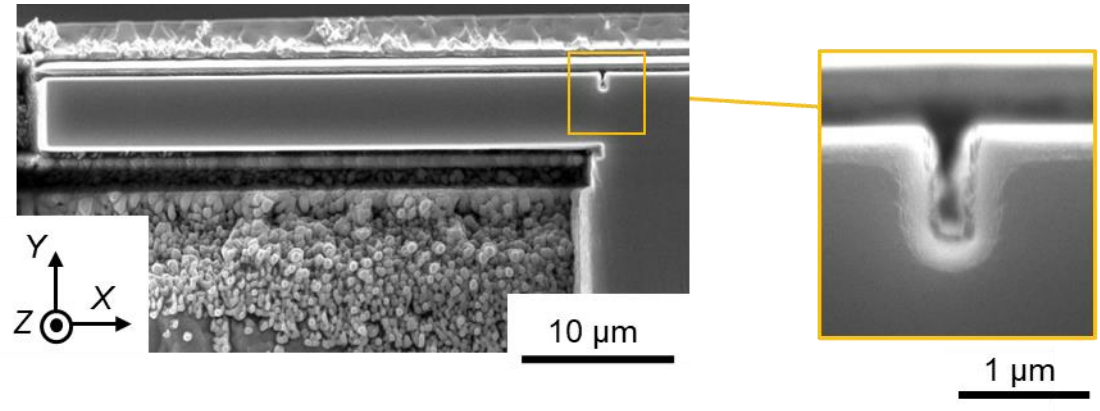

(b) Specimen OB

Fig. S4-4: SEM images of specimens for out-of-plane crack fracture toughness test using notched cantilever specimen

4.5 FEM model of out-of-plane and delamination cracks

Figure S4-5 shows the FEM model for Specimen OA.

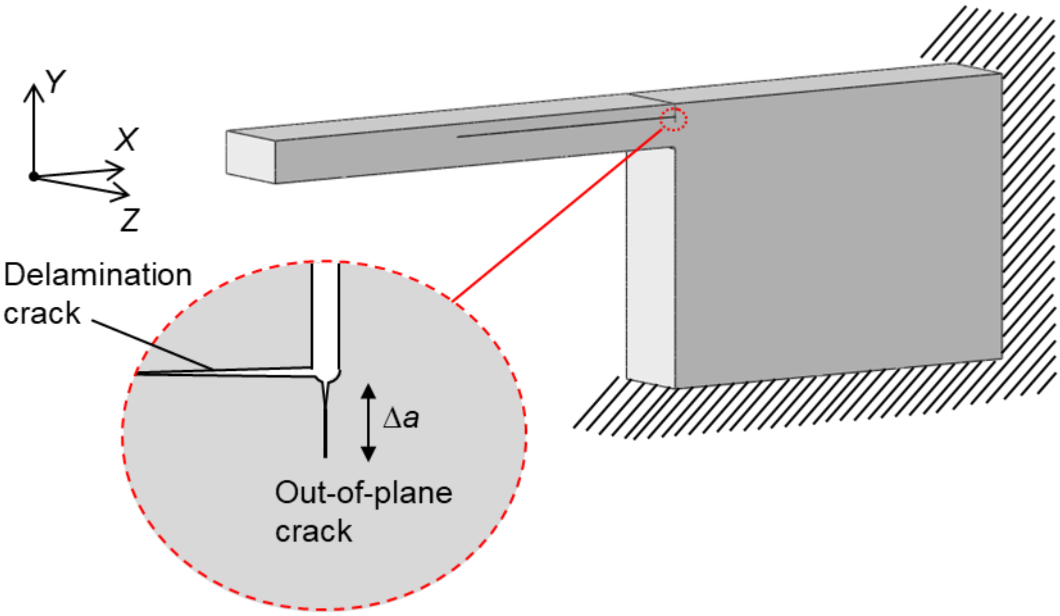

Fig. S4-5: FEM model of out-of-plane and delamination cracks (Specimen OA)

4.6 Determination of material constants in the CZM

The CZM parameters τ_{Tm} and δ_{Tm} in the discrete model shown in Fig. 3-2(b) were determined to reproduce the deformation behaviors of both smooth specimens (Specimens OS-I and OS-II) with different dimensions. Figure S4-6(a) shows the analytical model. The height, h_{n}, of the continuum layer was set to 450 nm. FEM software (ANSYS) was used for the analysis. Assuming plane strain, a triangular 6-node quadratic element was used as the element. The loading-unloading deformation of one cycle was analyzed by applying a displacement to the loading point. Parametric analysis with different τ_{Tm} and δ_{Tm} was performed to estimate the parameters that best fit the two experimental results. Figures S4-6 (b) and (c) show the load P – displacement d relationship for τ_{Tm} = 250 MPa and δ_{Tm} = 30 nm. P increased linearly with increasing d, then the slope decreased accompanied by intermittent decreases in P. When P decreased rapidly, interlayer slip occurred. During unloading, P decreased almost linearly. These behaviors were in good agreement with the experimental results. From this analysis, the CZM parameters in the semi-discrete layer model for this material were determined to be τ_{Tm} = 250 MPa and δ_{Tm} = 30 nm.

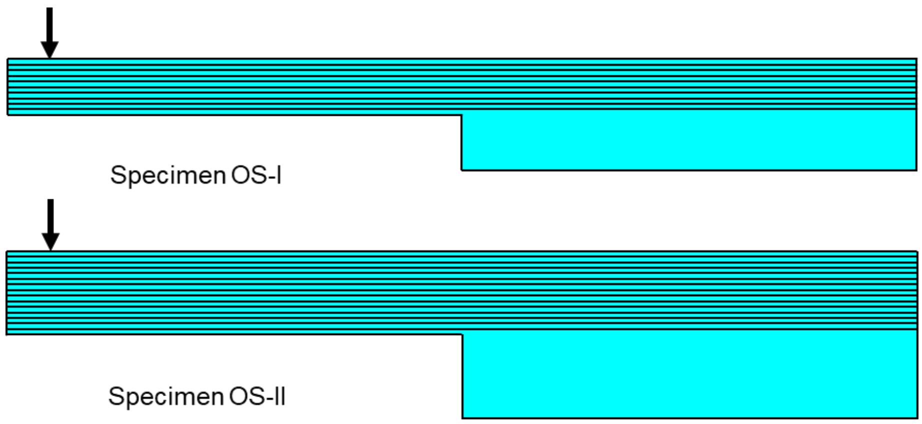

(a) Analytical model

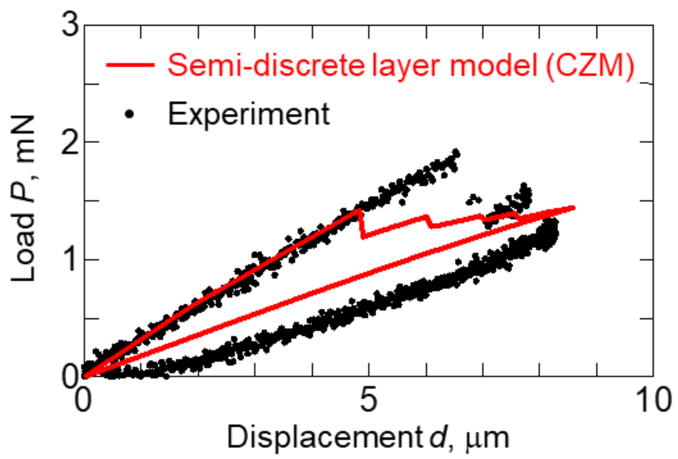

(b) Relationship between load P and displacement d of Test OS-I

Fig. S4-6: Comparison of deformation curve between the semi-discrete layer model and experiment (Specimens OS-I and OS-II)

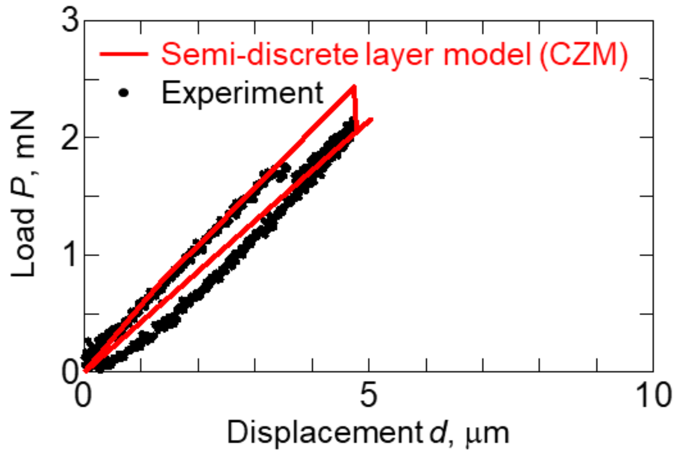

(c) Relationship between load P and displacement d of Test OS-II

Fig. S4-6: Continued.

4.7 Shear stress distribution in continuum and discrete models for Specimen OC

Figures S4-7 shows the results of the continuum analysis and the discrete model analysis using CZM for Specimen OC (Test OC2). The figures show the deformation and the distribution of shear stress τ_{xy} at the critical load P_C. In the continuum model, a singular stress field was generated at the crack tip, whereas in the discrete model, the crack tip was blunted by interlayer slip originating at the crack tip and τ_{xy} was released at the blunted crack tip.

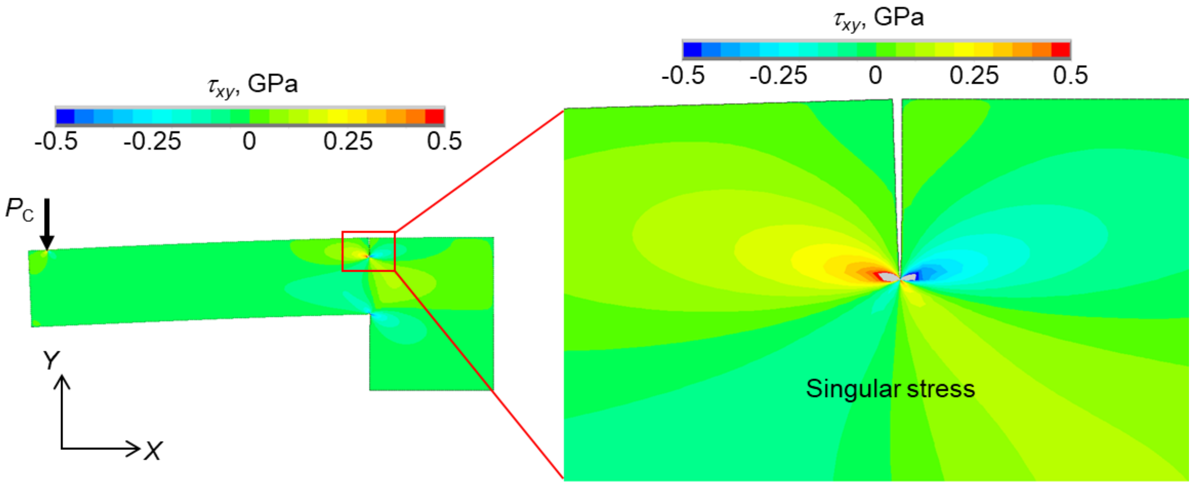

(a) Deformation and stress distribution in continuum model

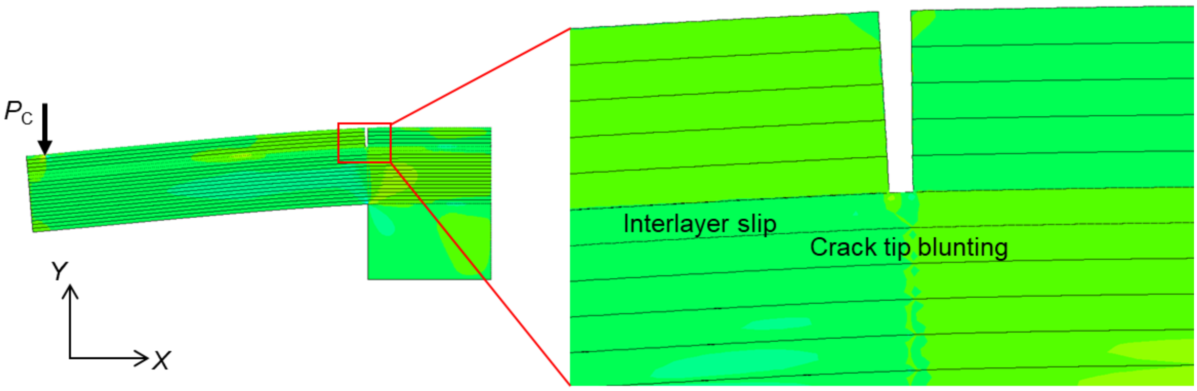

(b) Deformation and stress distribution in semi-discrete layer model

Fig. S4-7: Deformation and shear stress distributions in the continuum model and semi-discrete layer model for Specimen OC

List of Publications

Related to this dissertation

Full Length Papers

1. M. Akiyoshi, S. Koike, T. Shimada, and H. Hirakata, Bending deformation and self-restoration of submicron-sized graphite cantilevers, *Acta Mater*. **241**, 118381 (2022).
2. H. Hirakata, M. Akiyoshi, R. Masuda, and T. Shimada, High fracture toughness in van der Waals-layered $MoTe_2$: Disappearance of stress singularity, *Eng*. *Fract*. *Mech*. **277**, 108974 (2023).
3. M. Akiyoshi, T. Shimada, and H. Hirakata, Analyzing the bending deformation of van der Waals-layered materials by a semi-discrete layer model, *J. Appl*. *Phys*. **134**, 175102 (2023).

Domestic Conferences

1. M. Akiyoshi, S. Koike, T. Shimada, and H. Hirakata, Self-restoration of bending deformation in multi-layered graphene, *JSME*: *2021 Mech. Eng. Cong*., (Chiba Univ., 2021.9). (in Japanese)
2. M. Akiyoshi, S. Koike, T. Shimada, and H. Hirakata, Ultra-large bending deformation and self-restoration of multi-layered graphene, *JSMS: 2021 Mat. Week (Mat. Symp.) Work shop*, (Kyoto, 2021.10). (in Japanese)
3. M. Akiyoshi, T. Shimada, and H. Hirakata, Cohesive zone model for analysis on bending deformation of van der Waals-stacked materials, *JSME*: *CMD2022*, (Kagoshima Univ., 2022.11). (in Japanese)
4. M. Akiyoshi, T. Shimada, and H. Hirakata, Bending deformation analysis on van der

Waals-layered materials based on a semi-discrete layer model, *JSME*: *CMD2023*, (Toyohashi, 2023.10). (in Japanese)

5. S. Koike, M. Akiyoshi, S. Uegaki, T. Shimada, and H. Hirakata, Ultra-large bending deformation and its self-restoration of multilayered graphene by layered atomic structure, *JSME*: *M&M 2021*, (Nagoya Univ. 2021.9). (in Japanese)
6. H. Hirakata, R. Masuda, M. Akiyoshi, and T. Shimada, High fracture toughness due to disappearance of stress singularity in van der Waals-stacked $MoTe_2$, *JSME*: *CMD2022*, (Kagoshima Univ., 2022.11). (in Japanese)

Not related to this dissertation

Full Length Papers

1. M. Akiyoshi, A. Goto, N. Mohri, and N. Saito, Planarization of a layer made by using electrical discharge machining, *JSME Int*. *J*. 46, 3(2003).
2. N. Hana, M. Umeda, M. Akiyoshi, K. Mitamura, and Kenji Amaya, Crack identification by digital image correlation method using crack shape as prior information, *J. Pressure Vessel Technol*. 145, 041601 (2023).
3. N. Hana, M. Umeda, M. Akiyoshi, and K. Amaya, Identification of crack shapes by digital image correlation using joint estimation maximum a posteriori method, *J. Pressure Vessel Technol*. 145, 021601 (2023).

Domestic Conferences

1. M. Akiyoshi, A. Goto, and N. Mohri, Examination of formation mechanism of layer in EDC, *JSME*: *The Proceedings of The Manufacturing & Machine Tool Conference* 4,

121(2002). (in Japanese)

2. M. Akiyoshi, A. Goto, and N. Mohri, Performance improvement of layer produced by EDC by control gap distance, *JSEME*: *Electrical Processing Technol*. 26, 15(2002). (in Japanese)
3. M. Akiyoshi and T. Yuzawa, Study of sludge behavior in jump movement of EDM, *JSEME*: *2002 National convention*. (in Japanese)
4. M. Akiyoshi and T. Yuzawa, Study of sludge behavior in jump movement of EDM, *JSME*: *The Proceedings of The Manufacturing & Machine Tool Conference* 3, 247(2001). (in Japanese)
5. M. Akiyoshi, A. Goto, Y. Uehara, and N. Mohri, Study of Current Pulse Pattern in EDC Processing, *JSME*: *The Proceedings of The Manufacturing & Machine Tool Conference* 2, 31(2000). (in Japanese)
6. Y. Uchida, K. Maeda, K. Takeda, H. Mori, M. Furukawa, and M. Akiyoshi, Measurement Technique for Nonstationary Pressure Field in a Turbofan by Using Pressure Sensitive Paint, *JSME*: *2015 Fluids Enf. Conf.* (in Japanese)
7. K. Maeda, H. Mori, M. Furukawa, and M. Akiyoshi, Measurement Technique for Unsteady Low-speed Flow Fields Using Polymer-type Pressure Sensitive Paint, *JSME*: *2014 Fluids Enf. Conf.* (in Japanese)
8. H. Kawabata, N. Omura, H. Mori, M. Furukawa, M. Akiyoshi, and S. Okino, Measurement Technique for Unsteady Low-speed Flow Fields Using Pressure Sensitive Paint, *JSME*: *2012 Fluids Enf. Conf.* (in Japanese)

Acknowledgements

I would like to express my sincere gratitude to Professor Hiroyuki Hirakata for his warm guidance and encouragement in carrying out this research. Thanks to his patience and careful guidance, I was able to clarify what I needed to do and move forward step by step. Without his acceptance as my advisor and support for my research, I would not have been able to complete my degree. His guidance was the catalyst for a significant change in my thinking and work performance. I would like to express my utmost respect and gratitude to him.

I would also like to sincerely thank Professor Takahiro Shimada for his many helpful suggestions and teachings in the completion of this dissertation. I would like to express my sincere gratitude to him.

I would like to thank Professor Motofumi Suzuki and Professor Tomoko Hirayama for their helpful advice and guidance in the completion of this dissertation.

I would also like to express my deepest gratitude to Professor Takayuki Kitamura and Professor Takashi Sumigawa for opening the doors of my degree with the launch of organizational collaboration, one of the objectives of which was to increase the number of researchers.

Finally, I would like to thank my family for their constant support over the years.